eXPRESS Polymer Letters Vol.7, No.4 (2013) 319
Available online at www.expresspolymlett.com
DOI: 10.3144/expresspolymlett.2013.28

Editorial corner – a personal view

Recent research on conductive phase-change materials for energy storage

A. S. Luyt[*]

Department of Chemistry, University of the Free State (Qwaqwa Campus), Phuthaditjhaba, South Africa

Long chain paraffin-based phase change materials (PCM) for energy storage are materials that can store and release thermal energy through melting and solidification processes. Over the years a fair amount of work has been done to determine the suitability and properties of such materials. The first challenge was to find ways to prevent the leaking or flow of the molten paraffins. Some solutions e.g. encapsulation of the PCM by a thin polymeric shell and the formation of immiscible polymer/PCM blends were investigated. The most recently investigated challenge is to improve the thermal conductivity of the systems, because both polymer and paraffin have relatively high thermal resistivities.

A few papers were published during the past four years where the PCM was directly mixed with the conductive filler. These investigations included expanded graphite, carbon nanofibres and carbon nanotubes as fillers mixed into several paraffin-based PCMs. Generally the thermal conductivity increased, but several factors such as particle shape and orientation and particle dispersion were found to influence the extent of improvement in thermal conductivity. Another approach was the microencapsulation of a PCM by an inorganic conductive shell. The most investigated approach was the impregnation of thermally conductive, porous fillers with the liquid PCM. It was observed that the PCM was trapped inside the pores of the fillers, and generally no leakage was observed after melting of the PCM. The last approach, which involves polymers, is the formation of immiscible polymer/PCM blends containing conductive fillers. The effectiveness of such systems is determined by the extent of immiscibility of the polymer and PCM, and the strength of the interaction between the polymer or PCM and the conductive filler.

To me the last approach is the most interesting from a polymer scientist's viewpoint, because there are a number of factors that may determine the properties and effectiveness of such a phase-change system, e.g. crystallization kinetics of polymer and PCM, extent of co-crystallization, location and dispersion of conductive filler particles, extent of interaction of the filler particles with respectively the polymer and the PCM, to name a few. This may not be groundbreaking research, but the results of such research will certainly contribute to the finding of solutions for the provision of renewable energy.

Prof. Dr. Riaan Luyt
Member of International Advisory Board

[*]Corresponding author, e-mail: LuytAS@qwa.ufs.ac.za

eXPRESS Polymer Letters Vol.7, No.4 (2013) 320–328
Available online at www.expresspolymlett.com
DOI: 10.3144/expresspolymlett.2013.29

Graphene reinforced biodegradable poly(3-hydroxybutyrate-*co*-4-hydroxybutyrate) nano-composites

*V. Sridhar, I. Lee, H. H. Chun, H. Park**

Global Core Research Center for Ships and Offshore Plants (GCRC-SOP), Pusan National University, 60-735 Busan, Republic of Korea

Received 27 September 2012; accepted in revised form 5 December 2012

Abstract. Novel biodegradable poly(3-hydroxybutyrate-*co*-4-hydroxybutyrate) [PHBV]/graphene nanocomposites were prepared by solution casting. The thermal properties, crystallization behavior, microstructure, and fracture morphology of the composites were investigated. Scanning electron microscope (SEM) results show that graphene layers are homogeneously dispersed in the polymer matrix. X-ray diffraction (XRD) and dynamic scanning calorimetry (DSC) studies show that the well dispersed graphene sheets act as nucleating agent for crystallization. Consequently, the mechanical properties of the composites have been substantially improved as evident from dynamic mechanical and static tensile tests. Differential thermal analysis (DTA) showed an increase in temperature of maximum degradation. Soil degradation tests of PHBV/graphene nanocomposites showed that presence of graphene doesn't interfere in its biodegradability.

Keywords: *polymer composites, biodegradable polymers, thermal properties, graphene*

1. Introduction

With fast depletion of crude oil, ever increasing environmental problems associated with the end-of-life disposal of plastics obtained from petroleum oils and geo-political uncertainties associated with reliable supply of crude oil, alternate biodegradable plastics like poly(hydroxyalkanoate)s (PHAs) have gained considerable interest due to their biocompatibility, biodegradability, and renewable- resource-based origin [1]. Poly(3-hydroxybutyrate) (PHB), a homo-polymer with a highly stereo-regular structure that leads to high crystallinity is the most extensively known poly(hydroxyalkanoate). Though this high degree of crystallinity is useful in some applications, but it leads to a stiffness-toughness imbalance which limits its usage in many commercial applications [2]. Also, from processing point of view, PHB has a very narrow processing window, and undergoes extensive thermal degradation above its melting temperature during extrusion or injection molding [3]. In order to overcome these drawbacks, PHB has been copolymerized with hydroxyvalerate (HV), resulting in poly(3-hydroxybutyrate-*co*-4-hydroxybutyrate) PHBV, copolymers which have higher flexibility and lower processing temperatures [4].

One major disadvantage of PHBV polymers is its poor mechanical properties. In order to overcome this there are many reports on reinforcing effects of fibers and nano-particles in PHBV. PHBV reinforced with natural fibers such as cellulose [5], jute fibers [6], other agricultural fibers [7, 8], bamboo pulp [9], peach palm particles [10], starch [11], kenaf fibers [12], tapioca flour [13], the so-called 'green composites' have been reported. But the strength of these green composites is less than

*Corresponding author, e-mail: hyunpark@pusan.ac.kr

desirable. Reinforcement of nano-particles in PHBV like zinc oxide [14, 15], silica [16], calcium phosphate [17, 18], attapulgite [19], hydroxyapatite [20] etc. have also been reported. But among these nano-scaled reinforcing agents, fillers with lamellar or layered structure have special significance of which nano-clay [21–23], boron nitride [24], layered double hydroxides [25], halloysite [26] are noteworthy. The advantage of lamellar fillers is it acts as barrier material which increases the air impermeability of the membrane, besides the reinforcing effect which also improves its mechanical properties.

In recent years nano-carbons like carbon nanotubes and carbon nanofibers has attracted attention due to their excellent mechanical, thermal and electrical properties. Graphene, the new generation carbonaceous layered material has shown considerable potential as reinforcing material in polymer nanocomposites [27–29]. Though there are some research reports showing property improvements in biodegradable PHBV with the addition of carbon nanotubes [30] and carbon nanofibers [31] and utilization of graphene in poly(3-hydroxybutyrate, PHB) [32, 33], graphene reinforced PHBV nanocomposites have never been reported. In this study we report a systematic study on the effect of addition of graphene on the morphology, thermal and dynamic mechanical properties of PHBV. The effect of graphene on biodegradability of PHBV is also presented.

2. Materials and experimental

2.1. Synthesis of graphene

Graphene was synthesized by our previously reported microwave method using hydrogen peroxide as the eco-friendly oxidizing agent and ammonium peroxy disulfate as the radical initiator [34]. The procedure involves mixing of expandable graphite (Samjung C & G, Seoul, Korea), ammonium peroxy disulfate and hydrogen peroxide (both from Sigma-Aldrich, Seoul, Korea) at weight ratio of 2:1:0.5 in a glass tube at room temperature and ultrasonicating the mixture for 3 min. Subsequently, the glass tube was placed in a domestic microwave oven (Daewoo) and irradiated at 500 W. Under microwave irradiation, the precursors exfoliated rapidly to graphene worms, which were ultrasonicated in DMF for 10 mins. The thick graphene pieces and partially exfoliated graphite flakes settled down and were subsequently removed by centrifugation, wherein few-layered fluffy graphene nano-sheets rise to the top of the glass tube. A representative TEM of the graphene sheets obtained by this method is shown in Figure 1.

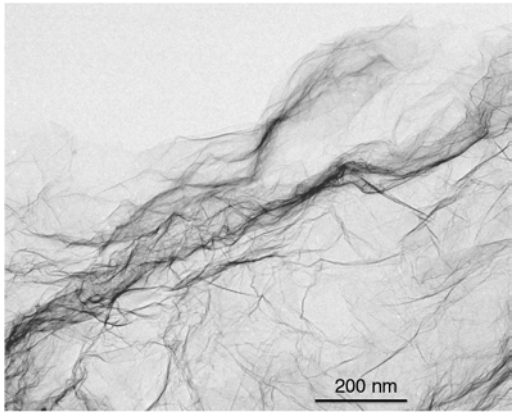

Figure 1. TEM micrograph of graphene synthesized by eco-friendly microwave method

2.2. Preparation of graphene/PHBV nano-composite films

The biodegradable poly(3-hydroxybutyrate-*co*-3-hydroxyvalerate), PHBV with 13 mol% hydroxyvalerate content, under the trade name Biopol with a molecular weight ~450 000, and 13% valerate content was procured from Biomer, Germany. Solution-cast film samples of pure PHBV and PHBV reinforced with 2, 4, and 6 wt% of graphene were prepared with a dry film thickness of around 100 μm, using chloroform as a solvent. Graphene oxide solution in chloroform were mixed in an ultrasonic homogenizer for 10 min and then stirred with the polymer solution at room temperature for 24 hours. Subsequently, the material was cast onto Petri dishes to obtain films after solvent evaporation at room temperature.

2.3. Characterization and testing

2.3.1. Morphology

Bright-field TEM images were recorded using a Philips EM 420 instrument at an accelerating voltage of 120 kV. SEM (scanning electron microscopy) images were recorded using a cold field emission scanning electron microscope (S-4700, Hitachi, Japan).

2.3.2. X-ray analysis

X-ray diffraction (Rigaku, Japan, D/Max, 2500V, CuKa radiation: 1.54056A) experiments were carried out on both the pristine PHBV and the graphene/

PHBV nanocomposite samples. The solvent cast films were cut into a size of about 15 mm × 15 mm and the X-ray diffractograms were recorded in the range ca 5–40° (2θ) with a step size of 0.04, and a time per step of 1 s.

2.3.3. Mechanical testing

The static tensile tests were performed on Instron 5564, Universal Testing Machine (England) at a cross-head speed of 5 mm/min, according to ASTM D 638-99 standards at room temperature.

2.3.4. DMA experiments

The dynamic viscoelastic properties of PHBV and the nano-composites were measured using a Q800 DMTA (TA instruments, USA) operating in the tensile mode at a frequency of 1 Hz and oscillating amplitude of 15 min. Frequency dependent mechanical characteristics were studied at room temperature in the range of 0.1 to 100 Hz.

2.3.5. DSC

DSC measurements were carried out on a DSC 2920 (TA Instruments, USA) using nitrogen as a purge gas. The temperature and heat flow were calibrated with indium. Samples of around 7 mg were cut from the solvent cast films and DSC traces of specimens were recorded upon heating at a rate of 10°C/min.

3. Results and discussion

Scanning electron microscopy was used to investigate the dispersion of graphene in the polymer matrix and a representative micrograph is shown in Figure 2a. A typical layered structure of graphene layers which are indicated by arrows in the polymer

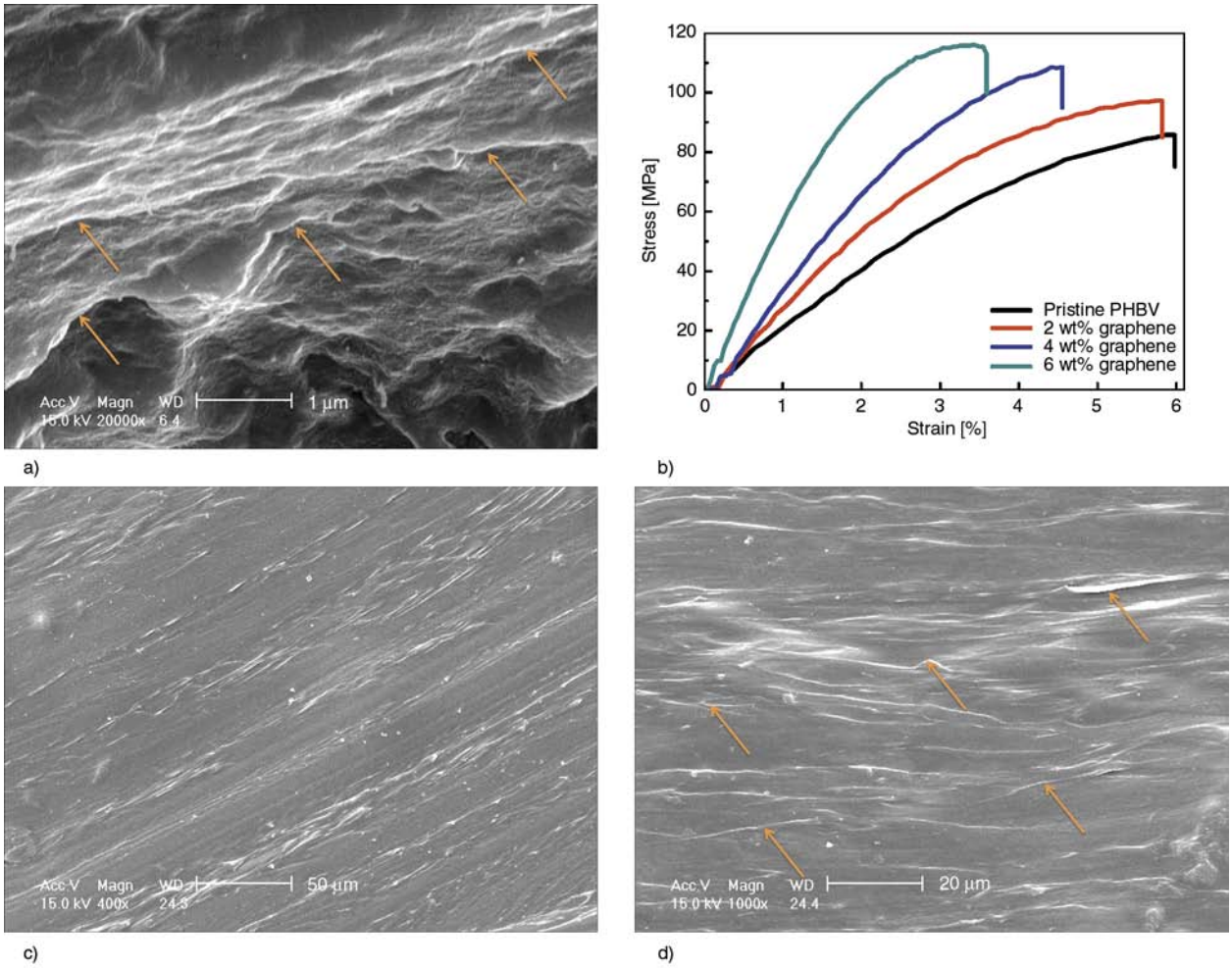

Figure 2. Morphology of graphene reinforced PHBV nanocomposites (a); stress-strain curves of recast and graphene reinforced PHBV nanocomposites (b); representative SEM micrographs of fracture surface of graphene reinforced PHBV nano composites at low (c) and high (d) magnifications. The arrows indicate graphene layers embedded in the polymer matrix.

matrix is observed; suggesting that during the solvent evaporation of solution-cast films enhances the alignment of graphene layers parallel to the surface of PHBV fibrils. A similar observation in alignment of graphene in diblock polymers has been reported earlier [35]. SEM micrographs also indicate that the graphene sheets were dispersed uniformly in the composite and there is no obvious aggregation of sheets in the polymer matrix. The influence of graphene content on the stress-strain properties of the nano composites is shown in Figure 2b. With the incorporation of 2, 4 and 6 wt% of graphene the modulus at break increased to 97.3, 108.7 and 115 MPa which is about 10.2, 19.7, 25.71% higher than that of pure PHBV (85.7 MPa). This progressive increase in modulus at break is a manifestation of the reinforcing ability of graphene in PHBV matrix. The improvement in the modulus could also be attributed to the lamellar structure of the graphene, which allows better wettability and enhanced polymer-filler interactions between the filler and polymer matrix, thereby leading to better stress transfer. Figure 2c and 2d is SEM taken from the fracture surface, showing significant crack deflection at low and high magnifications, respectively. As is evident from the fractographs, the surface of the fractured sample appears to be rough and crack appears to grow along the interface of graphene layers, suggesting a poorer interfacial adhesive strength when compared to the inherent cohesive strength of the PHBV matrix. Fracture in heterogeneous systems like filler reinforced polymer nanocomposites, is initiated from imperfections introduced due to addition of fillers. These imperfections are the stress concentration points and initiate crack growth under an applied load, until one or more of them coalesce to reach sufficient size for fracture. So, when this crack encounters a rigid inclusion (graphene in this case), the crack tilts and twists, generating an increase in the total fracture surface area, resulting in greater energy absorption. Additionally, the lamellar nature of graphene can also cause crack deflection, crack bifurcation and can even arrest the propagation of micro-cracks.

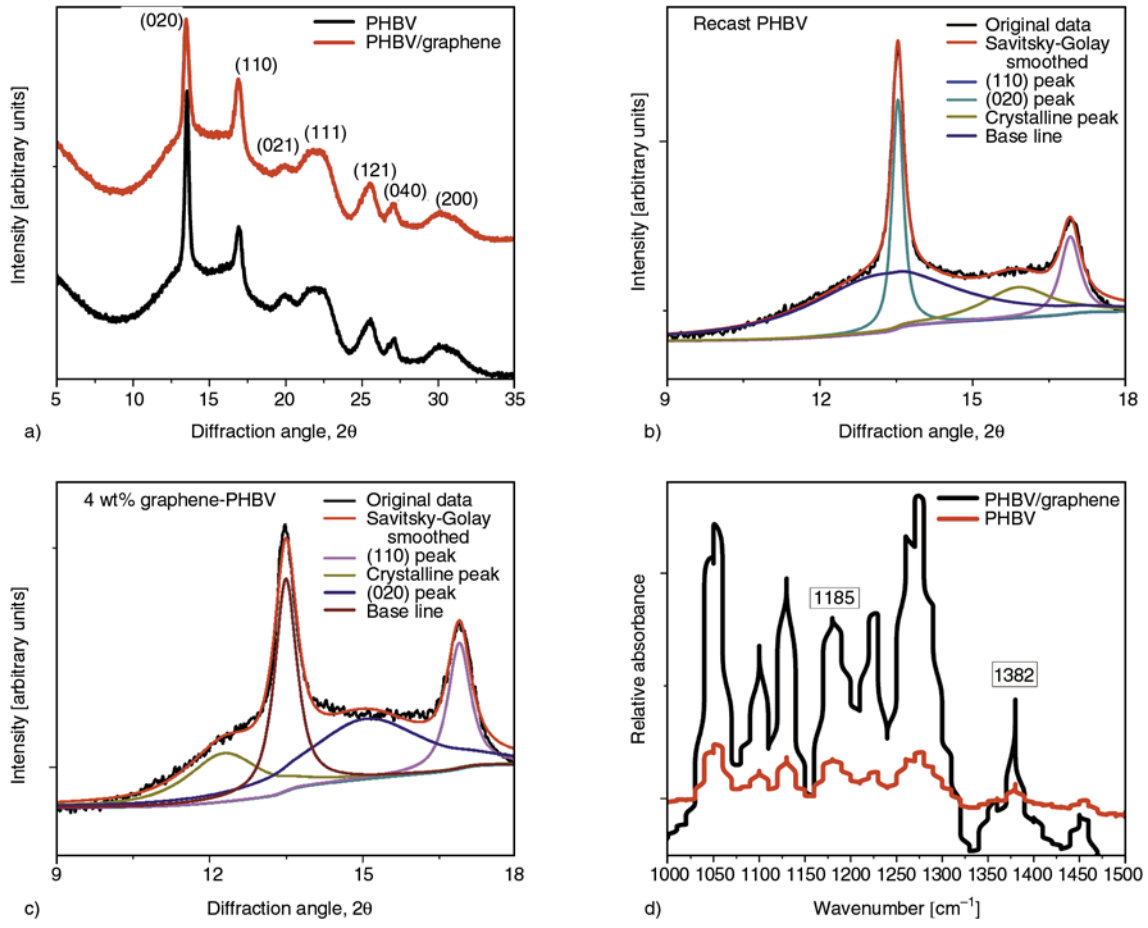

Figure 3. WAXD of PHBV and graphene reinforced PHBV nanocomposites (a); deconvoluted XRD peak profile analysis of recast (b) and graphene reinforced PHBV nanocomposites (c); FTIR spectra of recast and graphene reinforced PHBV nanocomposites showing variation in crystallinity (d)

Figure 3a shows X-ray patterns in the range 5 to 35 of pristine PHBV and its nanocomposites with graphene. The WAXD diffractograms of recast PHBV and PHBV/graphene nanocomposites show a semicrystalline nature with its characteristic reflections corresponding to an orthorhombic cell [25]. Both PHBV and PHBV/Graphene shows reflections at the same values as for the neat biopolymer, indicating that addition of graphene does not alter the unit cell after incorporation of graphene. However, the addition of graphene results in increase in FWHM, when compared to that of pure PHBV. The crystallite size L [nm] calculated for the (020) reflection peak using Scherrer's equation is 14.19 and 18.22 nm in recast PHBV and graphene/PHBV nanocomposites respectively, indicating that the crystallization of PHBV chains is promoted due to the presence of graphene. In order to further study this increase in crystallization, we have deconvoluted the XRD peaks of recast PHBV (Figure 3b) and graphene reinforced PHBV (Figure 3c) in the range of 9 to 18°. Deconvoluted XRD of graphene/PHBV shows substantial increase in the percentage of crystalline peak occuring at 15.5 when compared to its pristine counterpart which indicates that a portion of amorphous PHBV chains are bound to the surface of graphene thereby forming an interphase layer. More evidence of changes in crystallinity can be observed from FTIR spectra.

Bloembergen *et al*. [36] defined a crystallinity index, CI, in PHBV polymers, determined by normalising the intensity of 1185 cm^{-1} band to that of the 1382 cm^{-1} band, which was found to be sensitive to the degree of crystallinity. Figure 3d shows infrared spectra of recast and 4 wt% graphene reinforced PHBV samples. Though both the bands are similar in shape, there was tremendous change in the intensity in the two spectra. When the absorbance intensity of the 1382 cm^{-1} band was divided by that of the 1185 cm^{-1} band the IR spectrum of pristine PHBV exhibited a lower CI value compared to the graphene/PHBV spectrum. Solvent recast PHBV film yielded a CI value of 1.03 while that of graphene/PHBV yielded a CI value of 1.164. Combining these values with the crystallinity obtained by deconvoluted XRD analysis it can be concluded that addition of graphene into PHBV results in higher crystallinity.

Figure 4a shows the differential scanning calorimetry (DSC) data for neat PHBV and its graphene nanocomposites. A bimodal endothermic melting peak in the heating mode is observed in all the samples corresponding to the formation of two crystalline phases with different sizes of lamellae of varying thickness. With increase in graphene concentration, there was a progressive decrease in melting peak temperatures. This can be explained on the basis of hetero and homogeneous nucleation of PHBV. It has been reported that the two melting peaks of PHBV correspond to the heterogeneous nucleation of PHBV occurring due to chain aggregation and the higher temperature peak is related to homogeneous nucleation. Our result indicates that the addition of graphene influences both types of nucleation and is consistent with earlier reports on solvent cast layered nano-clay reinforced PHBV nanocomposites [22].

Figure 4b shows the differential thermal analysis (DTA) for neat PHBV and its graphene reinforced

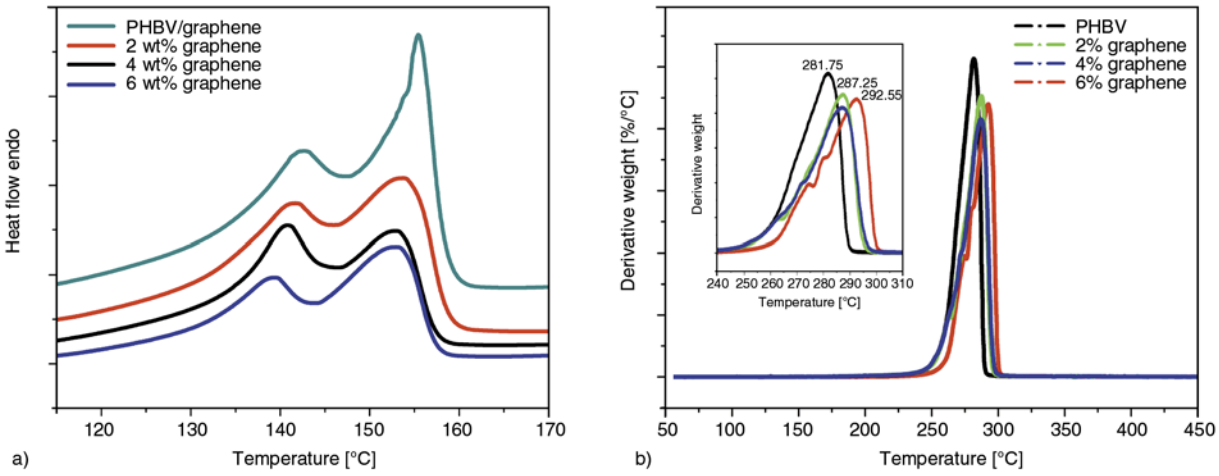

Figure 4. DSC heating curves (a) and Differential thermal analysis (b) of recast and PHBV/graphene at increasing concentrations

nanocomposites. From the plots it is evident that the thermal degradation process of PHBV and PHBV/graphene nanocomposites occurs in only one weight loss step and there is a progressive increase in temperature of maximum weight loss from 281 to 292°C. This indicates that layered structure of graphene improves the thermal stability of the PHBV matrix. It is noteworthy that the thermal stability of PHBV nanocomposite with 6 wt% graphene is lower than that of nanocomposites with its 2 and 4 wt% counterparts. It is widely known that layered fillers like graphene and nano-clay act as a barrier to permeability of volatile degradation products of the nanocomposites, which increases the thermal stability of polymer matrix. When compared to traditional layered fillers like nano-clay, graphene also has the additional advantage of being a very good electron acceptor and is capable of forming donor-acceptor complexes with the byproducts of nucleophilic chain scission of PHBV during its thermal degradation.

In many real time applications, a polymer nanocomposite will be subjected to many temperature and frequency fluctuations. Dynamic mechanical thermal analysis (DMTA) can provide reliable information over the relaxation behavior of the materials. In order to evaluate the effect of graphene on temperature dependent relaxation behavior of PHBV matrix, thermo-mechanical properties were measured from –20 to 100°C and plotted in Figure 5a. The glass transition temperature (T_g) of the nanocomposites shifted slightly to higher temperature with the increase of the graphene content: Tgs were 22.73, 22.82, 24.97 and 23.9°C at the graphene content of 0, 2, 4 and 6 wt% respectively. The increase in Tg with addition of graphene is marginal and is consistent with that of MWNT/PHBV nanocomposites [28].

Figure 5b shows the variation in storage modulus with temperature. In the tested temperature range, graphene reinforced nanocomposites show substantially higher modulus values than pristine PHBV and the magnitude of this increase in modulus is more than 100% in the whole range of temperature spectrum. In the rubbery region (until 10°C), the increase in the rubbery modulus can be attributed to the immobilization of polymer chains onto the graphene surface increasing the effective volume of the filler. Samples with 6 wt% graphene concentration show substantially higher storage modulus

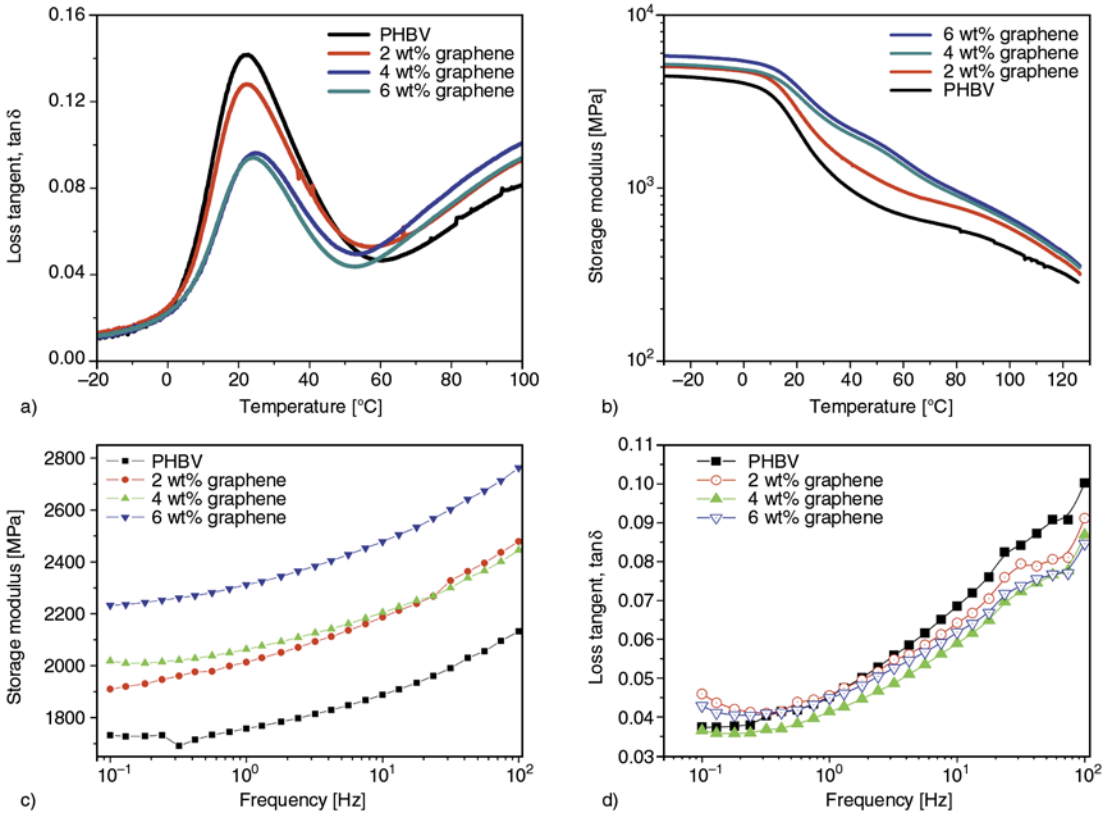

Figure 5. Variation in loss tangent (a) and storage modulus (b) in PHBV and PHBV/graphene nanocomposites as a function of temperature. Frequency dependent variations in storage modulus (c) and loss tangent (d).

which can be attributed to increased immobilization of PHBV chains onto the graphene surfaces. The rubbery modulus is also known to depend on the degree of crystallinity of the material. The crystalline regions act as physical crosslinks and also act as filler particles because of their finite size, which would increase the modulus substantially. The substantial increase in modulus is also consistent with the increase in crystallinity of PHBV due to the presence of graphene as discussed earlier in XRD and DSC sections. With increase in temperature as the nanocomposite pass through a 'terminal zone', corresponding to the melting of crystalline domains, the elastic shear modulus becomes lower and lower with temperature. Even in this region the modulus of graphene reinforced PHBV samples is more than double than that of pristine PHBV, indicating the tremendous reinforcing potential of graphene.

Though there are many studies on the carbonaceous filler reinforced dynamic mechanical properties of PHBV, frequency dependent characteristics of PHBV has never been reported [37]. Dynamic frequency sweep tests were conducted on PHBV and PHBV/graphene composites at 25°C. The effects of variation in graphene content on the storage modulus (G') and loss tangent are shown in Figure 5c and 5d respectively. It is known that the rheological behavior of unfilled polymers is typical of a visco-eleastic fluid, whereas addition of nano-scaled fillers weakens the frequency dependence of storage and loss tangent in the low-frequency region, thereby resulting in a pseudo-solid-like behavior.

It can be seen that with incorporation of graphene, the storage modulus is enhanced in the whole frequency range, which could be ascribed to the increase in stiffness by the graphene layers that allow efficient stress transfer between the filler and polymer chains. With further increase in the graphene concentration, graphene/graphene interactions become stronger resulting in percolation and formation of an interconnected structure, the formation of percolation limit. This phenomenon is more observable in the dependence of loss tangent with frequency, wherein all the samples show an abrupt 'hump' in loss tangent at 10 Hz implying the onset of transition from liquid-like to solid-like viscoelastic behavior.

It is well known that PHBV is a biodegradable plastic, however there are some conflicting reports on the cyto-toxic nature of graphene. So, in order to check the biodegradability, PHBV/graphene nanocomposites were buried under soil and representative SEM micrograph of the sample after 60 days of burial is shown in Figure 6. The surface of the sample is all roughed up accompanied by presence of fibrillar byproducts of PHBV biodegradation. However, the degree of degradation of PHBV chains in the vicinity of the graphene sheets is less when compared to the bulk. Additionally, layered graphene sheets can be still observed in the degraded sample (indicated by arrows). This infers that even though graphene itself is non-degradable, but its addition has marginal effect on the overall biodegradability of PHBV.

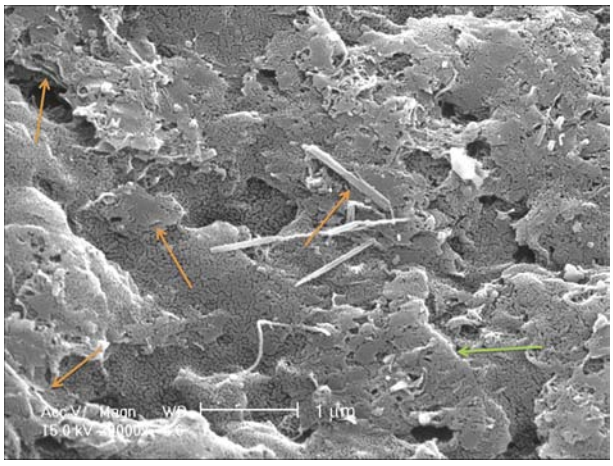

Figure 6. SEM micrographs of biodegradation of PHBV/graphene nanocomposites after 60 days

4. Conclusions

Graphene reinforced PHBV nanocomposites were successfully prepared by solution casting method. SEM morphology showed good dispersion of graphene layers in the PHBV matrix, whereas SEM fractographs indicated the crack pinning ability of graphene. Deconvoluted XRD and DSC studies showed increase in crystallinity accompanied with increase in crystallite size due to addition of graphene. DMA and tensile testing showed substantial increase in modulus of the samples. DTA analysis showed improvement in thermal degradation behavior due to anti-oxidant nature of graphene. Frequency dependent dynamic mechanical analysis showed a visco-elastic liquid to solid transitions at 10 Hz. Soil biodegradation tests showed that the degradation occurs predominantly in the bulk of the

sample, with less degradation of PHBV chains adhering to the graphene surface.

Acknowledgements

This work was supported by the National Research Foundation of Korea (NRF) grant funded by the Korea government (MEST) through GCRC-SOP (Grant No. 2011-0030668) and by the Industrial Strategic Technology Development Program (Grant No. 10038606) funded by the Ministry of Knowledge Economy (MKE, Korea).

References

[1] Sudesh K., Abe H., Doi Y.: Synthesis, structure and properties of polyhydroxyalkanoates: Biological polyesters. Progress in Polymer Science, **25**, 1503–1555 (2000).
DOI: 10.1016/S0079-6700(00)00035-6

[2] Gogolewski S., Jovanovic M., Perren S. M., Dillon J. G., Hughes M. K.: Tissue response and *in vivo* degradation of selected polyhydroxyacids: Polylactides (PLA), poly(3-hydroxybutyrate) (PHB), and poly(3-hydroxybutyrate-*co*-3-hydroxyvalerate) (PHB/VA). Journal of Biomedical Research, **40**, 1135–1148 (1993).
DOI: 10.1002/jbm.820270904

[3] Yasin M., Holland S. J., Tighe B. J.: Polymers for biodegradable medical devices: V. Hydroxybutyrate-hydroxyvalerate copolymers: Effects of polymer processing on hydrolytic degradation. Biomaterials, **11**, 451–454 (1990).
DOI: 10.1016/0142-9612(90)90057-W

[4] Avella M., Martuscelli E., Raimo M.: Review: Properties of blends and composites based on poly(3-hydroxy)butyrate (PHB) and poly(3-hydroxybutyrate-hydroxyvalerate) (PHBV) copolymers. Journal of Materials Science, **35**, 523–545 (2000).
DOI: 10.1023/A:1004740522751

[5] Ten E., Bahr D. F., Li B., Jiang L., Wolcott M. P.: Effects of cellulose nanowhiskers on mechanical, dielectric, and rheological properties of poly(3-hydroxybutyrate-*co*-3-hydroxyvalerate)/cellulose nanowhisker composites. Industrial and Engineering Chemistry Research, **51**, 2941–2951 (2012).
DOI: 10.1021/ie2023367

[6] Bledzki A. K., Jaszkiewicz A.: Mechanical performance of biocomposites based on PLA and PHBV reinforced with natural fibres – A comparative study to PP. Composites Science and Technology, **70**, 1687–1696 (2010).
DOI: 10.1016/j.compscitech.2010.06.005

[7] Luo S., Netravali A. N.: Mechanical and thermal properties of environment-friendly 'green' composites made from pineapple leaf fibers and poly(hydroxybutyrate-*co*-valerate) resin. Polymer Composites, **20**, 367–378 (1999).
DOI: 10.1002/pc.10363

[8] Luo S., Netravali A. N.: Interfacial and mechanical properties of environment-friendly 'green' composites made from pineapple fibers and poly(hydroxybutyrate-*co*-valerate) resin. Journal of Materials Science, **34**, 3709–3719 (1999).
DOI: 10.1023/A:1004659507231

[9] Jiang L., Huang J., Qian J., Chen F., Zhang J., Wolcott M. P., Zhu Y.: Study of poly(3-hydroxybutyrate-*co*-3-hydroxyvalerate) (PHBV)/bamboo pulp fiber composites: Effects of nucleation agent and compatibilizer. Journal of Polymers and the Environment, **16**, 83–93 (2008).
DOI: 10.1007/s10924-008-0086-7

[10] Batista K. C., Silva D. A. K., Coelho L. A. F., Pezzin S. H., Pezzin A. P. T.: Soil biodegradation of PHBV/peach palm particles biocomposites. Journal of Polymers and Environment, **18**, 346–354 (2010).
DOI: 10.1007/s10924-010-0238-4

[11] Koller I., Owen A. J.: Starch-filled PHB and PHB/HV copolymer. Polymer International, **39**, 175–181 (1996).
DOI: 10.1002/(SICI)1097-0126(199603)39:3<175::AID-PI472>3.3.CO;2-S

[12] Avella M., Gaceva G-B., Buzõarovska A., Errico M. E., Gentile G., Grozdanov A.: Poly(3-hydroxybutyrate-*co*-3-hydroxyvalerate)-based biocomposites reinforced with kenaf fibers. Journal of Applied Polymer Science, **104**, 3192–3200 (2007).
DOI: 10.1002/app.26057

[13] Kaewkannetra P., Soonthornchiya J., Moonamart S.: Increasing of tapioca flour by blending and forming with commercial PHBV and biopolymer obtained from fermented sugar cane juice for producing as bioplastic. Journal of Biotechnology, **150**, 385 (2010).
DOI: 10.1016/j.jbiotec.2010.09.482

[14] Yu W., Lan C-H., Wang S-J., Fang P-F., Sun Y-M.: Influence of zinc oxide nanoparticles on the crystallization behavior of electrospun poly(3-hydroxybutyrate-*co*-3-hydroxyvalerate) nanofibers. Polymer, **51**, 2403–2409 (2010).
DOI: 10.1016/j.polymer.2010.03.024

[15] Naphade R., Jog J.: Electrospinning of PHBV/ZnO membranes: Structure and properties. Fibers and Polymers, **13**, 692–697 (2012).
DOI: 10.1007/s12221-012-0692-9

[16] Ma P. M., Wang R. Y., Wang S. F., Zhang Y., Zhang Y. X., Hristova D.: Effects of fumed silica on the crystallization behavior and thermal properties of poly(hydroxybutyrate-*co*-hydroxyvalerate). Journal of Applied Polymer Science, **108**, 1770–1777 (2008).
DOI: 10.1002/app.27577

[17] Duan B., Wang M., Zhou W. Y., Cheung W. L.: Synthesis of Ca–P nanoparticles and fabrication of Ca–P/PHBV nanocomposite microspheres for bone tissue engineering applications. Applied Surface Science, **255**, 529–533 (2008).
DOI: 10.1016/j.apsusc.2008.06.057

[18] Duan B., Wang M.: Customized Ca–P/PHBV nanocomposite scaffolds for bone tissue engineering: Design, fabrication, surface modification and sustained release of growth factor. Journal of Royal Society Interface, **7**, S615–S629 (2010).
DOI: 10.1098/rsif.2010.0127.focus

[19] Thiré R. M. S. M., Arruda L. C., Barreto L. S.: Morphology and thermal properties of poly(3-hydroxybutyrate-*co*-3-hydroxyvalerate)/attapulgite nanocomposites. Materials Research, **14**, 340–344 (2011).
DOI: 10.1590/S1516-14392011005000046

[20] Jack K. S., Velayudhan S., Luckman P., Trau M., Grøndahl L., Cooper-White J.: The fabrication and characterization of biodegradable HA/PHBV nanoparticle–polymer composite scaffolds. Acta Biomaterialia, **5**, 2657–2667 (2009).
DOI: 10.1016/j.actbio.2009.03.017

[21] Javadi A., Srithep Y., Pilla S., Clemons C. C., Gong S., Turng L-S.: Microcellular poly(hydroxybutyrate-*co*-hydroxyvalerate)-hyperbranched polymer–nanoclay nanocomposites. Polymer Engineering and Science, **51**, 1815–1826 (2011).
DOI: 10.1002/pen.21972

[22] Wang K., Wang Y., Zhang R., Li Q., Shen C.: Preparation and characterization of microbial biodegradable poly(3-hydroxybutyrate-*co*-4-hydroxybutyrate)/organoclay nanocomposites. Polymer Composites, **33**, 838–842 (2012).
DOI: 10.1002/pc.22220

[23] Bordes P., Pollet E., Avérous L.: Nano-biocomposites: Biodegradable polyester/nanoclay systems. Progress in Polymer Science, **34**, 125–155 (2009).
DOI: 10.1016/j.progpolymsci.2008.10.002

[24] Kai W., He Y., Inoue Y.: Fast crystallization of poly(3-hydroxybutyrate) and poly(3-hydroxybutyrate-*co*-3-hydroxyvalerate) with talc and boron nitride as nucleating agents. Polymer International, **55**, 780–789 (2005).
DOI: 10.1002/pi.1758

[25] Dagnon K. L., Chen H. H., Innocentini-Mei L. H., D'Souza N. A.: Poly[(3-hydroxybutyrate)-*co*-(3-hydroxyvalerate)]/layered double hydroxide nanocomposites. Polymer Composites, **58**, 133–141 (2009).
DOI: 10.1002/pi.2503

[26] Carli L. N., Crespo J. S., Mauler R. S.: PHBV nanocomposites based on organomodified montmorillonite and halloysite: The effect of clay type on the morphology and thermal and mechanical properties. Composites Part A: Applied Science and Manufacturing, **42**, 1601–1608 (2011).
DOI: 10.1016/j.compositesa.2011.07.007

[27] Tantis I., Psarras G. C., Tasis D.: Functionalized graphene –poly(vinyl alcohol) nanocomposites: Physical and dielectric properties. Express Polymer Letters, **6**, 283–292 (2012).
DOI: 10.3144/expresspolymlett.2012.31

[28] Persson H., Yao Y., Klement U., Rychwalski R. W.: A simple way of improving graphite nanoplatelets (GNP) for their incorporation into a polymer matrix. Express Polymer Letters, **6**, 141–147 (2012).
DOI: 10.3144/expresspolymlett.2012.15

[29] Bon S. B., Valentini L., Kenny J. M.: Electric field assisted thermal annealing reorganization of graphene oxide/polystyrene latex films. Express Polymer Letters, **5**, 819–824 (2011).
DOI: 10.3144/expresspolymlett.2011.80

[30] Lai M., Li J., Yang J., Liu J., Tong X., Cheng H.: The morphology and thermal properties of multi-walled carbon nanotube and poly(hydroxybutyrate-*co*-hydroxyvalerate) composite. Polymer International, **53**, 1479–1484 (2004).
DOI: 10.1002/pi.1566

[31] Sanchez-Garcia M. D., Lagaron J. M., Hoa S. V.: Effect of addition of carbon nanofibers and carbon nanotubes on properties of thermoplastic biopolymers. Composites Science and Technology, **70**, 1095–1105 (2010).
DOI: 10.1016/j.compscitech.2010.02.015

[32] Jing X., Qui Z.: Crystallization kinetics and thermal property of biodegradable poly(3-hydroxybutyrate)/graphene oxide nanocomposites. Journal of Nanoscience and Nanotechnology, **12**, 7314–7321 (2012).
DOI: 10.1166/jnn.2012.6461

[33] Jing X., Qiu Z.: Effect of low thermally reduced graphene loadings on the crystallization kinetics and morphology of biodegradable poly(3-hydroxybutyrate). Industrial and Engineering Chemistry Research, **51**, 13686–13691 (2012).
DOI: 10.1021/ie3018466

[34] Sridhar V., Jeon J-H., Oh I-K.: Synthesis of graphene nano-sheets using eco-friendly chemicals and microwave radiation. Carbon, **48**, 2953–2957 (2010).
DOI: 10.1016/j.carbon.2010.04.034

[35] Jung J-H., Jeon J-H., Sridhar V., Oh I-K.: Electroactive graphene–nafion actuators. Carbon, **49**, 1279–1289 (2011).
DOI: 10.1016/j.carbon.2010.11.047

[36] Bloembergen S., Holden D. A., Hamer G. K., Bluhm T. L., Marchessault R. H.: Studies of composition and crystallinity of bacterial poly(β-hydroxybutyrate-*co*-β-hydroxyvalerate). Macromolecules, **19**, 2865–2871 (1986).
DOI: 10.1021/ma00165a034

[37] Vidhate S., Innocentini-Mei L., D'Souza N. A.: Mechanical and electrical multifunctional poly(3-hydroxybutyrate-*co*-3-hydroxyvalerate) – multiwall carbon nanotube nanocomposites. Polymer Engineering and Science, **52**, 1367–1374 (2012).
DOI: 10.1002/pen.23084

eXPRESS Polymer Letters Vol.7, No.4 (2013) 329–339
Available online at www.expresspolymlett.com
DOI: 10.3144/expresspolymlett.2013.30

Preparation and characterization of rubbery epoxy/multiwall carbon nanotubes composites using amino acid salt assisted dispersion technique

*S. B. Jagtap, D. Ratna**

Naval Materials Research Laboratory, Shil-Badlapur Road, Anand nagar P.O., District Thane, Maharashtra 421 506, 421506 Ambernath, India

Received 8 October 2012; accepted in revised form 6 December 2012

Abstract. Epoxy/multiwall carbon nanotubes (MWCNT) composites were prepared using sodium salt of 6-aminohexanoic acid (SAHA) modified MWCNT and its effect properties of related composites were investigated. The composite prepared using a polar solvent, tetrahydrofuran exhibits better mechanical properties compared to those prepared using less polar solvent and without using solvent. The tensile properties and dynamic storage modulus was found to be increased as a result of modification of MWCNT with SAHA. This improvement in the tensile properties and dynamic mechanical properties of epoxy/MWCNT composite is a combined effect of cation-π interaction and chemical bonding. Fourier transform infrared spectroscopy (FTIR) and Raman spectroscopy were used to explain cation-π interaction between SAHA with MWCNT and chemical bonding of SAHA with epoxy resin. The effect of modification of MWCNT on morphology of a nanocomposite was confirmed by using scanning electron microscopy (SEM) and transmission electron microscopy (TEM). The present approach does not disturb the π electron clouds of MWCNT as opposed to chemical functionalization strategy.

Keywords: *nanocomposites, mechanical properties, carbon nanotubes, epoxy resin*

1. Introduction

Carbon nanotubes (CNTs)-based polymer composites have many potential applications due to their extraordinary properties [1–9]. CNTs offer significant improvements in the various properties of polymers for wide variety of applications. Initial academic research on polymer/CNT nanocomposites has been focused on single wall carbon nanotubes (SWCNT) because of their simpler structure. However, the extremely high cost of SWCNT considerably restricts the commercialization of CNT-based composites. Nowadays, the production of multiwall carbon nanotubes (MWCNT) has already been scaled up by the industries and therefore the research interest has been diverted towards the technological proliferation of MWCNT–based systems [10–12]. However, the strong tendency of MWCNT to form agglomerates (due to Van der Waals forces) makes the nanotubes incompatible with the polymer matrix. Hence, homogeneous dispersion of MWCNT still remains as a great challenge. Several strategies such as high shear mixing, ultrasonication, surface oxidation (covalent functionalization) and the use of surfactant have been addressed to overcome the obstacle of agglomeration [13–14]. The surface oxidation is most widely used to achieve the desired properties. However, generation of functional groups due to the surface oxidation create the structural defect to the MWCNT (which disturb the π electron cloud) and deteriorate the intrinsic properties of MWCNT.

*Corresponding author, e-mail: ratnad29@hotmail.com

Recently, 'cation-π' interaction by using surfactant has been realized as the best way to achieve good dispersion of MWCNT and interfacial interaction [15–18]. The cation of such modifiers interacts with the π electron clouds of MWCNT and reduces the Van der Waals force. This method does not disturb the π electron clouds of MWCNT. In the present paper, we described the cation-π interaction using a sodium salt of 6-aminohexanoic acid (SAHA) as a modifier and MWCNT into the epoxy matrix. Though the modifier has been used for melt blending process by others [16], to our knowledge it has not been directly used for thermoset epoxy matrix.

Studies on epoxy/MWCNT composites are reported to date are mostly related to high T_g (glassy) epoxy systems [19–24]. In the present paper, we used rubbery epoxy matrix ($T_g \sim 5$°C) to study the reinforcing effect of MWCNT because the reinforcing effect in a flexible matrix is more prominent than that observed in a glassy one [25]. The rubbery epoxies are particularly important because of their use for vibration damping application [26]. However, poor mechanical properties of such flexible epoxies are a major drawback which restricts their application. That is why we used MWCNT to improve the mechanical properties of such rubbery epoxy. The modifier SAHA is designed in such way that it contains a cation (Na^+), which interacts with the π electron clouds of MWCNT via cation-π interaction and the free $–NH_2$ group can form chemical bonding with the epoxy resin. In this way, the nanotubes become an integral part of cross linking through chemical bonding between SAHA and epoxy resin. This provides an effective load transfer from epoxy matrices to nanotubes for the enhancement of mechanical properties. The nanocomposites prepared by using the present method is expected to improve dispersion of MWCNT in the flexible epoxy matrix. The effect of SAHA modified MWCNT on the mechanical, dynamic mechanical properties and morphology of the epoxy matrix will be discussed in the present paper.

2. Experimental

2.1. Materials

Epoxy resin diglycidyl ether of bisphenol A (DGEBA) (LY556) was purchased from Vantico (USA). Poly(oxypropylene) diamine (Jeffamine ED900, Sigma Aldrich, USA) was added as a curing agent for epoxy. MWCNT (Baytube® 150P) was procured from Bayer Material Science AG (Leverkusen, Germany). The MWCNTs synthesized by the chemical vapor deposition (CVD) method having purity 95% with diameter in the range of 5–20 nm and the length 1–10 μm. 6-aminohexanoic acid (purity – 98%) and sodium hydroxide (98%) were purchased from Merck chemical, Germany. Acetone and tetrahydrofuran were used as received and purchased from Merck chemical, Germany.

2.2. Preparation of nanocomposites

The SAHA modified MWCNT was prepared by mixing of 6-amino hexanoic acid, sodium hydroxide (1:1 mass ratio w/w) and MWCNT in 100 mL distilled water in 250 mL beaker. The mixture was sonicated for 20 min using a probe sonication (Bandelin Ultrasonic homogenizer, SONOPULS HD-3200, working frequency 20 kHz, Germany), keeping the beaker immersed in cold water. The water was removed by applying vacuum and the mixture was dried at 100°C for 24 h. Composites with unmodified and SAHA-modified MWCNT were prepared using small amount (20 wt%) of solvent. A typical procedure for preparation of nanocomposites using solvent is described as follows. 0.125 g MWCNT was added into solvent and sonicated using a probe sonication for 1 h. 25 g epoxy resin was added into it and the mixture was again sonicated for 20 min, keeping the beaker immersed in cold water. The solvent was removed by applying vacuum. Then, 19 g of curing agent (JeffamineED 900) was added into the mixture, mixed uniformly for 15 min, degassed for 10 min and allows to cure in Teflon mold at 80°C for 6 h. Figure 1 illustrates the flow chart of nanocomposites preparation by using solution. The composites prepared using solvent with unmodified MWCNT and SAHA-modified MWCNT are designated as epoxy/MWCNT(0.5 wt%) and epoxy/MWCNT (0.1, 0.25, 0.5, 0.75, 1, 1.5 and 2 wt%)/SAHA, respectively.

For comparison the epoxy composite with SAHA modified MWCNT was also made without using solvent. A typical procedure for nanocomposites prepared without using solvent is described as follows. 0.125 g MWCNT was added into 25 g epoxy resin and stirred for 2 h using mechanical stirrer. The mixture was sonicated for 20 min, keeping the beaker immersed in cold water. The 19 g of Jeffamine 900 was added into it, mixed uniformly for

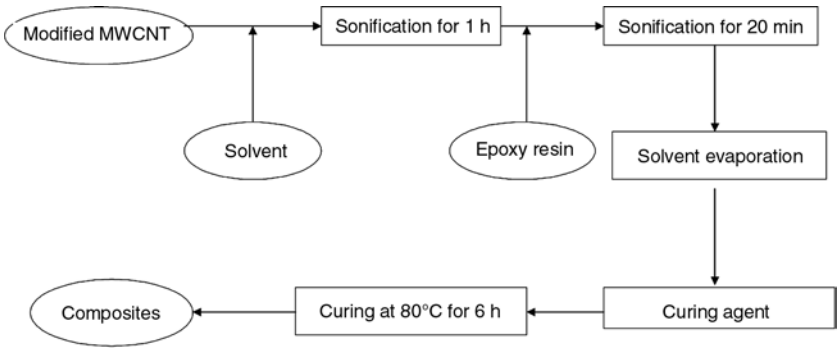

Figure 1. Flow chart of preparation of epoxy/MWCNT nanocomposites by using solvent

15 min, degassed for 10 min and allowed to cure in Teflon mold at 80°C for 6 h.

2.3. Characterization

2.3.1. Tensile properties

The tensile strength, tensile modulus and % elongation at break of neat epoxy and nanocomposites sample were measured using a (Hounsfield 50 KS Instron, UK) Universal Testing Machine (UTM) according to ASTM D 638. The crosshead speed was 100 mm/min and the gauge length was 50 mm. All the tests were performed at 27±2°C and the results are expressed in MPa. The quoted result is an average of the values obtained from four dumbbells.

2.3.2. Microscopic properties

A high resolution scanning electron microscope (FEG-SEM, Zeissa Supra 40 VP, Germany) was used to study the fractured surface morphology of epoxy/MWCNT composite samples. The composite samples were quenched in liquid nitrogen and cryogenically fractured to obtain the cross sections, which were sputter coated with carbon to avoid the charging before the SEM observation. High resolution transmission electron microscope (HRTEM) analysis of the epoxy/MWCNT composite samples was conducted on a JEOL, (JEM-2100, Japan) electron microscope at 200 KV. Ultra-thin sections of composite films were prepared with the thickness of 130–150 nm for TEM imaging using Leica ultracut microtome (Leica Mikrosysteme, GmbH, A-1170, Austria) using liquid nitrogen.

2.3.3. Spectroscopic properties

Fourier transform infrared (FTIR) spectra of MWCNT, SAHA-modified MWCNT and their composite samples were taken with attenuated total reflection (ATR) mode by a Nicolet 510 FTIR spectrometer, Germany over a scanning range from 1000 to 2000 cm^{-1} with a nominal resolution of 2 cm^{-1}. For each spectrum 64 runs were collected and averaged. Raman spectra of unmodified MWCNT, SAHA modified MWCNT and epoxy/MWCNT/SAHA composite samples were recorded using a Renishaw 2000, UK system with an Argon ion laser exciting wavelength of 514 nm over a scanning range of 500–2000 cm^{-1}.

2.3.4. Thermal properties

Thermal behavior of neat epoxy and epoxy/MWCNT composites was studied with DSC (TA instruments Q100 series, USA). About 6–10 mg of sample was placed in an aluminium pan and heated from –80 to 100°C with a heating rate of 5°C·min^{-1} and cooled to room temperature. The reference was an empty aluminium pan. Thermogravimetric analysis (TGA) of neat epoxy and the epoxy/MWCNT composite samples were carried out on a thermogravimetric analyzer, TA Instrument (TGA Q500, USA). 6–8 mg of sample was heated from room temperature to 800°C at a heating rate of 20°C·min^{-1} under nitrogen atmospheres.

2.3.5. Dynamic mechanical analysis

Dynamic mechanical analysis (DMA) of the neat epoxy and epoxy/MWCNT composite samples was carried out using a dynamic mechanical thermal analyzer (MK IV, Rheometric Scientific, USA). The test specimen was cooled to –80°C, allowed to stabilize and then heated at a rate of 3°C/min to 100°C. Liquid nitrogen was used for sub ambient region. Dynamic modulus and loss modulus were obtained by a dual cantilever mode for the sample of size $30 \times 10 \times 2$ mm^3 using a fixed frequency of 1 Hz.

3. Results and discussion

3.1. Reaction of modified MWCNT with the epoxy resin

A good dispersion of MWCNT and interfacial adhesion with the polymer matrix are absolutely necessary to achieve desirable properties of composites. In the absence of sufficient interfacial adhesion between the nanotubes and the polymer, the tubes will be simply pulled-out and will not contribute towards the enhancement of mechanical properties of the composites. We used SAHA to resolve the problem of the good dispersion and interfacial adhesion. SAHA can interact with π electron clouds of MWCNT (via cation-π interaction) which improves dispersion of MWCNT and also it can form chemical bonding with the epoxy resin. In this way, the nanotubes become an integral part of cross linking through chemical bonding between SAHA and epoxy resin. This provides an effective load transfer from epoxy matrices to nanotubes for the enhancement of mechanical properties. The cation-π interaction and chemical modification of MWCNT will be discussed subsequently in spectroscopic analysis section. Schematic representation of the cation-π interaction between SAHA with MWCNT, chemical bonding of amino groups of SAHA with epoxy resin and formation of epoxy network is shown in Figure 2.

3.2. Tensile properties of composites

Table 1 shows the tensile properties of epoxy/MWCNT(0.5 wt%)/SAHA composites, made using two solvents namely acetone and tetrahydrofuran separately. For comparison the composites with 0.5 wt% SAHA modified MWCNT was also made without using solvent (Table 1). The MWCNT to SAHA ratio was maintained as 1:1(w/w). It was observed that the epoxy/MWCNT(0.5 wt%)/SAHA composite made using solvent is much more effective in improvement of tensile properties compared to the composite made without using solvent. This can be attributed to the fact that solvent interacts

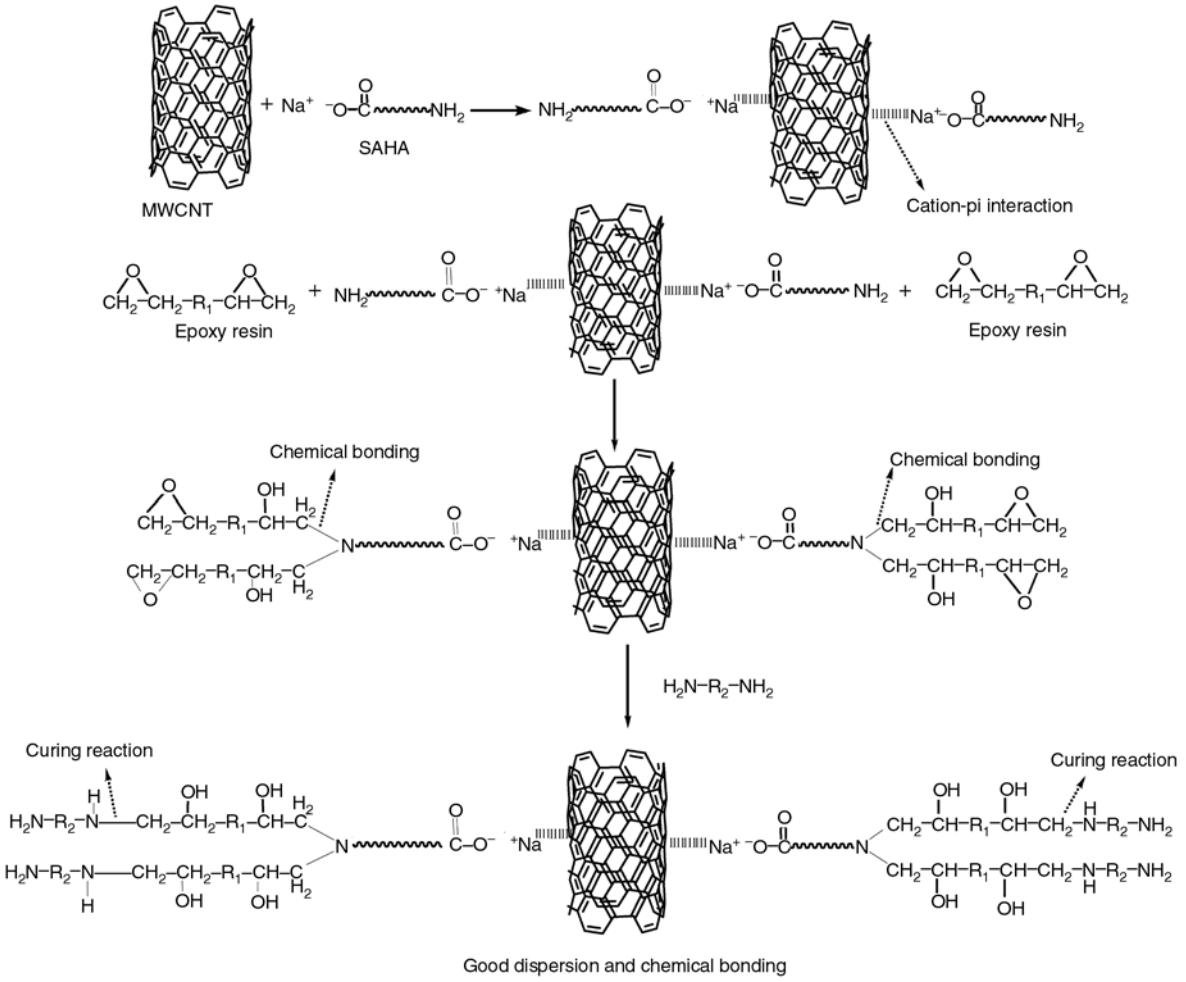

Figure 2. Representation of cation-π interaction (cation of the modifier with π electron clouds of MWCNT) between the modifier (SAHA) with MWCNT and H-bonding of carboxylic acid of SAHA with epoxy

Table 1. Tensile properties of epoxy/MWCNT(0.5 wt%)/SAHA composites prepared by using solvent (THF and acetone) and without using solvent

Samples	Tensile strength [MPa]	Tensile modulus [MPa]	Elongation at breaks [%]
Neat epoxy	0.61±0.02	0.61±0.03	121±7
Epoxy/MWCNT(0.5 wt%)/SAHA (1:1) without solvent	0.81±0.03	0.84±0.05	117±4
Epoxy/MWCNT(0.5 wt%)/SAHA (1:1) in THF	0.94±0.04	1.52±0.08	77±3
Epoxy/MWCNT(0.5 wt%)/SAHA (1:1) in acetone	0.84±0.03	1.11±0.05	85±5

Table 2. Tensile properties of epoxy/MWCNT(0.5 wt%)/SAHA having different ratio (w/w) of MWCNT to SAHA

Samples	Tensile strength [MPa]	Tensile modulus [MPa]	Elongation at breaks [%]
Neat epoxy (100:0:0)	0.61±0.02	0.61±0.03	121±7
Epoxy/MWCNT(0.5 wt%) (100:1:0)	0.72±0.03	0.87±0.02	94±4
Epoxy/MWCNT(0.5 wt%)/SAHA (100:1:0.5)	0.93±0.02	1.38±0.08	73±3
Epoxy/MWCNT(0.5 wt%)/SAHA (100:1:1)	0.94±0.04	1.52±0.06	77±2
Epoxy/MWCNT(0.5 wt%)/SAHA (100:1:1.5)	1.03±0.04	1.65±0.05	75±4
Epoxy/MWCNT(0.5 wt%)/SAHA (100:1:2)	0.79±0.03	1.33±0.04	69±4

strongly with the nanotubes and establishes a stable suspension by breaking the agglomeration of MWCNT. Further, we compared the tensile properties of epoxy/MWCNT(0.5 wt%)/SAHA composites prepared by using THF and acetone. The epoxy/MWCNT(0.5 wt%)/SAHA composite prepared by using tetrahydrofuran showed better performance. This explained that the nature of the solvent is also an important factor to improve the performance of MWCNT in the epoxy matrix. The amine groups of SAHA provides good compatibility with THF compared to the acetone, this leads to debundling of MWCNT and stable suspension of MWCNT. About 54 and 150% improvement in tensile strength and tensile modulus was obtained for composite prepared using THF. In this case, only 20 wt% of solvent was used (low molecular weight) for composites preparation, which is much less compared to that used for thermoplastics composite (>90%). From the above results, THF was used as a solvent for further synthesis and characterization of epoxy/MWCNT composites.

The tensile properties of epoxy/MWCNT(0.5 wt%)/SAHA composites were made with different MWCNT to SAHA ratio is presented in Table 2. The ratios of MWCNT to SAHA were maintained as 1:0.5, 1:1, 1:1.5, and 1:2 (w/w). Among all the composites, the composites prepared by using 1:1.5 MWCNT to SAHA ratio showed the best improvement in the tensile strength and tensile modulus (Table 2). It exhibited around 68 and 170% improvement in the tensile strength and tensile modulus, respectively. This indicates that the addition of optimum concentration (1:1.5) of SAHA and MWCNT resulted in a significant improvement in tensile properties of the composites. This improvement in the tensile property is a combined effect of improved dispersion of MWCNT in the epoxy resin and chemical bonding between the SAHA and the epoxy resin. The good dispersion of MWCNT can be explained in terms of cation-π interaction between cation of SAHA and π electron of MWCNT. This type of interaction reduces the Van der Waals interaction present within the nanotubes and promotes their debundling. Beyond the optimum concentration of modifier (1:1.5), it does not contribute towards improvement in dispersion and interfacial adhesion, but interfere in curing reaction because of the presence of free amine group. This increases the stoichiometric imbalance in the epoxy/reaction, resulting in deterioration in properties. Similar observation was reported in literature [18]. Hence, 1:1.5 MWCNT to SAHA ratio (referred as SAHA modified MWCNT) was considered as an optimum one and the same was used further for preparation of varying concentration of epoxy/MWCNT composites.

A series of epoxy/MWCNT composites were made using varying concentration of SAHA modified MWCNT and their tensile properties were evaluated. The representative stress-strain curve of neat epoxy, epoxy/MWCNT(0.5 wt%), and epoxy/MWCNT(0.5 wt%)/SAHA composites are presented in Figure 3 and the tensile properties are

Table 3. Tensile properties of epoxy/MWCNT/SAHA (1:1.5) composite having varying concentration [wt%] of MWCNT

Samples (wt% SAHA modified MWCNT)	Tensile strength [MPa]	Tensile modulus [MPa]	Elongation at breaks [%]
0	0.61±0.02	0.61±0.03	121±7
0.1	0.66±0.02	0.98±0.03	102±6
0.25	0.74±0.04	1.00±0.04	90±3
0.5	1.03±0.04	1.65±0.05	75±4
0.75	1.09±0.02	1.85±0.07	64±2
1	1.16±0.05	2.22±0.05	63±3
1.5	0.96±0.04	1.42±0.06	58±5
2	0.81±0.03	1.40±0.02	50±2

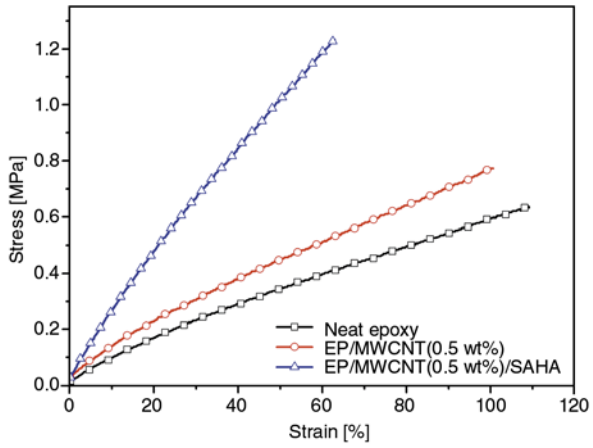

Figure 3. Stress-strain curve of neat epoxy, EP/MWCNT (0.5 wt%) and EP/MWCNT(0.5 wt%) /SAHA

summarized in Table 3. The % elongation at break was found to decrease significantly due to the incorporation of MWCNT into the epoxy matrix (Figure 3). The increased tensile modulus is more prominent in case of modified MWCNT compared to unmodified MWCNT composites. It can be seen that from Table 3, the tensile properties of epoxy/MWCNT composite increased with increasing concentration of MWCNT up to 1 wt % and decreased thereafter. Addition of 1 wt% SAHA modified MWCNT into epoxy matrix showed around 90, and 264% improvement in tensile strength and tensile modulus, respectively. This improvement can be attributed to the good dispersion of MWCNT into the epoxy matrix. The decreased tensile properties of composites beyond 1 wt% due to agglomerated MWCNT, as evidenced by SEM and TEM which will be discussed in subsequent section.

3.3. Microscopic analysis

The epoxy composite prepared using unmodified MWCNT and SAHA modified MWCNT were characterized by SEM to study the dispersion state of MWCNT in the epoxy matrix. The composite samples were cryogenically fractured and the fracture surface was subjected to SEM analysis. Figure 4

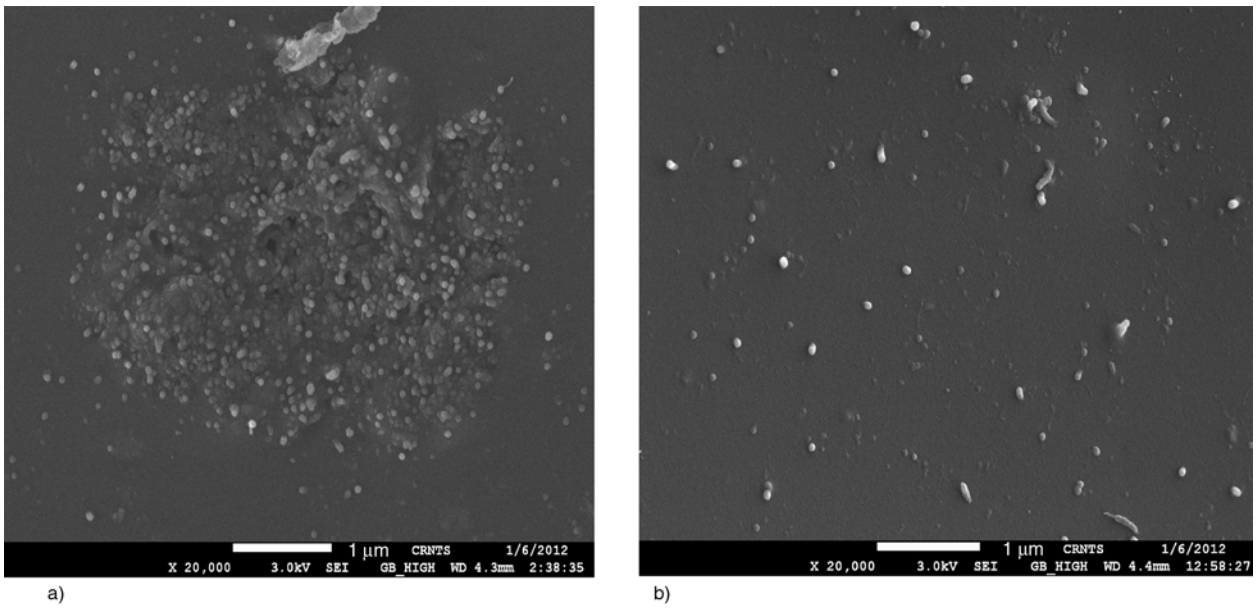

Figure 4. SEM photographs of epoxy/MWCNT composites with (0.5 wt%) (a), unmodified MWCNT and SAHA-modified MWCNT (b)

shows the photographs of epoxy/MWCNT(0.5 wt%) and epoxy/MWCNT(0.5 wt%)/SAHA composite samples. The agglomerated nanotubes can be seen on the fractured surface of the epoxy/MWCNT (0.5 wt%) composite (Figure 4a). The broken ends of unmodified MWCNT simply pulled out from the matrix indicating poor dispersion and absence of interfacial adhesion. On the other hand, the epoxy/MWCNT/SAHA composite showed well dispersed nanotubes throughout the epoxy matrix (Figure 4b). This implies that the modification of MWCNT by SAHA provides not only good dispersion but also good interfacial adhesion.

In order to substantiate the dispersion of MWCNT, the epoxy/MWCNT composite samples were further characterized by TEM. TEM photographs of epoxy/MWCNT, epoxy/MWCNT(0.5 wt%)/SAHA, epoxy/MWCNT(1 wt%)/SAHA and epoxy/MWCNT (1.5 wt%)/SAHA composites are shown in Figure 5. Epoxy/MWCNT(0.5 wt%) clearly demonstrate poor dispersion of MWCNT and high degree of agglomeration (Figure 5a). The well separated nanotubes can be seen for the epoxy/MWCNT (0.5 wt%)/SAHA and epoxy/MWCNT(1 wt%) /SAHA composites (Figure 5b and 5c). This can be explained by considering fact that the debundling of nanotubes due to the cation-π interaction and chemical bonding as described in Figure 2. TEM photograph of epoxy/MWCNT(1.5 wt%) /SAHA composite indicates that at higher concentration of MWCNT it is difficult to prevent the agglomeration. This explains why tensile property decreases beyond 1 wt% MWCNT as discussed earlier.

3.4. Spectroscopic analysis

Raman spectrum for MWCNT, SAHA modified MWCNT and epoxy/MWCNT(1 wt%)/SAHA composite is shown in Figure 6. The spectrum of unmodified MWCNT shows two characteristics peak of *G* and *D* band. The *D* band of MWCNT arises due to

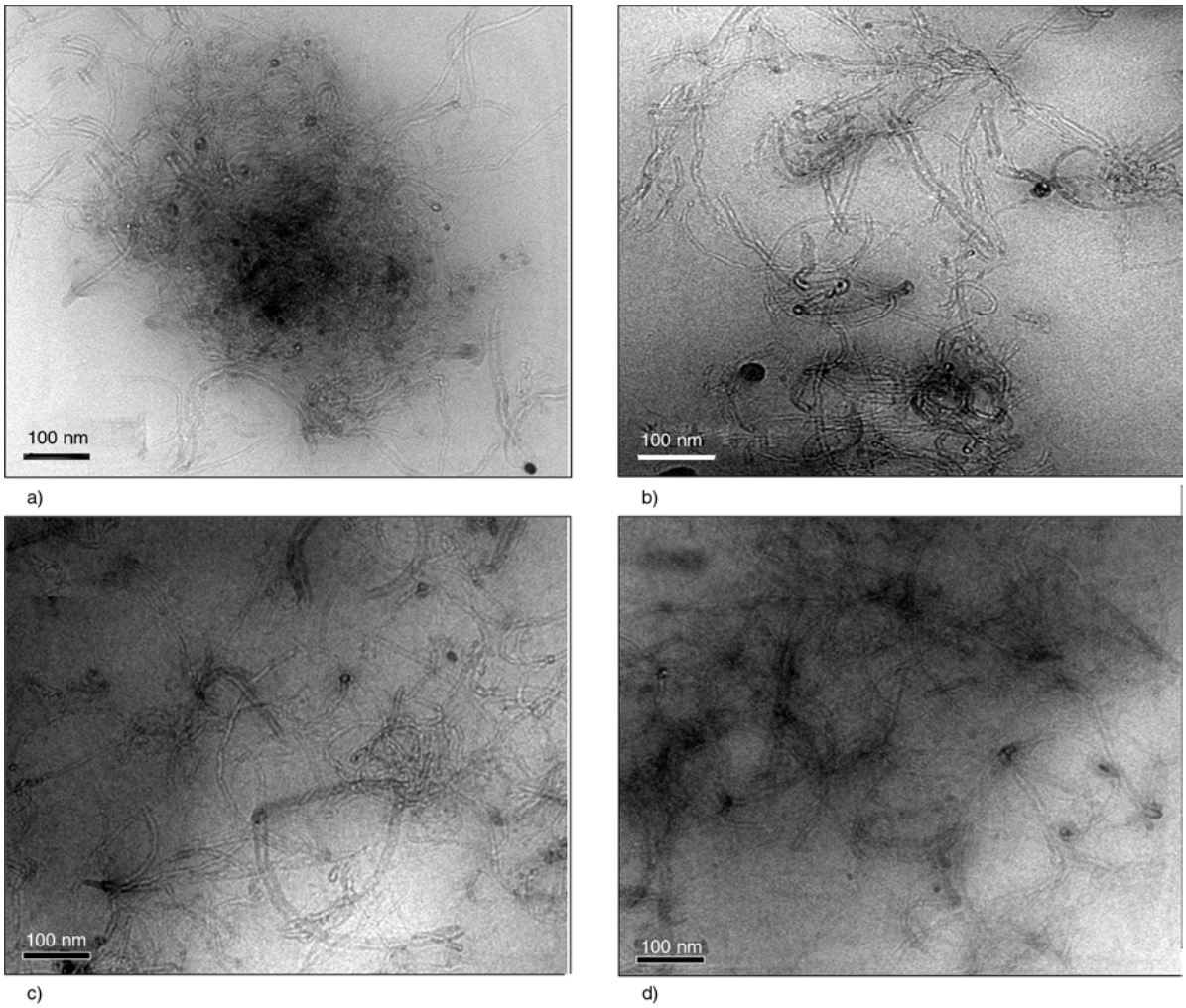

Figure 5. TEM photographs of epoxy /MWCNT composites (a) unmodified-MWCNT(0.5 wt%); (b) (0.5 wt%) SAHA-modified MWCNT, (c) (1 wt%) SAHA-modified MWCNT and (d) (1.5 wt%) SAHA modified MWCNT

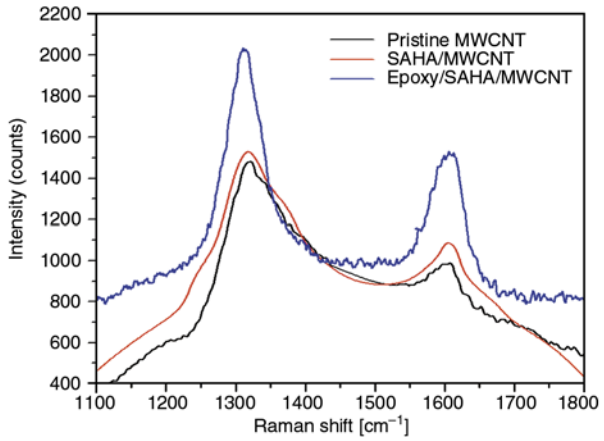

Figure 6. Raman spectra for pristine MWCNT, SAHA modified MWCNT and epoxy/SAHA/MWCNT composite

the disorder graphitic structure, and corresponding *G* band is due to tangential stretching of carbon carbon bond. There is no shift in the peak position of *G* band and *D* band of MWCNT, when MWCNT mixed with SAHA. This observation confirms that the modification of MWCNT with SAHA did not generate any defect on to the surface of MWCNT. It was also observed that upon modification the peak intensity of *G* and *D* band shifted towards higher intensity. Epoxy/MWCNT/SAHA composite also shows the higher peak intensity of *G* and *D* band of MWCNT compared to the unmodified MWCNT and SAHA modified MWCNT. The higher peak intensity of MWCNT after modification can be explained by considering the cation-π interaction (between SAHA and MWCNT) which is responsible for reduction of Van der Waals force within the MWCNT resulting in their good dispersion in polymer matrix [18, 27].

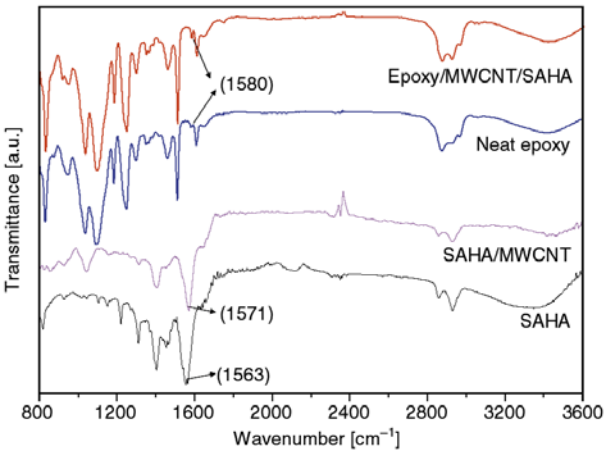

Figure 7. FTIR spectra for SAHA, SAHA modified MWCNT, neat epoxy and epoxy/MWCNT(1 wt%)/SAHA composite

The FTIR spectra of SAHA, SAHA modified MWCNT, neat epoxy and epoxy/MWCNT(1 wt%)/SAHA composite samples are presented in Figure 7. The SAHA shows a characteristic peaks at 1563 cm^{-1} corresponds to C=O stretching of carboxylate group. The C=O stretching peak of carboxylate group is shifted from 1563 to 1571 cm^{-1} for SAHA modified MWCNT. This can be explained by considering the cation-π interaction between the SAHA and MWCNT. The cation of SAHA interact with π electron cloud of MWCNT and reduces the effectiveness of dislocation of negative charge on oxygen atom of the carboxylate ion by reducing the electron density on the charged oxygen atom; resulting in higher wave number of the carboxylate group. The epoxy/MWCNT(0.5 wt%)/SAHA composite also exhibits a shift of the peak of corresponding C=O group of the carboxylate ion from 1563 to 1580 cm^{-1}. It can be noted that the less intense peak at 1580 cm^{-1} appear also in case of the neat epoxy which corresponds to Ar–C=C–H stretching. The same peak obtained for epoxy/MWCNT(0. 5wt%)/SAHA composite has stronger intensity. This can be attributed to overlapping of carboxylate ion peak and Ar–C=C–H group stretching in this region.

3.5. Thermal analysis

Table 4 shows glass transition temperature of the neat epoxy, epoxy/MWCNT and epoxy/MWCNT/SAHA composites measured by DSC and DMA. It was observed that the T_g of all composite sample shifted towards the lower temperature compared to T_g of the neat epoxy which will be discussed in DMA analysis in subsequent section. In order to study the effect of addition of the modified MWCNT on the thermal stability of composites, the neat epoxy and the epoxy/MWCNT/SAHA composite samples were subjected to TGA and results are shown in Figure 8. It can be seen that, the epoxy/MWCNT/

Table 4. Glass transition temperature of neat epoxy and epoxy/MWCNT composites measured by DSC and DMA

Sample	DSC T_g [°C]	DMA T_g [°C]
Neat epoxy	–8	5
Epoxy/MWCNT(0.5 wt%)	–7	6
Epoxy/MWCNT(0.5 wt%)/SAHA	–10	3
Epoxy/MWCNT(0.75 wt%)/SAHA	–10	2
Epoxy/MWCNT(1 wt%)/SAHA	–13	1
Epoxy/MWCNT(1.5 wt%)/SAHA	–11	4

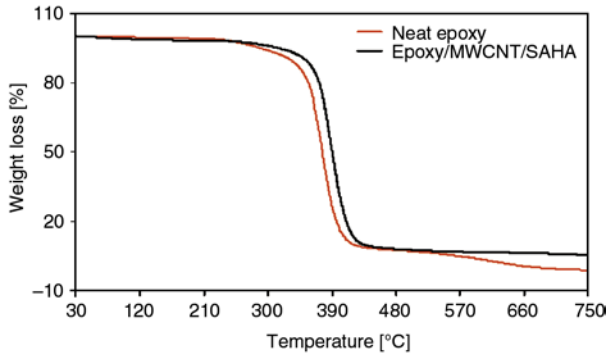

Figure 8. TGA plots of neat epoxy and epoxy/MWCNT/SAHA composite

SAHA composite exhibited higher thermal stability compared to the neat epoxy. This improvement in the thermal stability of the epoxy/MWCNT composite is due to well dispersed nanotubes and strong interfacial adhesion between nanotubes and epoxy matrix. The strong interfacial adhesion of MWCNT with epoxy matrix reduces the mobility of the epoxy matrix around the nanotubes and thereby enhances the thermal stability [28].

3.6. Dynamic mechanical analysis

The storage modulii as a function of temperature for the neat epoxy, epoxy/MWCNT(0.5 wt%), epoxy/MWCNT(0.5 wt%)/SAHA, epoxy/MWCNT(1 wt%) and epoxy/MWCNT(1.5 wt% SAHA) composite are shown in Figure 9. The epoxy/MWCNT(0.5 wt%) composite exhibits the moderate improvement in the storage modulus compared to the neat epoxy. This can be explained by the inert surface of unmodified MWCNT cannot make any kinds of interaction with epoxy matrix (Figure 4 and Figure 5). On the other hand, epoxy/MWCNT(0.5 wt%)/SAHA and epoxy/MWCNT(1 wt%)/SAHA composites show significant improvement in the storage modulus. This is due to the reinforcing effect of MWCNT. The reinforcing effect is a result of good dispersion and strong interfacial adhesion (chemical bonding) between nanotubes and epoxy matrix. The good dispersion of MWCNT is believed to originate from the cation-π interaction and interfacial adhesion due to the chemical bonding of SAHA and epoxy matrix (Figure 2). The lowering of storage modulus in case of epoxy/MWCNT(1.5 wt%)/SAHA compared to epoxy/MWCNT(1 wt%)/SAHA composites clearly indicated that reinforcing effect of MWCNT decreased when concentration of MWCNT goes beyond 1 wt%. This supports the tensile, SEM and TEM results as discussed earlier.

The loss tangent vs. temperature plot of neat epoxy, epoxy/MWCNT(0.5 wt%), epoxy/MWCNT(0.5 wt%)/SAHA, epoxy/MWCNT(1 wt%)/SAHA and epoxy/MWCNT(1.5 wt%)/SAHA are shown in Figure 10. All the composites show reduction in the tan δ peak height due to the addition of MWCNT. This indicates that the restricted mobility of polymer chain which increases rigidity and stiffness of the composites. The moderate reduction in the tan δ peak height in case of epoxy/MWCNT composite indicates the absence of any interaction (cation-π and chemical bonding) between MWCNT with epoxy matrix. On the other hand, a significant decrease in the tan δ peak height was observed due to the addition SAHA modified MWCNT (Figure 10). This is because SAHA modified MWCNTs (well dispersed) restrict the segmental motion of the epoxy around the nanotubes surface. The glass transition temperature of neat epoxy and all the composite samples are listed in Table 4. It can be noted that the glass transition temperature (T_g) tends to decrease due to

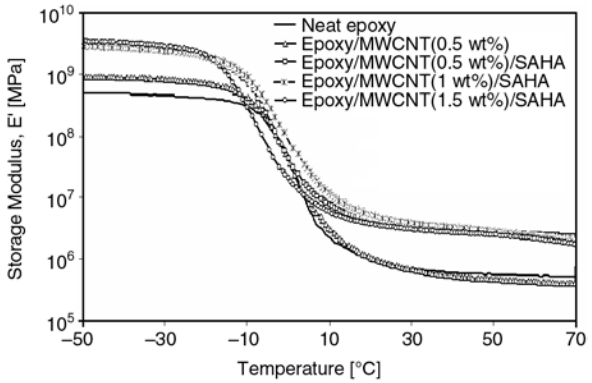

Figure 9. Storage modulus vs. temperature plots for neat epoxy, epoxy/MWCNT(0.5 wt%), epoxy/MWCNT (0.5 wt%)/SAHA, epoxy/MWCNT(1 wt%)/SAHA and epoxy/MWCNT(1.5 wt%)/SAHA

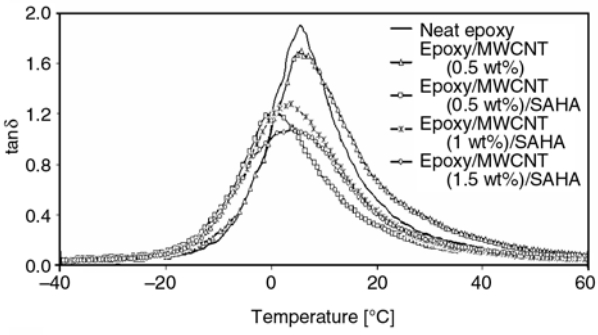

Figure 10. Loss tangent vs. temperature plots for neat epoxy, epoxy/MWCNT(0.5 wt%), epoxy/MWCNT (0.5 wt%)/SAHA, epoxy/MWCNT(1 wt%)/SAHA and epoxy/MWCNT(1.5 wt%)/SAHA

the addition of SAHA modified MWCNT compared to neat epoxy. The lowering of T_g is due to the reaction of amine group of SAHA with epoxy resin resulting non-stoichiometric balance between epoxy resins and curing agent, and thus leading to the inhibition of crosslinking reaction to a certain extent between them [29].

4. Conclusions

A detailed study on effect of SAHA modified MWCNT on tensile properties; thermomechanical properties and dispersion of MWCNT have been conducted. The dispersion of MWCNT in the epoxy matrix is significantly improved due to the use of SAHA as a modifier. The addition of optimum concentration of modified MWCNT(1 wt%) resulted in around 90 and 264% improvement in the tensile strength and tensile modulus, respectively. The good dispersion of MWCNT is a result of cation-π interaction between SAHA and MWCNT. The present approach does not disturb the π electron cloud of CNT as opposed to chemical functionalization.

References

[1] Iijima S.: Helical microtubules of graphitic carbon. Nature, **354**, 56–84 (1991).
DOI: 10.1038/354056a0

[2] Schaefer W. D., Justice S. R.: How nano are nanocomposites? Macromolecules, **40**, 8501–8517 (2007).
DOI: 10.1021/ma070356w

[3] Treacy M. M. J., Ebbesen T. W., Gibson J. M.: Exceptionally high Young's modulus observed for individual carbon nanotubes. Nature, **381**, 678–680 (1996).
DOI: 10.1038/381678a0

[4] Gojny F. H., Nastalczyk J., Roslaniec Z., Schulte K.: Surface modified multi-walled carbon nanotubes in CNT/epoxy-composites. Chemical Physics Letters, **370**, 820–824 (2003).
DOI: 10.1016/S0009-2614(03)00187-8

[5] Haggenmueller R., Gommans H. H., Rinzler A. G., Fischer J. E., Winey K. I.: Aligned single-wall carbon nanotubes in composites by melt processing methods. Chemical Physics Letters, **330**, 219–225 (2000).
DOI: 10.1016/S0009-2614(00)01013-7

[6] Dalton A. B., Collins S., Muñoz E., Razal J. M., Ebron V. H., Ferraris J. P., Coleman J. N., Kim B. G., Baughman R. H.: Super-tough carbon-nanotube fibres. Nature, **423**, 703 (2003).
DOI: 10.1038/423703a

[7] Kumar S., Doshi H., Srinivasarao M., Park J. O., Schiraldi D. A.: Fibers from polypropylene/nano carbon fiber composites. Polymer, **43**, 1701–1703 (2002).
DOI: 10.1016/S0032-3861(01)00744-3

[8] Lozano K., Yang S., Jones R. E.: Nanofiber toughened polyethylene composites. Carbon, **42**, 2329–2331 (2004).
DOI: 10.1016/j.carbon.2004.03.021

[9] Hill D. E., Lin Y., Rao A. M., Allard L. F., Sun Y-P.: Functionalization of carbon nanotubes with polystyrene. Macromolecules, **35**, 9466–9471 (2002).
DOI: 10.1021/ma020855r

[10] Hong C-Y., You Y-Z., Pan C-Y.: Functionalized multiwalled carbon nanotubes with poly(*N*-(2-hydroxypropyl)methacrylamide) by RAFT polymerization. Journal of Polymer Science Part A: Polymer Chemistry, **44**, 2419–2427 (2006).
DOI: 10.1002/pola.21341

[11] Kong H., Gao C., Yan D.: Functionalization of multiwalled carbon nanotubes by atom transfer radical polymerization and defunctionalization of the products. Macromolecules, **37**, 4022–4030 (2004).
DOI: 10.1021/ma049694c

[12] Du J-H., Bai J., Cheng H-M.: The present status and key problems of carbon nanotube based polymer composites. Express Polymer Letters, **1**, 253–273 (2007).
DOI: 10.3144/expresspolymlett.2007.39

[13] Zhao B., Hu H., Yu A., Perea D., Haddon R. C.: Synthesis and characterization of water soluble single-walled carbon nanotube graft copolymers. Journal of the American Chemical Society, **127**, 8197–8203 (2005).
DOI: 10.1021/ja042924i

[14] Qu L., Lin Y., Hill D. E., Zhou B., Wang W., Sun X., Kitaygorodskiy A., Suarez M., Connell J. W., Allard L. F., Sun Y-P.: Polyimide-functionalized carbon nanotubes: Synthesis and dispersion in nanocomposite films. Macromolecules, **37**, 6055–6060 (2004).
DOI: 10.1021/ma0491006

[15] Fukushima T., Kosaka A., Ishimura Y., Yamamoto T., Takigawa T., Ishii N., Aida T.: Molecular ordering of organic molten salts triggered by single-walled carbon nanotubes. Science, **300**, 2072–2074 (2003).
DOI: 10.1126/science.1082289

[16] Kodgire P. V., Bhattacharyya A. R., Bose S., Gupta N., Kulkarni A. R., Misra A.: Control of multiwall carbon nanotubes dispersion in polyamide 6 matrix: An assessment through electrical conductivity. Chemical Physics Letters, **432**, 480–485 (2006).
DOI: 10.1016/j.cplett.2006.10.088

[17] Ratna D., Abraham T. N., Siengchin S., Karger-Kocsis J.: Novel method for dispersion of multiwall carbon nanotubes in poly(ethylene oxide) matrix using dicarboxylic acid salts. Journal of Polymer Science Part B: Polymer Physics, **47**, 1156–1165 (2009).
DOI: 10.1002/polb.21713

[18] Jagtap S. B., Kushwaha R. K., Ratna D.: Poly(ethylene oxide)-multiwall carbon nanotube composites: Effect of dicarboxylic acid salt-based modifiers. Journal of Applied Polymer Science, in press (2013).
DOI: 10.1002/app.38112

[19] Sandler J., Shaffer M. S. P., Prasse T., Bauhofer W., Schulte K., Windle A. H.: Development of a dispersion process for carbon nanotubes in an epoxy matrix and the resulting electrical properties. Polymer, **40**, 5967–5971 (1999).
DOI: 10.1016/S0032-3861(99)00166-4

[20] Schadler L. S., Giannaris S. C., Ajayan P. M.: Load transfer in carbon nanotube epoxy composites. Applied Physics Letters, **73**, 3842–3844 (1998).
DOI: 10.1063/1.122911

[21] Guadagno L., De Vivo B., Di Bartolomeo A., Lamberti P., Sorrentino A., Tucci V., Vertuccio L., Vittoria V.: Effect of functionalization on the thermo-mechanical and electrical behavior of multi-wall carbon nanotube/epoxy composites. Carbon, **49**, 1919–1930 (2011).
DOI: 10.1016/j.carbon.2011.01.017

[22] Tanaka M., Taguchi J., Kato R.: Effects of microstructures on the creep-rupture properties and fracture mechanisms in austenitic heat-resistant steels. Materials Science and Engineering: A, **410–411**, 79–84 (2005).
DOI: 10.1016/j.msea.2005.08.007

[23] Zhou W., Du Z-J., Liu Y-X., Yang X., Li H-Q., Zhang C.: Functionalization of MWNTs using polyacryloyl chloride and the properties of CNT–epoxy matrix nanocomposites. Composites Science and Technology, **68**, 3259–3264 (2008).
DOI: 10.1016/j.compscitech.2008.08.011

[24] Ma P. C., Kim J-K., Tang B. Z.: Effects of silane functionalization on the properties of carbon nanotube/epoxy nanocomposites. Composites Science and Technology, **67**, 2965–2972 (2007).
DOI: 10.1016/j.compscitech.2007.05.006

[25] Yang Z., McElrath K., Bahr J., D'Souza N. A.: Effect of matrix glass transition on reinforcement efficiency of epoxy-matrix composites with single walled carbon nanotubes, multi-walled carbon nanotubes, carbon nanofibers and graphite. Composites Part B: Engineering, **43**, 2079–2086 (2012).
DOI: 10.1016/j.compositesb.2012.01.049

[26] Ratna D., Manoj N. R., Chandrasekhar L., Chakraborty B. C.: Novel epoxy compositions for vibration damping applications. Polymers for Advanced Technologies, **15**, 583–586 (2004).
DOI: 10.1002/pat.513

[27] Bose S., Bhattacharyya A. R., Khare R. A., Kulkarni A. R., Patro T. U., Sivaraman P.: Tuning the dispersion of multiwall carbon nanotubes in co-continuous polymer blends: A generic approach. Nanotechnology, **19**, 335704/1–335704/8 (2008).
DOI: 10.1088/0957-4484/19/33/335704

[28] Cao Y., Feng J., Wu P.: Preparation of organically dispersible graphene nanosheet powders through a lyophilization method and their poly(lactic acid) composites. Carbon, **48**, 3834–3839 (2010).
DOI: 10.1016/j.carbon.2010.06.048

[29] Shen J., Huang W., Wu L., Hu Y., Ye M.: The reinforcement role of different amino-functionalized multi-walled carbon nanotubes in epoxy nanocomposites. Composites Science and Technology, **67**, 3041–3050 (2007).
DOI: 10.1016/j.compscitech.2007.04.025

eXPRESS Polymer Letters Vol.7, No.4 (2013) 340–354
Available online at www.expresspolymlett.com
DOI: 10.3144/expresspolymlett.2013.31

Reactive processing of maleic anhydride-grafted poly(butylene succinate) and the compatibilizing effect on poly(butylene succinate) nanocomposites

Y. J. Phua[1,2], *W. S. Chow*[1,2], *Z. A. Mohd Ishak*[1,2*]

[1]Cluster for Polymer Composites, Engineering and Technology Research Platform, Engineering Campus, Universiti Sains Malaysia, 14300 Nibong Tebal, Penang, Malaysia.
[2]School of Materials and Mineral Resources Engineering, Engineering Campus, Universiti Sains Malaysia, 14300 Nibong Tebal, Penang, Malaysia

Received 27 September 2012; accepted in revised form 8 December 2012

Abstract. In this study, maleic anhydride-grafted poly(butylene succinate) (PBS-g-MA) was synthesized via reactive melt-grafting process using different initiator contents. The grafting efficiency was increased with the initiator content, manifested by the higher degree of grafting in PBS-g-MA. The grafting reaction was confirmed through Fourier transform infrared (FTIR) spectroscopy and nuclear magnetic resonance (NMR) spectroscopy. Then, PBS-g-MA was incorporated into organo-montmorillonite (OMMT) filled poly(butylene succinate) (PBS) nanocomposites as compatibilizer. Mechanical properties of PBS nanocomposites were enhanced after compatibilized with PBS-g-MA, due to the better dispersion of OMMT in PBS matrix and the improved filler-matrix interfacial interactions. This was verifiable through X-ray diffraction (XRD), transmission electron microscopy (TEM) and scanning electron microscopy (SEM). Differential scanning calorimetry (DSC) showed that the degree of crystallinity and melting temperature increased after addition of PBS-g-MA. However, the presence of PBS-g-MA did not favor the thermal stability of the nanocomposites, as reported in the thermogravimetry (TGA).

Keywords: *nanocomposites, biodegradable polymers, reinforcements, mechanical properties*

1. Introduction

The production of polymer/organoclay nanocomposites to enhance the performance of materials has been a rapidly expanding field of research. Organo-montmorillonite (OMMT) is one of the commercial organoclays that has been widely utilized as reinforcing filler in polymer nanocomposites [1–3]. Numerous authors have reported on the enhancement in strength and modulus [4–6], gas barrier [7] and flame retardant properties [8–9] of polymer/OMMT nanocomposites. In recent years, attention has been devoted to the nanocomposites based on biodegradable polymers and organoclay due to the increasing awareness on the plastic waste pollution.

Poly(butylene succinate) (PBS) is a biodegradable polyester with many desirable properties including biodegradability, melt processability, thermal and chemical resistance [10–14]. Fujimaki [13] has compared the properties between the biodegradable PBS and the conventional plastic packaging materials. He reported that the yield strength of PBS (Bionolle #1020) was 264% higher than that of low-density polyethylene (LDPE), and was 10.3% higher than that of polypropylene (PP). In this research, OMMT was incorporated into the PBS matrix in order to

*Corresponding author, e-mail: zarifin.ishak@googlemail.com

produce a 'green' nanocomposite, which is focusing on the potential application in the environmental-friendly packaging films. In our previous work, the effects of OMMT loading on the mechanical and rheological properties of biodegradable PBS/OMMT nanocomposites were reported. The optimum mechanical properties of PBS nanocomposites were observed at 2 wt% OMMT loading [15–16]. However, the improvement is rather limited due to the low polarity of PBS, which restricted the dispersion of clay platelets because of the absence of any strong interactions [17]. Therefore, to obtain a homogeneous dispersion of OMMT in PBS matrix has become a major challenge. Compatibilization turns out to be the most potential way to further enhance the properties of PBS/OMMT nanocomposites.

Maleic anhydride (MA)-grafted polymers have been used as compatibilizers in many composite systems, by reason of their polar functional group that will improve the filler-matrix interactions [18–21]. López-Quintanilla *et al*. [22] reported on the better interfacial adhesion between PP and clay after compatibilized with MA-grafted PP, subsequently improved the mechanical properties of the nanocomposites. Kusmono *et al*. [23] discovered that the incorporation of MA grafted styrene-ethylene/butylene-styrene was able to enhance the strength and ductility of polyamide 6/polypropylene nanocomposites. Although studies on PBS nanocomposites are rather abundant [10–12], study on the PBS nanocomposites compatibilized with MA-grafted polymers is rare. To date, PBS-g-MA is not commercially available and there is limited literature reported on this material. In this study, PBS-g-MA was produced through reactive melt-grafting method in the presence of dicumyl peroxide (DCP) as initiator at various contents, i.e. 1 and 1.5 phr. At our previous research, the optimum mechanical properties of PBS nanocomposites were observed at 2 wt% OMMT loading [15–16]. Hence, as an extension of the previous study, PBS-g-MA was added into the 2 wt% OMMT filled PBS nanocomposites, to investigate the effects of initiator content on the grafting efficiency, and its compatibilizing effects on PBS nanocomposites. In addition, the mechanical, thermal and morphological properties of PBS/OMMT nanocomposites were studied.

2. Experimental

2.1. Materials

PBS (Bionolle #1020) was supplied by Showa Highpolymer Co., Ltd., Japan with MFI value of 25 g/10 min (190°C, 2.16 kg) and melting temperature of 115°C. OMMT (Nanomer® I.30TC, Nanocor Inc, USA) with cation exchange capacity (CEC) of 110 mequiv/100 g, containing MMT (70 wt%) intercalated by octadecylamine (30 wt%) was used. DCP (Aldrich Luperox®, purity ≥ 99.0%) from Sigma-Aldrich Inc, USA was used as initiator. MA (purity ≥ 99.8%) was obtained from R&M Chemicals, UK.

2.2. Synthesis of PBS-g-MA

First, PBS, MA and DCP were physically premixed. The reactive grafting process was carried out in an internal mixer (Haake Polydrive R600, Germany) at 135°C for 7 min. Two different PBS-g-MA, varying from the initiator content, labeled as C1 and C2 were produced as shown in Table 1. After that, purification process was carried out. PBS-g-MA was refluxed in chloroform for 4 h, and the hot solution was filtered into cold methanol. The precipitated polymer was washed with methanol several times, in order to remove any unreacted reagents, followed by drying in an oven at 60°C for 24 h. The purified PBS-g-MA was obtained.

Table 1. Compositions for a Preparation of PBS-g-MA

Component	C1	C2
	Amount [phr]	Amount [phr]
PBS	100	100
MA	10	10
DCP	1	1.5

*phr = part per hundred resin

2.3. Degree of grafting determination

The degree of grafting (G_d) for PBS-g-MA was determined through titration. 1 g of purified PBS-g-MA was refluxed in 100 mL of chloroform for 1 h. Then, 10 mL of distilled water were added. It was titrated immediately with 0.025 M potassium hydroxide (KOH) using phenolphthalein as indicator. G_d can be calculated as shown by Equation (1):

$$G_d[\%] = \frac{N(V_1 - V_0)\cdot 98.06}{2\cdot W\cdot 1000}\cdot 100\% \quad (1)$$

where N is the KOH concentration [M], W is the sample weight [g], V_0 and V_1 is the KOH volume [mL] for blank solution and for titration of PBS-g-MA, respectively.

2.4. Fourier transform infrared (FTIR) spectroscopy

FTIR analysis was carried out on the PBS-g-MA at ambient temperature by using Perkin-Elmer Spectrum One FT-IR Spectrometer (USA). It was performed through the scanning wavelength from 4000–550 cm^{-1} with 32 scanning times.

2.5. Nuclear magnetic resonance (NMR) spectroscopy

NMR test were conducted in deuterated chloroform ($CDCl_3$) solution under ambient temperature on a Bruker Avance 300 MHz spectrometer (Germany) with 13.2 µs pulse and acquisition time of 3.0 s. Tetramethylsilane (TMS) was applied as internal chemical shift standard. Two-dimensional correlation spectroscopy (COSY) was recorded with relaxation-delay time of 1.62 s and sweep width of 1930.5 Hz.

2.6. Gel permeation chromatography (GPC)

The molecular weight of PBS was measured by gel permeation chromatography (GPC) analysis. GPC analysis was performed at 40°C on an Agilent Technologies 1200 Series GPC system (USA) equipped with a refractive index detector (RID) and SHODEX K-806M and SHODEX K-802 columns. The calibration of the columns was carried out using a polystyrene standard of known molecular weight and polydispersity. The samples were then dissolved in chloroform at ambient temperature, followed by filtration to eliminate the contaminants. Chloroform was used as the eluent with a flow rate of 0.8 mL/min, and the injected sample volume was 50 µL with a polymer concentration of 1 mg/mL. The weight-average molecular weight (M_w) and number-average molecular weight (M_n) were obtained from the GPC analysis.

2.7. Preparation of nanocomposites

PBS nanocomposites were prepared by the addition of 2 wt% OMMT and 5 wt% PBS-g-MA into the PBS resin. PBS, OMMT and PBS-g-MA were physically premixed and melt-mixed in an internal mixer (Haake PolyDrive R600, Germany) at 135°C for 5 min with a rotary speed of 50 rpm. It was then molded on a compression molding machine (GT 7014-A30C, Taiwan) at 135°C and 3 min into various shapes of specimen.

2.8. Mechanical properties

Mechanical tests were performed using universal testing machine (Instron 3366, Instron Co., Ltd., USA) at 23±2°C and 50±5% relative humidity. Tensile test was carried out using ASTM D638-03 (Type IV) with a gauge length of 50 mm and a cross-head speed of 5 mm/min. Flexural test (three-point bending) was performed according to ASTM D790-03 with a support span length of 50 mm and a cross-head speed of 5 mm/min.

2.9. X-ray diffraction (XRD)

XRD analysis was carried out with PANalytical X'pert Pro Mrd PW2040 XRD diffractometer (Netherlands) in a scan range from 2–10° and 2.0°/min scanning rate. The X-ray source was Cu-K_α radiation with a wavelength (λ) of 0.154 nm. The interlayer spacing of OMMT was calculated from d_{001}-reflections using Bragg's equation: $n\lambda = 2d_{001}\cdot\sin\theta$, where θ is the measured diffraction angle [24].

2.10. Transmission electron microscopy (TEM)

The morphologies of the nanocomposite samples were observed using an Energy Filter Transmission Microscope (EFTEM) (Zeiss Libra 120, Netherlands) operated at 200 kV. The ultrathin sections of sample with the thickness 70–80 nm were prepared via ultramicrotomy technique using Reichert Ultramicrotome Supernova.

2.11. Scanning electron microscopy (SEM)

The tensile-fractured surface of the samples was observed under a field-emission scanning electron microscope (FESEM) (Zeiss LEO Supra 35VP, Germany). Prior to the observations, the samples were sputter-coated with a thin layer of gold to avoid electrical charging during examination.

2.12. Differential scanning calorimetry (DSC)

The DSC analysis was carried out using Perkin-Elmer DSC-6 (USA) machine in a nitrogen atmosphere. Sample was heated from 30 to 150°C at a heating rate of 10°C/min. The sample was then cooled

from 150 to 30°C at a same heating rate. Next, second heating was performed from 30 to 150°C. Finally, it is cooled to 30°C. The thermal behavior of PBS nanocomposites is studied from the second heating and cooling in DSC in order to eliminate the thermal history. Degree of crystallinity (χ_c) was calculated by using Equations (2) and (3):
For pure PBS,

$$\chi_c = \frac{\Delta H_c}{\Delta H_m^0} \cdot 100\% \quad (2)$$

where ΔH_c crystallization enthalpy of sample, ΔH_m^0 melting enthalpy of 100% crystalline PBS (110.3 J/g) [25].
For polymer nanocomposites,

$$\chi_c = \frac{\Delta H_c}{\Delta H_m^0 (1 - W_f)} \cdot 100\% \quad (3)$$

where W_f weight fraction of fillers in the nanocomposite.

2.13. Thermogravimetry (TGA)

TGA was conducted in the Perkin-Elmer Pyris 6 TGA Analyzer (USA) from room temperature to 700°C at the heating rate of 10°C/min under nitrogen atmosphere.

3. Results and discussion

3.1. Characterizations of PBS-g-MA

3.1.1. Degree of grafting (G_d) determination

In the previous study, Mani *et al*. [26] performed the grafting of MA onto PBS by varying the initiator content from 0.3–1.0 wt%. They reported that the grafting efficiency was the highest at 1.0 wt% of initiator. By using this as a reference, in this study, 1.0 and 1.5 phr of initiator was incorporated. Generally, G_d is influenced by various factors such as monomer and initiator concentration, temperature, rotor speed and residence time [26, 27]. In the present research, other parameters were kept constant. Therefore, the changes in G_d are mainly attributed by the initiator concentration. Table 2 shows that C1 possess G_d of 3.89%, while C2 exhibits a G_d of 4.84%. This reveals that the grafting efficiency increased as the initiator content increased, owing to the increase radical formation through the decomposition of initiator. Higher radical concentration would provide higher chain transfer to the polymer backbone and hence, higher the grafting efficiency. Note that high initiator concentration may cause crosslinking to the polymers. C1 and C2 were completely dissolved in chloroform, indicating no crosslinking takes place in the grafting process.
The G_d of PBS-g-MA that synthesized in this work is appeared to be higher than that of the conventional grafted polymers such as MA-grafted PP, with the G_d ranged between 0.5–1.2% [28]. This shows the potential of PBS-g-MA to be applied as compatibilizer in the polymer composite system, with respect to its higher ability to diffuse into the polymer matrix and provide enough sites for attachment to the fillers.
Besides that, the molecular weight of C1 and C2 was determined through gel permeation chromatography (GPC) analysis. The weight-average molecular weight (M_w) and number-average molecular weight (M_n) were determined and shown in Table 2. Based on the datasheet, the initial M_w of the PBS is $1.4 \cdot 10^5$ g/mol. Thus, this shows that as the PBS is grafted with MA, the molecular weight is lowered as a result from chain degradation via the beta-scission reaction [26].

Table 2. Degree of grafting and molecular weight at different initiator concentrations

Compatibilizer	DCP concentration [phr]	Degree of grafting [%]	M_w [g/mol]	M_n [g/mol]
C1	1.0	3.89	28 620	14 450
C2	1.5	4.84	24 620	12 450

3.1.2. Fourier transform infrared (FTIR) spectroscopy

The performance of the grafting process was further evaluated through FTIR spectroscopy, as reported in Figure 1. The peak at 917 cm^{-1} corresponds to the –C–OH bending in the carboxylic acid groups of PBS. The bands at 1044–1046 cm^{-1} were due to

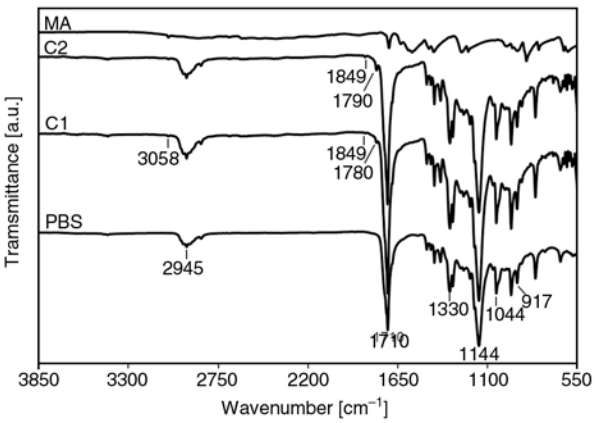

Figure 1. FTIR spectra of PBS, PBS-g-MA and MA

–O–C–C– stretching vibrations in PBS. Peaks in the range of 1144–1264 cm^{-1} resulted from the stretching of the –C–O–C– group in the ester linkages of PBS. The band at the 1710–1713 cm^{-1} region was attributed to the C=O stretching vibrations of ester groups in PBS. Meanwhile, the peaks at 1330 and 2945 cm^{-1} were assigned to the symmetric and asymmetric deformational vibrations of $–CH_2–$ groups in the PBS main chains, respectively [29].

There is a clear signal at the transmittance bands of 1780 and 1849 cm^{-1} in the grafted PBS, while were absent in the neat PBS. These bands are assigned to the symmetric (1780 cm^{-1}) and asymmetric (1849 cm^{-1}) stretching of C=O bonds for the succinic anhydride groups [27, 30]. Higher peak intensities were also observed on C2 at the 1780 and 1849 cm^{-1} bands as compared to C1, corresponded to higher content of succinic anhydride groups in C2. Furthermore, an additional band at 3058 cm^{-1} was found in PBS-g-MA and neat MA, ascribed to the $=CH_2$ vibration in the cyclic MA.

3.1.3. Nuclear magnetic resonance (NMR) spectroscopy

The ^{1}H-NMR spectra of pure PBS and PBS-g-MA are shown in Figure 2. The ^{1}H-NMR resonance signal of pure PBS appearing at 2.55 ppm was associated with the methylene protons (H_a) in the succinic moiety. The resonances at 4.05 and 1.64 ppm were respectively assigned to the methylene protons α (H_b) and β (H_c) in the 1,4-butanediol unit. An additional signal is observed in the PBS-g-MA spectra at approximate 3.7 ppm region (Figure 2b and 2c), which is related to the resonance of the methane proton formed due to the grafting of MA [26]. This supports the evidence that MA is attached to the polymer chains after the reactive grafting process.

The 2D COSY ^{1}H-NMR spectra (Figure 3) provides additional information on the grafting mechanism, which reveals the coupling relationships between the protons presence in the grafted PBS. In Figure 3a, the off-diagonal peaks or cross correlated peaks show a single coupling interaction between the neighboring carbon atoms in the 1,4-butanediol unit (H_{bc}) of pure PBS. A similar coupling interaction is seen in the PBS-g-MA, as shown in Figure 3b and 3c. However, there is an additional coupling interaction between the methine proton of the anhydride with protons of the α carbon atom ($H_{b'}$) in the 1,4-butanediol unit. This result suggests

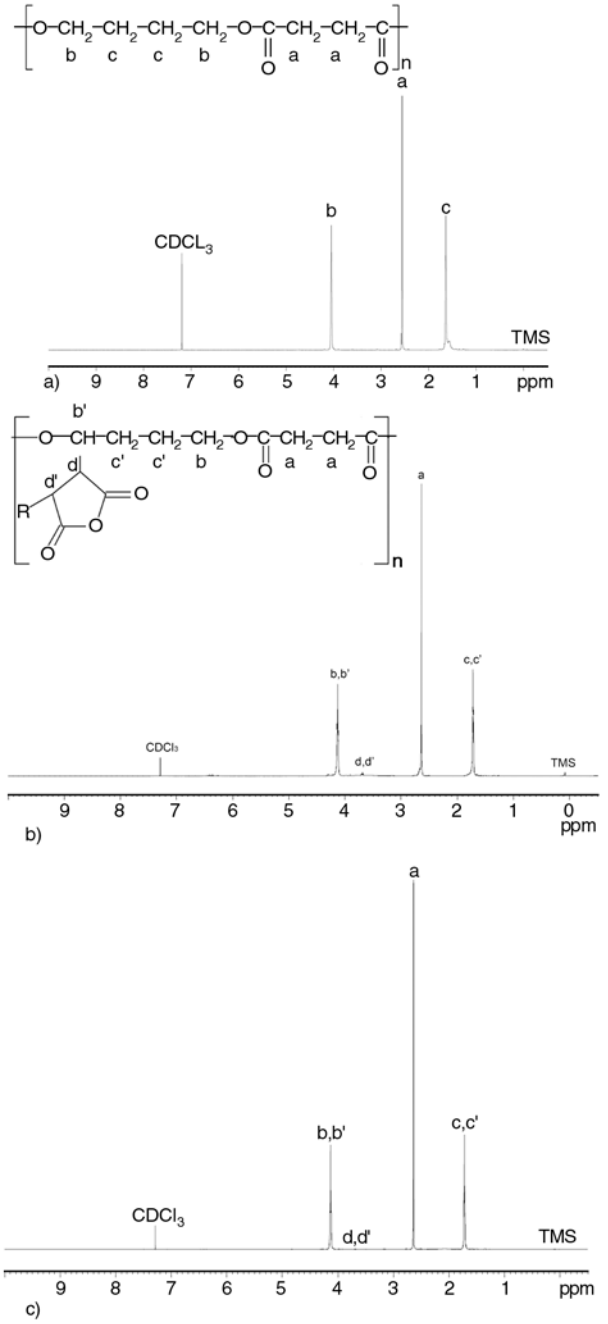

Figure 2. ^{1}H-NMR spectra of (a) pure PBS, (b) C1 and (c) C2

that the grafting reaction take place at the diol unit of PBS, which is proposed in Figure 4. Thus, the COSY ^{1}H-NMR demonstrated a successful construction of the PBS-g-MA product.

Figure 4. represents a proposed scheme of the reactions during the reactive melt grafting of PBS-g-MA. The initiator decomposes at the initial step to form primary radicals (Scheme I). These primary radicals abstract the hydrogen atom from PBS backbone and yield PBS radicals (Scheme II). Scheme III shows the grafting of MA molecules onto the PBS radicals to form PBS-MA radicals, and followed by

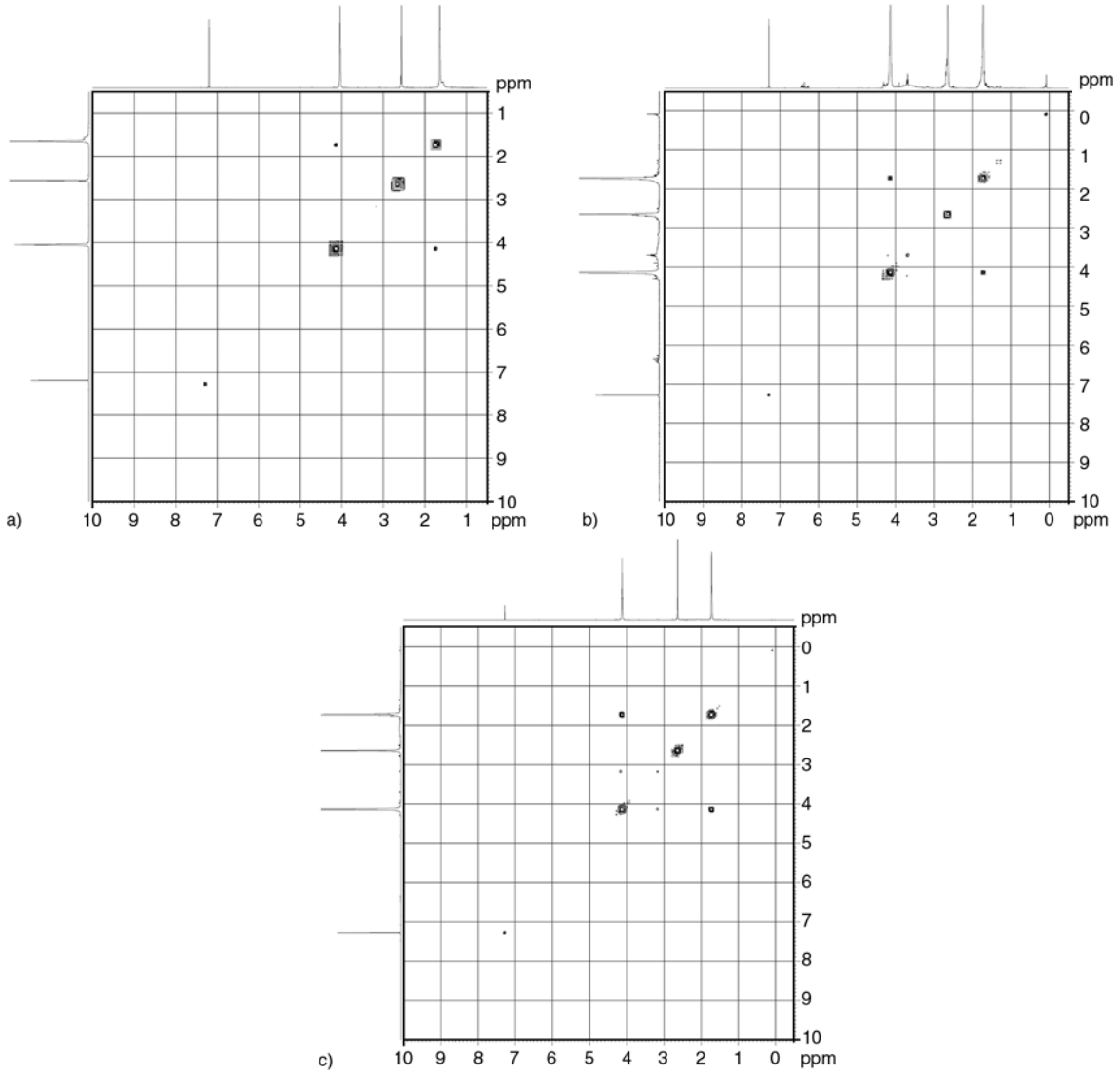

Figure 3. 2D COSY ^{1}H-NMR spectra of (a) pure PBS, (b) C1 and (c) C2

various termination reactions. The PBS-MA radicals might undergo hydrogen transfer from another polymer chains, MA, or the initiator (Scheme IV) and form the final product of PBS-g-MA. Scheme V presents the possible reactions of PBS-MA radicals with other radicals in the system, such as MA, PBS or primary radicals to form a different structure of PBS-g-MA.

3.2. Characterizations of nanocomposites

3.2.1. Mechanical tests

The mechanical properties of PBS nanocomposites are presented in Table 3. It can be seen that the presence of PBS-g-MA decreased the tensile and flexural strength, as well as the elongation at break of PBS. The low molecular weight of PBS-g-MA is believed to responsible for this reduction. It was reported in our previous publication that the mechanical strength and modulus were increased, after incorporation of 2 wt% OMMT into PBS to form a nanocomposite [15]. After compatibilization with C2, tensile and flexural strength of the nanocomposites are improved by 10.4 and 6.1%, respectively. The polar MA groups may interact with the amine groups on the OMMT surface by forming hydrogen bonding on one side, and with the carbonyl groups on the PBS chains on the other side. This may consequently improve the filler-matrix interaction, meanwhile, enhance the filler dispersion through the intercalation of MA groups between the silicate galleries [19, 21, 31]. Besides that, the higher amount of grafted MA contained in C2 is able to provide

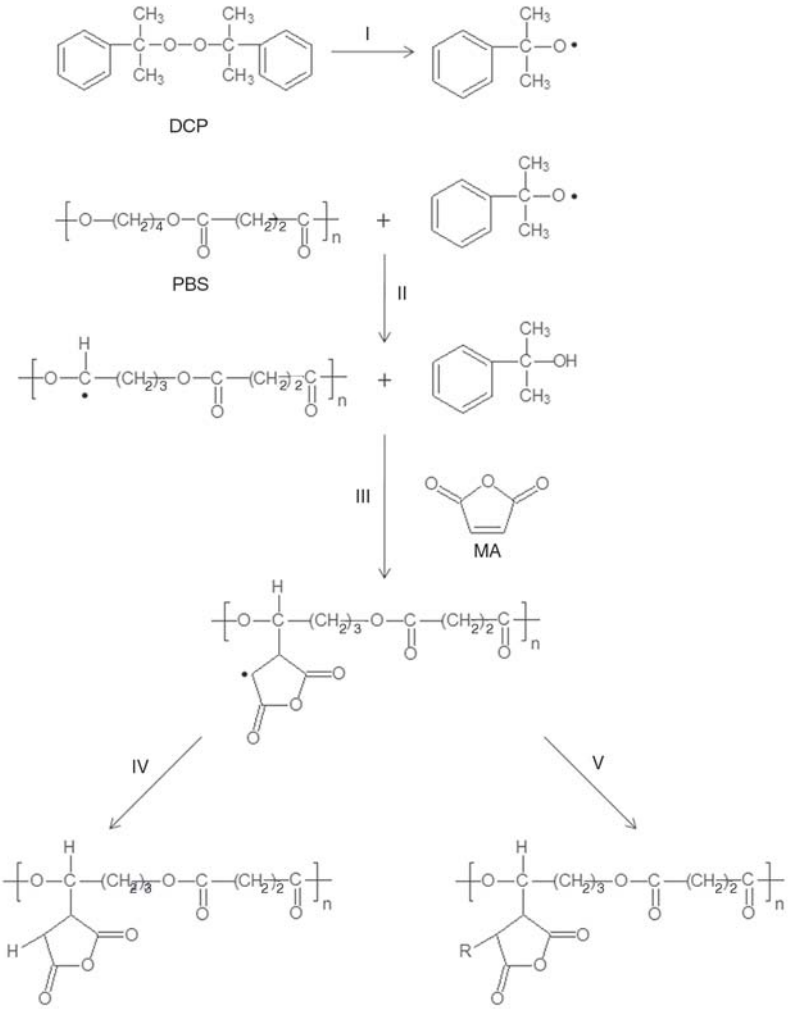

Figure 4. Proposed grafting mechanism of MA onto PBS

Table 3. Mechanical properties of PBS nanocomposites

Properties	Compound					
	PBS	PBS/C1	PBS/C2	PBS/2%OMMT	PBS/2%OMMT/C1	PBS/2%OMMT/C2
Tensile						
Strength [MPa]	32.6±2.7	29.8±0.69	29.0±2.2	33.6±1.2	34.2±1.3	37.1±1.3
Modulus [MPa]	589±6.8	603±12	599±14	631±9.1	634±4.3	650±7.2
Elongation at break [%]	10.9±2.6	6.99±0.45	6.67±1.4	12.9±2.4	10.5±2.0	12.5±1.8
Flexural						
Strength [MPa]	33.3±1.9	31.2±0.80	32.1±1.3	36.1±0.91	38.2±1.2	38.3±0.18
Modulus [MPa]	570±14	595±9.5	598±21	619±11	627±9.4	626±3.9

higher intercalation of the OMMT galleries, which in turn provides a better dispersion of the clay platelets.

The addition of stiff reinforcements, such as OMMT was able to improve both the tensile and the flexural modulus [15–16, 29]. Table 3 shows that the modulus is slightly increased after the incorporation of PBS-g-MA into the nanocomposites. Moreover, nanocomposite compatibilized with C2 exhibits a higher tensile modulus than that of compatibilized with C1. Mishra *et al*. [32] and Tserki *et al*. [27] explained that the intercalation of polymer chains inside the silicate layers led to an increase in the surface area of interaction between the organoclay and polymer matrix, subsequently caused the modulus enhancement. However, the effect of G_d on the flexural strength and modulus is negligible. Nevertheless, the incorporation of PBS-g-MA does not show significant effect on the elongation at break. It is believed that the better interfacial interaction between polymer and organoclay has compensated the negative effect of MA that was often reported to

reduce the elongation at break [22, 32]. The improved matrix-filler interfacial interactions could enhance the stress transfer efficiency from matrix to filler when the composites were subjected to an external load, subsequently yield a higher elongation at break. Hence, the elongation at break in PBS/2%OMMT/C2 was retained. The improvement in mechanical properties could therefore be a combination of improved clay dispersion and interfacial interactions between polymer and clay.

3.2.2. X-ray diffraction (XRD)

The OMMT dispersion in the nanocomposites was studied through the XRD analysis. Figure 5 presents the wide-angle XRD patterns of OMMT and the nanocomposites. A clear peak showing the interlayer spacing associated with the d_{001} plane of MMT was observed. The XRD spectrum of OMMT exhibits a broad intense peak at $2\theta = 3.17°$, corresponding to a d_{001} spacing of 2.79 nm. It is clear that the peaks tend to broaden and shift toward a lower value of 2θ after the formation of nanocomposites, suggesting the formation of intercalated and exfoliated structures in the nanocomposites [33–35]. The XRD patterns of PBS/2%OMMT, PBS/2%OMMT/C1 and PBS/2%OMMT/C2 reveal the diffraction peaks at $2\theta = 2.46$, 2.32 and 2.23°, corresponding to the d_{001} spacing of 3.59, 3.81 and 3.95 nm, respectively.

Addition of PBS-g-MA into the nanocomposites is proven to further facilitate the expansion of gallery space between the organoclay layers. Moreover, nanocomposite compatibilized with C2 shows better OMMT dispersion with larger d_{001} spacing than that with C1. This can be correlated with the greater enhancement in mechanical properties of C2 compatibilized nanocomposite, as discussed earlier.

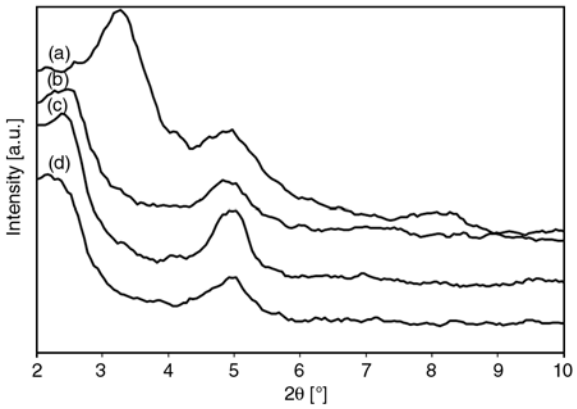

Figure 5. XRD patterns of (a) OMMT, (b) PBS/2%OMMT, (c) PBS/2%OMMT/C1 and (d) PBS/2%OMMT/C2

3.2.3. Transmission electron microscopy (TEM)

TEM images of the nanocomposites are displayed in Figure 6. As observed from Figure 6a, a mixed region of tactoids, stacks of intercalated clay platelets, and individual exfoliated platelets are present in the uncompatibilized nanocomposites. After compatibilization using PBS-g-MA, a higher degree of intercalated and exfoliated clay platelets has been obtained, as presented in Figure 6b and 6c. The clay agglomerations and tactoids were obviously reduced, contributed to better filler dispersion. The TEM images have provided a direct visualization of the improved dispersion of OMMT in PBS matrix, which is in good agreement with the observed mechanical properties and XRD results. It is also noted that C2 compatibilized nanocomposite shown better clay dispersion as compared to C1 compatibilized nanocomposite.

3.2.4. Scanning electron microscopy (SEM)

Figure 7 shows the tensile fractured surface of PBS and its nanocomposites. PBS exhibits a semi-ductile fracture behavior, indicated by the relatively smooth and clear surface with fibrils that formed a web-like structure. In Figure 7b, fractured surface of PBS/2%OMMT nanocomposites reveals a reduction in the fibrillation of PBS, due to the stiffening effect after OMMT addition. This is in agreement with the modulus enhancement as reported previously. Furthermore, distinct phase separation between the OMMT platelets and the PBS matrix is noticeable. The formation of microcavities at the filler-matrix interface is caused by the poor compatibility between PBS and OMMT, which is the main reason of the limited properties enhancement.

Figure 7c and 7d show the tensile fractured surface of the compatibilized nanocomposites. The disappearance of matrix fibrillation from the fracture surface is due to the stiffening effect after incorporation of PBS-g-MA. Besides that, there is no clear filler delamination from the PBS matrix, confirms the improved filler-matrix interactions in the PBS/OMMT nanocomposites after compatibilization.

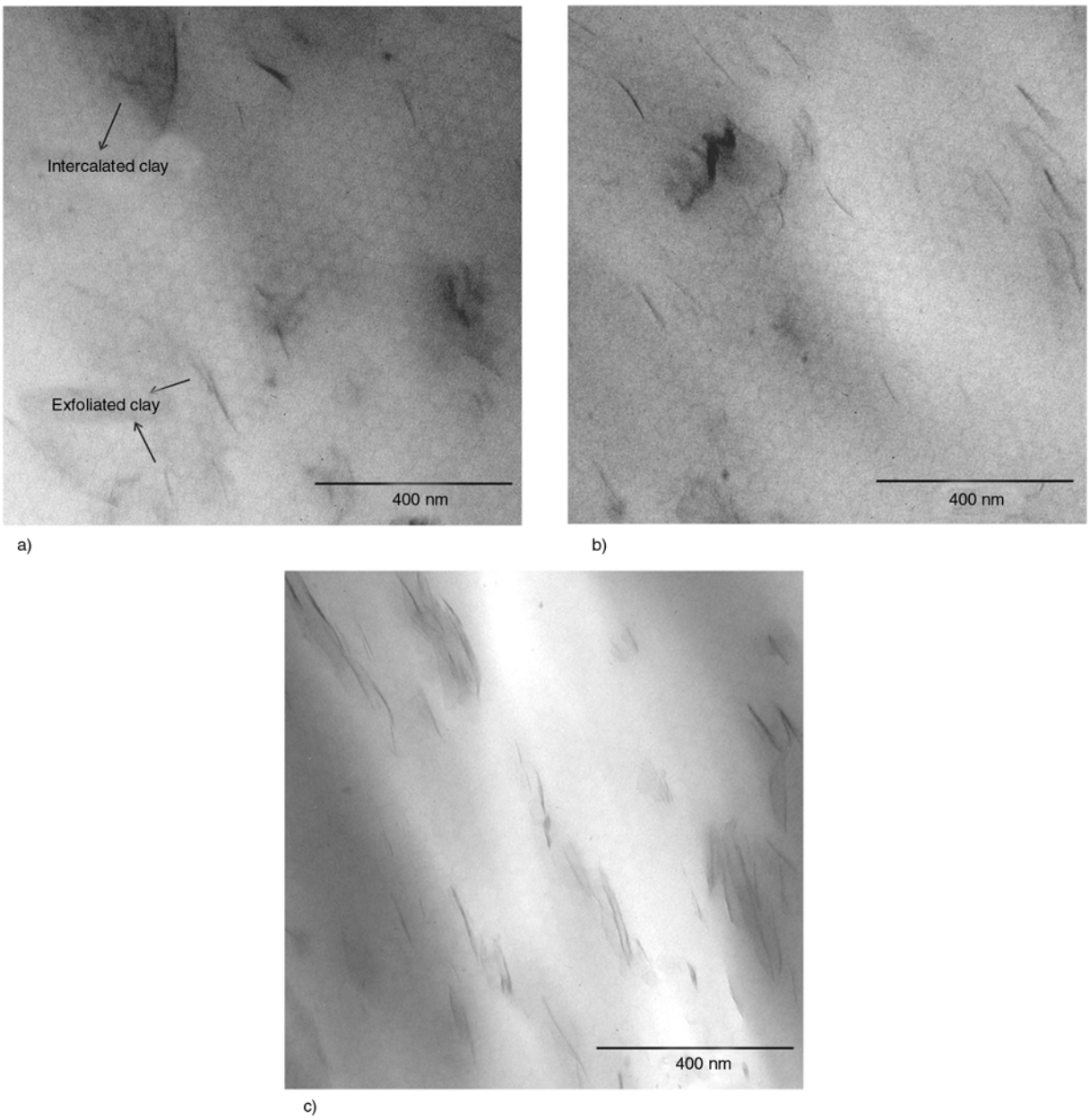

Figure 6. TEM images of (a) PBS/2%OMMT, (b) PBS/2%OMMT/C1 and (c) PBS/2%OMMT/C2

3.2.5. Differential scanning calorimetry (DSC)

The thermal behavior of PBS nanocomposites is studied from the DSC analysis and reported in Figure 8. Figure 8a shows two distinct peaks in the heating scans of PBS and its nanocomposites. Similar observation has been reported by Ray *et al*. [36] and Vega-Baudrit *et al*. [37], where they pointed out the existence of two melting peaks was due to the two different types of crystalline lamella presented in PBS. They suggested that the lower melting endotherm is corresponds to the melting of the original crystallites formed at the isothermal crystallization temperature; while the higher melting endotherm reveals the melting of the recrystallized crystals. Moreover, an exothermic peak, which resulted from the fusion and recrystallization of PBS crystals during heating [38–39], was found for all the samples prior to the second melting endotherm. Table 4 indicates that the incorporation of PBS-g-MA into PBS slightly increased the melting temperature at the low endotherm (T_{m1}). This is assigned to the interfacial chemical reaction between the MA group in PBS-g-MA and carbonyl group in PBS, which affected the melting kinetics of PBS crystals. Melting temperature at the high endotherm (T_{m2}) of PBS did not show any appreciable change after the addition of PBS-g-MA. Moreover, the incorporation of OMMT did not change the T_{m1} and T_{m2} of

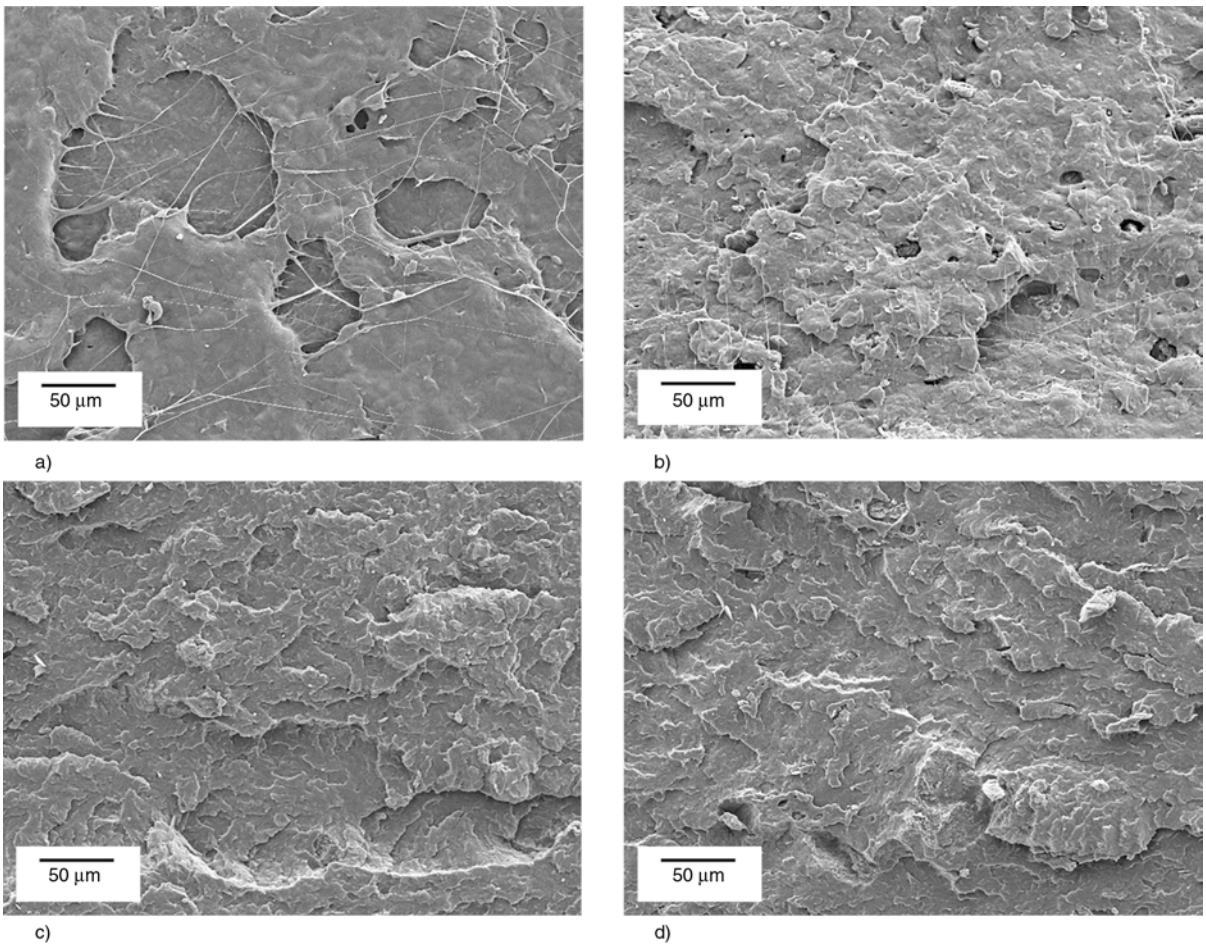

Figure 7. SEM micrographs of the tensile fractured surface of (a) PBS, (b) PBS/2%OMMT, (c) PBS/2%OMMT/C1 and (d) PBS/2%OMMT/C2

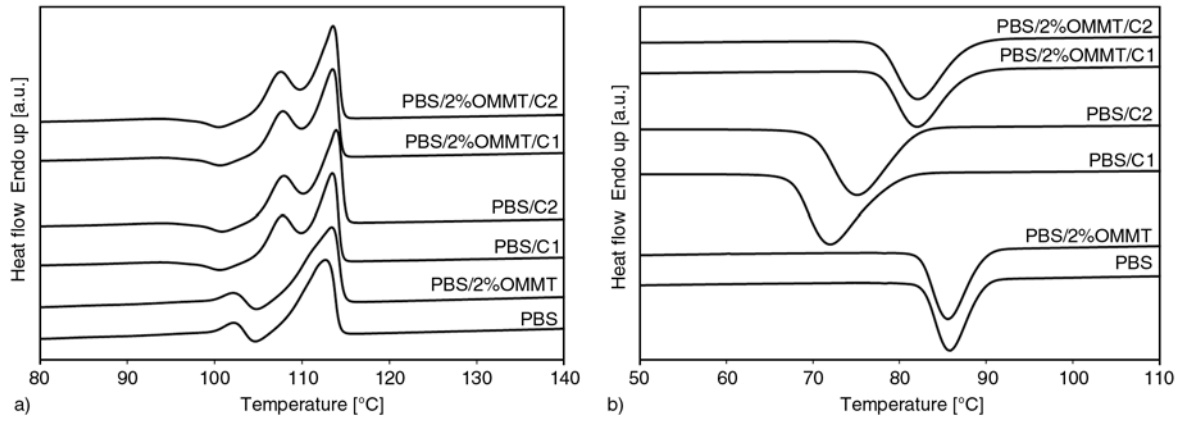

Figure 8. DSC (a) melting and (b) cooling scans of PBS nanocomposites

Table 4. Melting and crystallization behavior of PBS nanocomposites

Compound	T_{m1} [°C]	T_{m2} [°C]	T_c [°C]	χ_c [%]
PBS	102.2	112.4	85.9	57.6
PBS/2%OMMT	102.1	113.4	85.6	55.7
PBS/C1	107.8	113.9	72.1	61.7
PBS/C2	107.9	114.0	75.3	62.5
PBS/2%OMMT/C1	107.6	113.4	82.0	64.8
PBS/2%OMMT/C2	107.4	113.6	82.1	65.9

PBS, which is in line with that reported in our previous publications [15–16].

From Figure 8b, it is noted that the incorporation of OMMT into PBS does not provide a significant change in the crystallization temperature (T_c). However, a slight decreased degree of crystallinity (χ_c) in PBS/2%OMMT nanocomposites has been observed. This is attributed to the physical hindrance of OMMT platelets for the mobility and

flexibility of the polymer chains to fold and join the crystallization growth front [14–15, 29]. An obvious reduction in T_c is observed in the PBS/PBS-g-MA blend, accompanied with a slight improvement in χ_c to 61.7 and 62.5% in the presence of C1 and C2, respectively. The reduction in T_c is attributed to slower crystal growth generated by the interactions between PBS and PBS-g-MA, as mentioned earlier. In addition, the increased χ_c reveals that PBS-g-MA acts as a heterogeneous nucleating agent, creating the nucleating sites for crystallization process to occur [40]. Nanocomposite that compatibilized by C2 exhibits higher χ_c than that compatibilized by C1, owing to the higher G_d of C2. Besides that, the χ_c of nanocomposites is increased by 16.3 and 18.3% after compatibilized with C1 and C2, respectively. Thus, it is understood that the increment in crystallinity could also be partially responsible for the increase in mechanical properties. However, the compatibilized nanocomposites show T_c at ~82 °C, which is higher than that of the PBS/PBS-g-MA blend. A study done by Xu *et al*. [41] claimed that the improved interaction between polymer and organoclay after compatibilization has caused the immobilizing of some polymer chains. This contributes to the crystallization of polymer matrix, leads to the crystallization at a higher T_c. However, the existence of clay platelets may also create a physical hindrance upon the crystal growth. Therefore, the T_c is still lower than that of the neat PBS.

3.2.6. Thermogravimetry (TGA)

The thermal stability of PBS nanocomposites was assessed by TGA, where the sample weight loss due to volatilization of degraded by-products is monitored in function of a temperature ramp, as presented in Figure 9. The TGA curves display a single-stage degradation process starting at ~300°C and ending at ~470°C, which correspondens to the structural decomposition of the polymers. The single-stage decomposition of compatibilized PBS nanocomposites provides an evidence that no formation of crosslinking in the PBS-g-MA. The nanocomposites show a weight loss of 97.4, 98.1 and 97.6%, for the PBS/2DM, PBS/2DM/C1 and PBS/2DM/C2 nanocomposites, respectively. There is approximately 2–3 wt% of char residue remained after the polymer decomposition.

According to the literature, the decomposition temperature can be studied through various points in the TGA curves. In this work, the onset of the decomposition temperature (T_{d5}) was determined by the temperature at 5% weight loss [42–44], whilst the decomposition temperature at the point of greatest rate of change on the weight loss curve (T_{dmax}) was measured through the derivative weight loss curves (Figure 10). Table 5 shows that the addition of OMMT into PBS does not produce any appreciable changes in the T_{d5} and T_{dmax}. This implies that the presence of OMMT does not provide a significant effect in improving the thermal stability as usually reported by numerous researchers [45–48]. Even though the organoclay was often reported on its

Table 5. Thermal stability of PBS nanocomposites

Compound	T_{d5} [°C]	T_{dmax} [°C]
PBS	368.7	411.9
PBS/2%OMMT	371.4	407.8
PBS/C1	372.8	427.4
PBS/C2	369.3	426.0
PBS/2%OMMT/C1	365.4	407.2
PBS/2%OMMT/C2	362.1	407.3

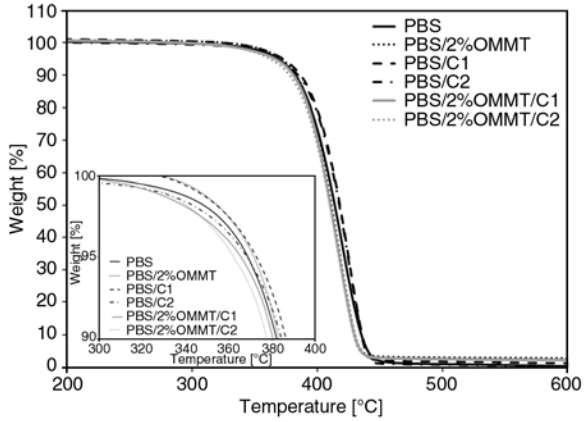

Figure 9. TGA curves of PBS nanocomposites (the insert shows the zoom of the selected area)

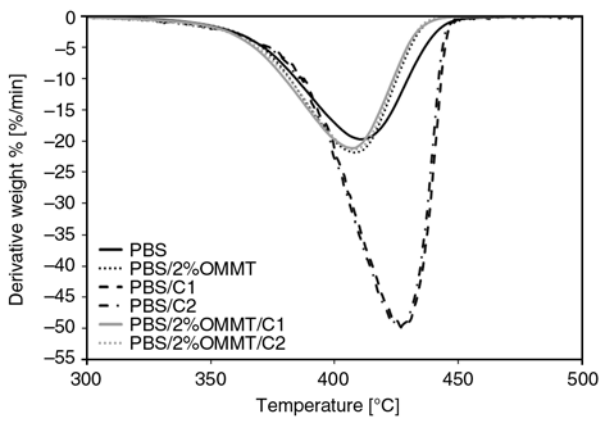

Figure 10. Derivative weight loss curves of PBS nanocomposites

ability to enhance the thermal stability, the organic surfactant on the organoclay could suffer from decomposition following the Hoffmann elimination reaction [49–50]. The alkylammonium cations present on the OMMT surface is decomposed into an olefin and an amine, leaves an acid proton on the OMMT surface. This acid site is able to catalyze the degradation of the polymers at elevated temperatures, resulting in thermal instability of the material. On the other hand, the incorporation of PBS-g-MA into PBS does not show any significant change in the T_{d5}, but increased the T_{dmax}. The enhancement in the thermal properties may due to the improved interactions between PBS and PBS-g-MA [51]. For the compatibilized nanocomposites, the improved filler-matrix interaction in the nanocomposites does not favor the thermal stability. This means that the presence of alkylammonium groups on the OMMT surface has catalyzed the degradation, leads to a reduction in the thermal stability.

3.2.7. Fourier transform infrared (FTIR) spectroscopy

It was discussed earlier that the polar MA groups may interact with the amine groups on the OMMT surface by forming hydrogen bonding on one side, and with the carbonyl groups on the PBS chains on the other side. This is further verified from the FTIR spectroscopy as presented in Figure 11. The characteristic peaks of PBS-g-MA at 1780 and 1849 cm^{-1} disappeared in the compatibilized PBS nanocomposites. The peak intensities of PBS nanocomposites were weakened after compatibilization, typically for the ester function groups in PBS (1144–1264 cm^{-1} and 1710–1713 cm^{-1}). Furthermore, the transmittance band (721 cm^{-1}) corresponding to the amine functional groups of octadecylamine in OMMT vanished after compatibilization. Hence, it is quite reasonable to suppose that partial hydrolysis occurred in the anhydride functional groups interacting with the alkylammonium and the hydroxyl groups on OMMT surface, and with the carbonyl groups in PBS by forming hydrogen bonds [52].

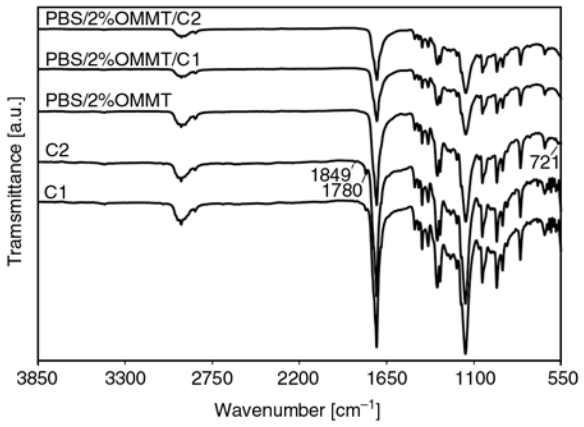

Figure 11. FTIR spectra of PBS-g-MA and nanocomposites before and after compatibilization

4. Conclusions

This study successfully demonstrated the synthesis of PBS-g-MA through reactive grafting process at the diol unit of PBS, as confirmed by FTIR and NMR spectroscopy. PBS-g-MA produced by using higher initiator content exhibited higher degree of grafting. Mechanical properties of PBS nanocomposites were improved after the incorporation of PBS-g-MA as compatibilizer. The compatibilizer not only enhanced the intercalation of polymer chains between the silicate galleries, but also improved the filler-matrix interaction. PBS-g-MA that prepared at higher initiator content was able to provide a better compatibilizing effect, caused by the higher degree of grafting. Besides that, PBS-g-MA could act as a nucleating agent to increase the degree of crystallinity, which is partially responsible for the improvements in mechanical properties. However, the effect of PBS-g-MA on the thermal stability of nanocomposites is negligible.

Acknowledgements

The financial support of USM Research University Cluster Grant (1001/PKT/8640012), USM Incentive Grant (1001/PBAHAN/8021011), USM Research University Postgraduate Research Grant Scheme (1001/PBAHAN/8044004), USM Fellowship and USM Post-doctoral Fellowship is gratefully acknowledged.

References

[1] LeBaron P. C., Wang Z., Pinnavaia T. J.: Polymer-layered silicate nanocomposites: An overview. Applied Clay Science, **15**, 11–29 (1999). DOI: 10.1016/S0169-1317(99)00017-4

[2] Alexandre M., Dubois P.: Polymer-layered silicate nanocomposites: Preparation, properties and uses of a new class of materials. Materials Science and Engineering R: Reports, **28**, 1–63 (2000). DOI: 10.1016/S0927-796X(00)00012-7

[3] Rajesh J. J., Soulestin J., Lacrampe M. F., Krawczak P.: Effect of injection molding parameters on nanofillers dispersion in masterbatch based PP-clay nanocomposites. Express Polymer Letters, **6**, 237–248 (2012).
DOI: 10.3144/expresspolymlett.2012.26

[4] Li Y., Zhao B., Xie S., Zhang S.: Synthesis and properties of poly(methyl methacrylate)/montmorillonite (PMMA/MMT) nanocomposites. Polymer International, **52**, 892–898 (2003).
DOI: 10.1002/pi.1121

[5] Zhao C., Qin H., Gong F., Feng M., Zhang S., Yang M.: Mechanical, thermal and flammability properties of polyethylene/clay nanocomposites. Polymer Degradation and Stability, **87**, 183–189 (2005).
DOI: 10.1016/j.polymdegradstab.2004.08.005

[6] Rousseaux D. D. J., Sallem-Idrissi N., Baudouin A-C., Devaux J., Godard P., Marchand-Brynaert J., Sclavons M.: Water-assisted extrusion of polypropylene/clay nanocomposites: A comprehensive study. Polymer, **52**, 443–451 (2011).
DOI: 10.1016/j.polymer.2010.11.027

[7] Yano K., Usuki A., Okada A., Kurauchi T., Kamigaito O.: Synthesis and properties of polyimide–clay hybrid. Journal of Polymer Science Part A: Polymer Chemistry, **31**, 2493–2498 (1993).
DOI: 10.1002/pola.1993.080311009

[8] Gilman J. W., Jackson C. L., Morgan A. B., Harris R., Manias E., Giannelis E. P., Wuthenow M., Hilton D., Phillips S. H.: Flammability properties of polymer–layered-silicate nanocomposites. Polypropylene and polystyrene nanocomposites. Chemistry of Materials, **12**, 1866–1873 (2000).
DOI: 10.1021/cm0001760

[9] Timochenco L., Grassi V. G., Dal Pizzol M., Costa J. M., Castellares L. G., Sayer C., Machado R. A. F., Araújo P. H. H.: Swelling of organoclays in styrene. Effect on flammability in polystyrene nanocomposites. Express Polymer Letters, **4**, 500–508 (2010).
DOI: 10.3144/expresspolymlett.2010.63

[10] Okamoto K., Ray S. S., Okamoto M.: New poly(butylene succinate)/layered silicate nanocomposites. II. Effect of organically modified layered silicates on structure, properties, melt rheology, and biodegradability. Journal of Polymer Science Part B: Polymer Physics, **41**, 3160–3172 (2003).
DOI: 10.1002/polb.10708

[11] Someya Y., Nakazato T., Teramoto N., Shibata M.: Thermal and mechanical properties of poly(butylene succinate) nanocomposites with various organo-modified montmorillonites. Journal of Applied Polymer Science, **91**, 1463–1475 (2003).
DOI: 10.1002/app.13366

[12] Chen G-X., Kim E-S., Yoon J-S.: Poly(butylene succinate)/twice functionalized organoclay nanocomposites: Preparation, characterization, and properties. Journal of Applied Polymer Science, **98**, 1727–1732 (2005).
DOI: 10.1002/app.22264

[13] Fujimaki T.: Processability and properties of aliphatic polyesters, 'BIONOLLE', synthesized by polycondensation reaction. Polymer Degradation and Stability, **59**, 209–214 (1998).
DOI: 10.1016/S0141-3910(97)00220-6

[14] Chieng B. W., Ibrahim N. A., Wan Yunus W. M. Z.: Effect of organo-modified montmorillonite on poly (butylene succinate)/poly(butylene adipate-co-terephthalate) nanocomposites. Express Polymer Letters, **4**, 404–414 (2010).
DOI: 10.3144/expresspolymlett.2010.51

[15] Phua Y. J., Chow W. S., Mohd Ishak Z. A.: Poly(butylene succinate)/ organo-montmorillonite nanocomposites: Effects of the organoclay content on mechanical, thermal, and moisture absorption properties. Journal of Thermoplastic Composite Materials, **24**, 133–151 (2010).
DOI: 10.1177/0892705710376469

[16] Phua Y. J., Chow W. S., Mohd Ishak Z. A.: Mechanical properties and structure development in poly(butylene succinate)/organo-montmorillonite nanocomposites under uniaxial cold rolling. Express Polymer Letters, **5**, 93–103 (2011).
DOI: 10.3144/expresspolymlett.2011.11

[17] Nwabunma D., Kyu T.: Polyolefin composites. Wiley-Interscience, New Jersey (2008).

[18] Pegoretti A., Dorigato A., Penati A.: Tensile mechanical response of polyethylene-clay nanocomposites. Express Polymer Letters, **1**, 123–131 (2007).
DOI: 10.3144/expresspolymlett.2007.21

[19] Petersson L., Oksman K., Mathew A. P: Using maleic anhydride grafted poly(lactic acid) as a compatibilizer in poly(lactic acid)/layered-silicate nanocomposites. Journal of Applied Polymer Science, **102**, 1852–1862 (2006).
DOI: 10.1002/app.24121

[20] Lai S-M., Li H-C., Liao Y-C.: Properties and preparation of compatibilized nylon 6 nanocomposites/ABS blends: Part II – Physical and thermal properties. European Polymer Journal, **43**, 1660–1671 (2007).
DOI: 10.1016/j.eurpolymj.2007.02.009

[21] Kusmono, Mohd Ishak Z. A., Chow W. S., Takeichi T., Rochmadi: Enhancement of properties of PA6/PP nanocomposites via organic modification and compatibilization. Express Polymer Letters, **2**, 655–664 (2008).
DOI: 10.3144/expresspolymlett.2008.78

[22] López-Quintanilla M. L., Sánchez-Valdés S., Ramos de Valle L. F., Medellín-Rodríguez F. J.: Effect of some compatibilizing agents on clay dispersion of polypropylene-clay nanocomposites. Journal of Applied Polymer Science, **100**, 4748–4756 (2006).
DOI: 10.1002/app.23262

[23] Kusmono, Mohd Ishak Z. A., Chow W. S., Takeichi T., Rochmadi: Compatibilizing effect of SEBS-g-MA on the mechanical properties of different types of OMMT filled polyamide 6/polypropylene nanocomposites. Composites Part A: Applied Science and Manufacturing, **39**, 1802–1814 (2008).
DOI: 10.1016/j.compositesa.2008.08.009

[24] Mohanty S., Nayak S. K.: Effect of clay exfoliation and organic modification on morphological, dynamic mechanical, and thermal behavior of melt-compounded polyamide-6 nanocomposites. Polymer Composites, **28**, 153–162 (2007).
DOI: 10.1002/pc.20284

[25] Qiu Z., Yang W.: Crystallization kinetics and morphology of poly(butylene succinate)/poly(vinyl phenol) blend. Polymer, **47**, 6429–6437 (2006).
DOI: 10.1016/j.polymer.2006.07.001

[26] Mani R., Bhattacharya M., Tang J.: Functionalization of polyesters with maleic anhydride by reactive extrusion. Journal of Polymer Science Part A: Polymer Chemistry, **37**, 1693–1702 (1999).
DOI: 10.1002/(SICI)1099-0518(19990601)37:11<1693::AID-POLA15>3.0.CO;2-Y

[27] Tserki V., Matzinos P., Panayiotou C.: Novel biodegradable composites based on treated lignocellulosic waste flour as filler. Part II. Development of biodegradable composites using treated and compatibilized waste flour. Composites Part A: Applied Science and Manufacturing, **37**, 1231–1238 (2006).
DOI: 10.1016/j.compositesa.2005.09.004

[28] Kim H-S., Lee B-H., Choi S-W., Kim S., Kim H-J.: The effect of types of maleic anhydride-grafted polypropylene (MAPP) on the interfacial adhesion properties of bio-flour-filled polypropylene composites. Composites Part A: Applied Science and Manufacturing, **38**, 1473–1482 (2007).
DOI: 10.1016/j.compositesa.2007.01.004

[29] Phua Y. J., Chow W. S., Mohd Ishak Z. A.: The hydrolytic effect of moisture and hygrothermal aging on poly(butylene succinate)/organo-montmorillonite nanocomposites. Polymer Degradation and Stability, **96**, 1194–1203 (2011).
DOI: 10.1016/j.polymdegradstab.2011.04.017

[30] Sclavons M., Laurent M., Devaux J., Carlier V.: Maleic anhydride-grafted polypropylene: FTIR study of a model polymer grafted by ene-reaction. Polymer, **46**, 8062–8067 (2005).
DOI: 10.1016/j.polymer.2005.06.115

[31] Chow W. S., Mohd Ishak Z. A., Karger-Kocsis J., Apostolov A. A., Ishiaku U. S.: Compatibilizing effect of maleated polypropylene on the mechanical properties and morphology of injection molded polyamide 6/polypropylene/organoclay nanocomposites. Polymer, **44**, 7427–7440 (2003).
DOI: 10.1016/j.polymer.2003.09.006

[32] Mishra J. K., Hwang K-J., Ha C-S.: Preparation, mechanical and rheological properties of a thermoplastic polyolefin (TPO)/organoclay nanocomposite with reference to the effect of maleic anhydride modified polypropylene as a compatibilizer. Polymer, **46**, 1995–2002 (2005).
DOI: 10.1016/j.polymer.2004.12.044

[33] Shen Z., Simon G. P., Cheng Y-B.: Comparison of solution intercalation and melt intercalation of polymer–clay nanocomposites. Polymer, **43**, 4251–4260 (2002).
DOI: 10.1016/S0032-3861(02)00230-6

[34] Parija S., Nayak S. K., Verma S. K., Tripathy S. S.: Studies on physico-mechanical properties and thermal characteristics of polypropylene/layered silicate nanocomposites. Polymer Composites, **25**, 646–652 (2004).
DOI: 10.1002/pc.20059

[35] Samal S. K., Nayak S. K., Mohanty S.: Polypropylene nanocomposites: Effect of organo-modified layered silicates on mechanical, thermal & morphological performance. Journal of Thermoplastic Composite Materials, **21**, 243–263 (2008).
DOI: 10.1177/0892705708089476

[36] Ray S. S., Bousmina M., Okamoto K.: Structure and properties of nanocomposites based on poly(butylene succinate-*co*-adipate) and organically modified montmorillonite. Macromolecular Materials and Engineering, **290**, 759–768 (2005).
DOI: 10.1002/mame.200500203

[37] Vega-Baudrit J., Sibaja M., Martín-Martínez J. M., Nakayama K., Masuda T., Cao A.: Characterization of the biodegradable polymer bionolle. in 'New developments in polymer analysis, stabilization and degradation' (ed.: Zaikov G. E. Jiménez A.) Nova Science, New York, 57–71 (2005).

[38] Pang M. Z., Qiao J. J., Jiao J., Wang S. J., Xiao M., Meng Y. Z.: Miscibility and properties of completely biodegradable blends of poly(propylene carbonate) and poly(butylene succinate). Journal of Applied Polymer Science, **107**, 2854–2860 (2008).
DOI: 10.1002/app.27252

[39] Chiu F-C., Lai S-M., Chen Y-L., Lee T-H.: Investigation on the polyamide 6/organoclay nanocomposites with or without a maleated polyolefin elastomer as a toughener. Polymer, **46**, 11600–11609 (2005).
DOI: 10.1016/j.polymer.2005.09.077

[40] Minhaz-Ul Haque M., Alvarez V., Paci M., Pracella M.: Processing, compatibilization and properties of ternary composites of Mater-Bi with polyolefins and hemp fibres. Composites Part A: Applied Science and Manufacturing, **42**, 2060–2069 (2011).
DOI: 10.1016/j.compositesa.2011.09.015

[41] Xu W., Liang G., Wang W., Tang S., He P., Pan W-P.: Poly(propylene)–poly(propylene)-grafted maleic anhydride–organic montmorillonite (PP–PP-g-MAH–Org-MMT) nanocomposites. II. Nonisothermal crystallization kinetics. Journal of Applied Polymer Science, **88**, 3093–3099 (2003).
DOI: 10.1002/app.11974

[42] Ding C., Jia D., He H., Guo B., Hong H.: How organo-montmorillonite truly affects the structure and properties of polypropylene. Polymer Testing, **24**, 94–100 (2005).
DOI: 10.1016/j.polymertesting.2004.06.005

[43] Kusmono, Mohd Ishak Z. A., Chow W. S., Takeichi T., Rochmadi: Influence of SEBS-g-MA on morphology, mechanical, and thermal properties of PA6/PP/organoclay nanocomposites. European Polymer Journal, **44**, 1023–1039 (2008).
DOI: 10.1016/j.eurpolymj.2008.01.019

[44] Cui W., Jiao Q., Zhao Y., Li H., Liu H., Zhou M.: Preparation of poly(ethylene terephthalate)/layered double hydroxide nanocomposites by *in-situ* polymerization and their thermal property. Express Polymer Letters, **6**, 485–493 (2012).
DOI: 10.3144/expresspolymlett.2012.51

[45] Lee D. C., Jang L. W.: Preparation and characterization of PMMA–clay hybrid composite by emulsion polymerization. Journal of Applied Polymer Science, **61**, 1117–1122 (1996).
DOI: 10.1002/(SICI)1097-4628(19960815)61:7<1117::AID-APP7>3.0.CO;2-P

[46] Liang Z-M., Yin J., Wu J-H., Qiu Z-X., He F-F.: Polyimide/montmorillonite nanocomposites with photolithographic properties. European Polymer Journal, **40**, 307–314 (2004).
DOI: 10.1016/j.eurpolymj.2003.09.020

[47] Zhu J., Wilkie C. A.: Thermal and fire studies on polystyrene–clay nanocomposites. Polymer International, **49**, 1158–1163 (2000).
DOI: 10.1002/1097-0126(200010)49:10<1158::AID-PI505>3.0.CO;2-G

[48] Song L., Hu Y., Tang Y., Zhang R., Chen Z., Fan W.: Study on the properties of flame retardant polyurethane/organoclay nanocomposite. Polymer Degradation and Stability, **87**, 111–116 (2005).
DOI: 10.1016/j.polymdegradstab.2004.07.012

[49] Cai Y., Wu N., Wei Q., Zhang K., Xu Q., Gao W., Song L., Hu Y.: Structure, surface morphology, thermal and flammability characterizations of polyamide 6/organic-modified Fe-montmorillonite nanocomposite fibers functionalized by sputter coating of silicon. Surface and Coatings Technology, **203**, 264–270 (2008).
DOI: 10.1016/j.surfcoat.2008.08.076

[50] Cui L., Khramov D. M., Bielawski C. W., Hunter D. L., Yoon P. J., Paul D. R.: Effect of organoclay purity and degradation on nanocomposite performance, Part 1: Surfactant degradation. Polymer, **49**, 3751–3761 (2008).
DOI: 10.1016/j.polymer.2008.06.029

[51] Zhai H., Xu W., Guo H., Zhou Z., Shen S., Song Q.: Preparation and characterization of PE and PE-g-MAH/montmorillonite nanocomposites. European Polymer Journal, **40**, 2539–2545 (2004).
DOI: 10.1016/j.eurpolymj.2004.07.009

[52] Lonkar S. P., Therias S., Leroux F., Gardette J. L., Singh R. P.: Influence of reactive compatibilization on the structure and properties of PP/LDH nanocomposites. Polymer International, **60**, 1688–1696 (2011).
DOI: 10.1002/pi.3129

eXPRESS Polymer Letters Vol.7, No.4 (2013) 355–364
Available online at www.expresspolymlett.com
DOI: 10.3144/expresspolymlett.2013.32

A multi-layer bioinspired design with evolution of shish-kebab structures induced by controlled periodical shear field

K. J. Liu, J. Zhang, H. Liu, X. Y. Qian, Y. Zhang, T. Wang, K. Z. Shen*

State Key Laboratory of Polymer Materials Engineering, College of Polymer Science and Engineering, Sichuan University, Chengdu, PR China

Received 13 September 2012; accepted in revised form 9 December 2012

Abstract. The crystallization of polymers, caused by flow fields in the melt, has been the subject of extensive studies for many years. In this study, we use periodical shear to induce polypropylene to form multi-layer structure, which is usually observed in plants. Two interesting points were found: firstly, the quest of mimicking natural structures was achieved by controlled periodical shear field; secondly, the evolution from nano to shish-kebab-like cylindrite structure was obtained in the multi-layer structure, which can be clarified by nuclei competition model. This study can be used to better understand the shear-induced crystallization of polymer. Here our intention is to place this new observation on the map, leaving a fuller presentation and discussion of the work to a future publication.

Keywords: *processing technologies, bioinspired, shish-kebab, multi-layer, shear-induced crystallization*

1. Introduction

The creativity of nature is very amazing and interesting. Creatures always have the simplest but most optimized structures, e.g., reed, shell, bone and so on, which display excellent comprehensive mechanical performance, prominent adaptability and good self-healing feature. Bionics is developing rapidly as a new branch of material science, chemistry, physics and biology [1].

Reed is a large perennial grass found in wetlands throughout temperate and tropical regions of the world. The stem of reed is lightweight, high-performance structural material with exceptional strength and toughness. These two properties tend to be mutually exclusive, and attaining optimal mechanical performance is invariably a compromise often achieved through the empirical design of microstructures. Its highly sophisticated structures with complex hierarchical morphology are shown in Figure 1. Figure 1a shows that the cross section of reed stem is formed by vessels which carry nutrients and water between leaves and root. Figure 1b shows that the vertical section of the reed stem which is consisted of a multi-layer structure. Figure 1c indicates that these layers are formed by vessel cells, which look like highly oriented fibers [2]. These multi-layer cylindrical structures are so-called walled cylindrical shell structures [3]. Slippage between layers can absorb energy to avoid the stem breaking. The deformation of thin walled cylindrical shell structure can be restricted to deformation [4]. Can polymer products be bioinspired designed to improve their mechanical properties? The quest of mimicking natural structures in the synthesis of new structural materials has generated enormous interest but has yielded few practical advances.

*Corresponding author, e-mail: zhangjie@scu.edu.cn

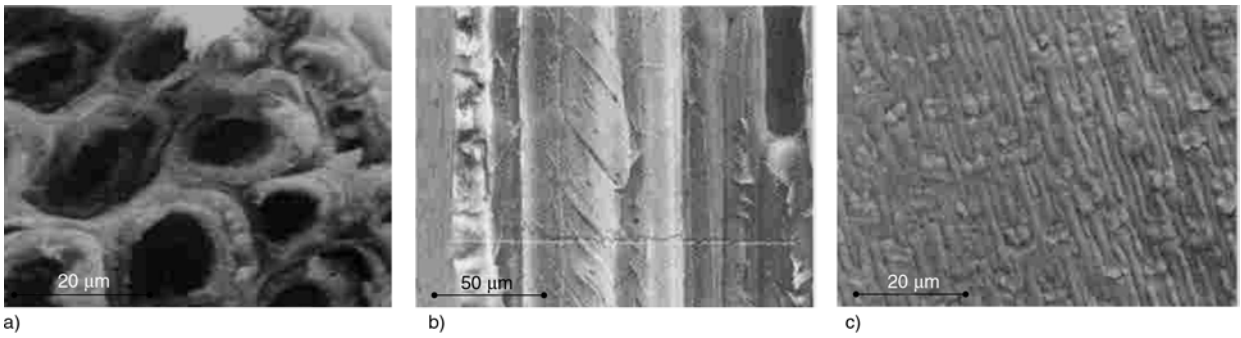

Figure 1. SEM figures of reeds stem and its multi-layer structure, (a) cross section of layer from reeds stem, (b) vertical section of reeds stem, (c) surface of layer from reeds stem. (ref. [2], permitted by the Publishers)

It is well known that iPP parts prepared by injection molding always present an evolution from skin to core morphology [5, 6]. The skin [7] starts forming during the filling phase due to the rapid cooling of the hot and highly oriented melt against the cold mold wall. Transition region [8] is formed by deformed spherulites. Shear region has peculiar microstructures induced by shear flow, normally referred to as shish-kebab structures [9]. The core [10, 11] shows essentially α-type spherulitic morphology. The evolution is due to the gradient of thermal and flow field. Bevis and coworkers [12, 13] invented shear controlled orientation injection molding (SCORIM) to provide strengthening shear field. Su *et al.* [14] used SCORIM to produce the so-call bioinspired bamboo-like structure with a typical hierarchic structure with high-proportion shish-kebab structures in the skin and intermediate layers and abundant beta-crystals in the core layer. Another successful experiment was conducted by Zhong and coworkers [15, 16], who obtained injection molded polymer parts with a high and homogeneous orientation distribution upon a combination of *in situ* microfibrils and dynamic oscillation shear by suppressing the skin-core structure of iPP parts. Our previous work [17] also changes the morphology of injection parts by periodical vibration injection molding (PVIM).

These methods [12–17] are to strengthen shear field to induce the transition from a relatively isotropic, spherulitic morphology [18–20] to a highly oriented, shish-kebab morphology [21]. Formation of shish-kebab structure [22] can be described as follows: When polymer melts are sheared, molecules can be oriented in the flow direction. Alignment of chain segments of polymer molecules is a natural consequence of shear. At given temperature and external shear field, the degree of orientation and the extent of alignment obviously depend on the critical entanglement molecular weight, relaxation time, helical chain conformation, etc. Hence, it is possible that, under certain experimental conditions, only partial chain strands are oriented in the flow direction, while the other chain strands, especially those near the chain ends, remain unoriented or randomly oriented with respect to the flow direction. When bundles of oriented chain segments develop under shear, these bundles can initiate the formation of primary nuclei. Then, crystallization continues to produce the so-called 'shish-kebab' (cylindrite) morphology [23]. Zhang *et al.* [24] found the shish-kebab structures which formed at low shear rate and low temperature were different from the classical shish-kebab structures which formed at high shear rate and temperature. The greatest difference was that low temperature and shear rate can induce shish-kebab-like cylindrite structures which can be observed by polarized light microscope (PLM), while the high temperature and shear rate induced nano-scale shish-kebab structures [25], which were usually characterized by scanning electron microscope (SEM) and small angle X-ray diffraction (SAXD). In our previous work [26], a region full of shish-kebab (cylindrite) structures induced by PVIM, which belong to shish-kebab-like structures reported by Han and coworkers [23, 24], was also found between skin and core. These shish-kebab structures were in close resemblance to the polymorphic shish-kebab morphology in iPP melts sheared with fibers [27–29], crystallization in fibers/polymer composites [30, 31], or sample crystallization by a razor blade shear in the melt [32]. However, in our experiment there were neither fibers nor other nucleation species added.

Herein, the PVIM technique was exploited in the creation of reed-stem-like multi-layer bionic sam-

ples. The goal was to realize the bioinspired design to significantly improve the mechanical properties of iPP samples. It was very interesting that we found the multi-layer structure composed of evolution from nano to shish-kebab-like cylindrite structure induced by periodical shear. To the best of our knowledge, this is the first report of shish-kebab structures of different scales in the same sample.

2. Experimental section

2.1. Material

IPP (grade: F401) used in the experiment was a commercial product from Lan Gang petroleum chemical, China, and its MFI is 2.3 g/10 min. The molecular weight of the iPP is 80~120 thousands.

2.2. Sample preparation

In the PVIM, there is a vibration system in addition to injection system. The injection system provides the basic pressure while the vibration system provides oscillatory pressure. During the packing stage, a periodically changing pressure acts on the melt in the runner and mold cavity until the injection gate is frozen. A schematic representation of the melt vibration injection apparatus was shown in Figure 2. The processing parameters were shown in Table 1, which were set on the control panel. For the purpose of comparison, conventional injection molding (CIM) was carried out under static packing (without vibration) by using the same processing parameters.

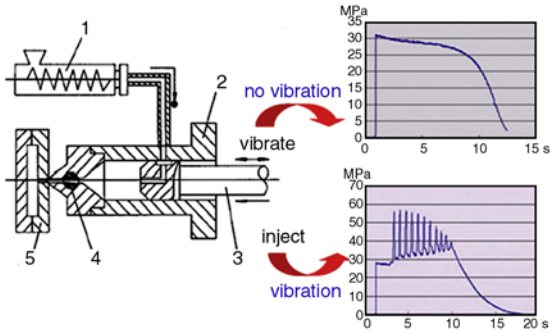

Figure 2. The schematic representation of pressure vibration injection molding and the cavity pressure profile measured from a pressure sensor. 1 – plasticizing equipment, 2 – barel, 2 – vibrating and injecting piston, 4 ; valves, 5 – injection mold

Table 1. Processing parameters

	Static injection molding	Vibration injection molding
Injection pressure [MPa]	35	35
Packing pressure [MPa]	35	35
Melt temperature [°C]	200	200
Mold temperature [°C]	40	40
Vibration pressure [MPa]	0	60
Frequency [Hz]	0	0.9

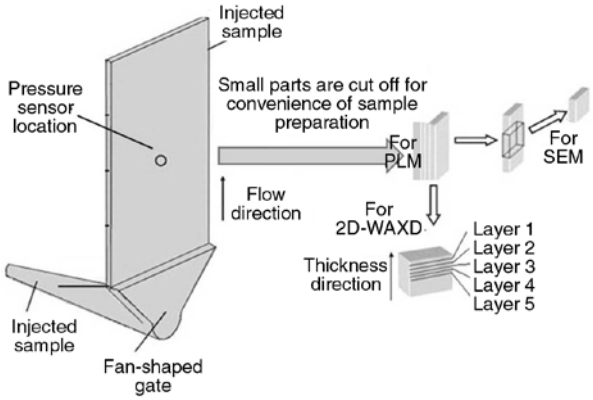

Figure 3. Specimen preparation for tests

The samples have rectangular geometry with a dimension of 50 mm × 80 mm × 2 mm. The molding gate is fan-shape with an end dimension of 50 mm × 5 mm. The thickness of gate is larger than that of cavity, so as to achieve relatively homogeneous flow. The pressure sensor was located in the central part of sample cavity. To better investigate and analyze the morphology evolution, the sample was divided into four zones along the flow direction. Besides, one half-width of each specimen was separated into five layers through the thickness direction for 2D-WAXD study, as also shown in Figue 3. Each layer is 0.2 mm thick. The preparation of specimen for tests is exhibited in Figure 3. The specimens for PLM observation were cut into slices with a thickness of 10 microns by means of microtome at room temperature. The microtome is MT-1 from Zhe-Jiang Yidi Medical Apparatus and Instruments Co. Ltd., China.

2.3. Character methods

2.3.1. Polarized-light microscopy (PLM)

The specimens for PLM are15 μm thick slices prepared by microtome along MD and ND axis respectively, as shown in Figure 3. Subsequently, micrographs were taken using a DX-1 (Jiang Xi Phoenix Optical Co. China.) microscope connected with a Nikon 500D digital camera.

2.3.2. Scanning electron microscope (SEM)

For the SEM observation, the blocky specimen was ground and polished to the same distance from the sample surface as the slices prepared for PLM, then

etched for a certain time in an etchant consisting of a 3% w/v solution of potassium permanganate dissolved in the sulphuric and dry ortho-phosphoric acids mixed solution, and then washed with 30% hydrogen peroxide and distilled water. The specimen was gold sputtered before observation.

2.3.3. Synchrotron two-dimensional wide-angle X-ray diffraction (2D-WAXD).

Specimens for 2D-WAXD were 1mm thick slices cut from the injection sample, as shown in Figure 3. The synchrotron 2D-WAXD experiments were carried out on the U7B beam line in the National Synchrotron Radiation Laboratory (NSRL), Hefei, China. The wavelength used was 0.1409 nm. The two-dimensional diffraction patterns were recorded every 180 s by a Mar CCD 165 X-ray detector system in transmission mode at room temperature. Azimuthally scans (0–360°) of 2D-WAXD were made for the corresponding lattice planes of the α-form polypropylene (α-PP). The orientation level of various planes could be calculated by the orientation parameter f, which was calculated as shown by Equtions (1) and (2):

$$f = \frac{3\overline{(\cos^2\phi)} - 1}{2} \tag{1}$$

$$\overline{(\cos^2\phi)} = \frac{\int_0^{\pi/2} I(\phi)\sin\phi\cos^2\phi \mathrm{d}\phi}{\int_0^{\pi/2} I(\phi)\sin\phi \mathrm{d}\phi} \tag{2}$$

where ϕ is the angle between the normal of a given crystal plane and the shear flow direction and I is intensity. Additionally, the relative crystallinity of β (K_β) is calculated by Equation (3):

$$K_\beta = \frac{I_\beta}{I_{\alpha1} + I_{\alpha2} + I_{\alpha3} + I_\beta} \tag{3}$$

where I_β is the intensity of the (300) reflection of the β-modification, and $I_{\alpha1}$, $I_{\alpha2}$, and $I_{\alpha3}$ are the intensities for the (110), (040), and (130) planes of the α-phase, respectively.

2.3.4. Dynamic mechanical properties

Dynamic mechanical analysis (DMA) was performed using a TA DMA Q800 analyzer from TA Instruments (USA). A three point bending clamping geometry was used. DMA tests were carried out from –100 to 150°C at a heating rate of 5°C/min at 1 Hz.

2.3.5. Tensile testing

Tensile testing was performed according to GBT1040-2006 (National Standards of P.R.C) on an A REGER-1030 testing machine (RTG-10) at room temperature. The tensile rate is 5 0mm/min.

3. Results and discussion

3.1. Hierarchical structures of CIM samples and PVIM samples by PLM

Longitudinal sections of PVIM and CIM samples were examined using PLM. Herein, because the sample has a symmetrical structure, only half of which is shown. In Figure 4a, CIM sample can be roughly divided into skin, shear region and core region. However, because the skin and the shear region are too thin to be distinguished, they are marked together in Figure 4. That of PVIM samples

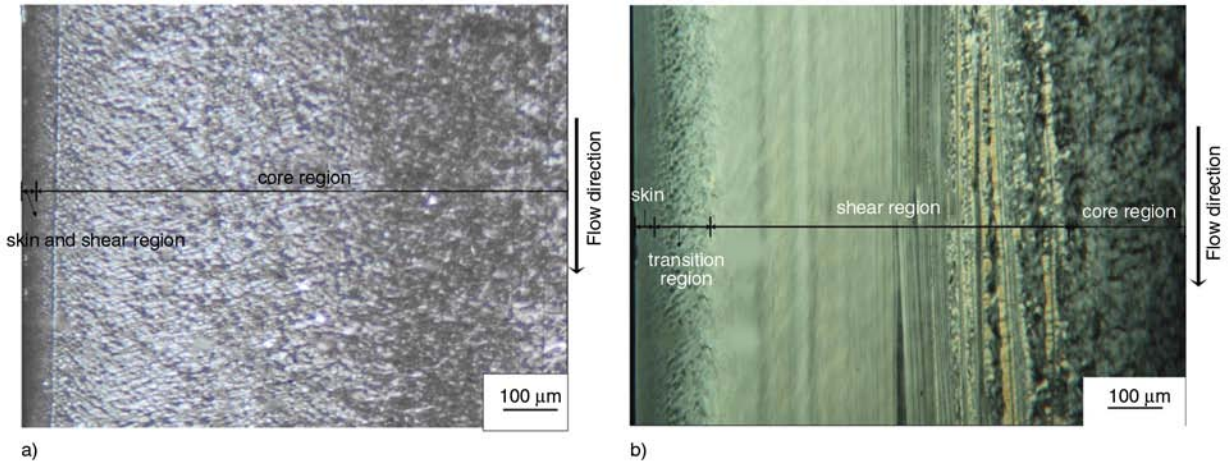

Figure 4. PLM figures of (a) CIM sample and (b) PVIM sample

are more abundant, which can be divided into skin, transition region, shear region and core region. Skin may formed by oriented structures, which cannot be clearly observed by the PLM, as reported by other researchers [16, 17]. Transition region is formed by transformed spherulites. Shear region consists of shear-induced crystal structures. Core region is composed of more perfect spherulites. What is notable is that obvious multi-layer structure exists in shear region, which is similar to multi-layer structure shown in Figure 1b.

In the CIM sample, the core region is the thickest, which is 972 μm. While, the thickness of the core region of PVIM sample is only 206 μm. Instead, shear region becomes the thickest in PVIM sample.

3.2. Microstructure of multi-layer morphology by PLM and SEM

As mentioned above, the most obvious difference between CIM sample and PVIM sample is a multi-layer structure existing in the shear region of the PVIM sample as shown in Figure 5. It indicates that a so-called multi-layer morphology is formed by two obviously different layers. In the layer close to skin, there are overcrowding fiber-like [33] structures that have unclear boundaries. With the distance increasing from the skin, these fiber-like structures can be distinguished more easily. In vicinity of core, unambiguous multi-layer structure is formed by so-called shish-kebab structures.

To clarify the morphology of the two layers, their scanning electron microscopy (SEM) micrographs are presented in Figures 6 and 7. As shown in Figure 6, the layer close to skin is also mainly constituted of shish-kebab structures. However the size of these shish-kebab structures is only a few nanometers. Therefore, the layer can be named as nano-scale shish-kebab layer.

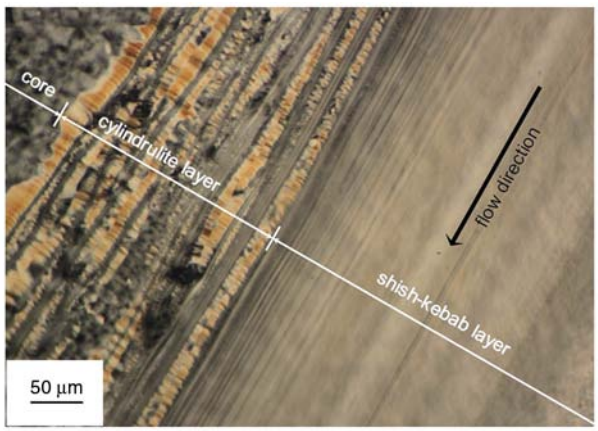

Figure 5. PLM graph of multi-layer structure of PVIM sample

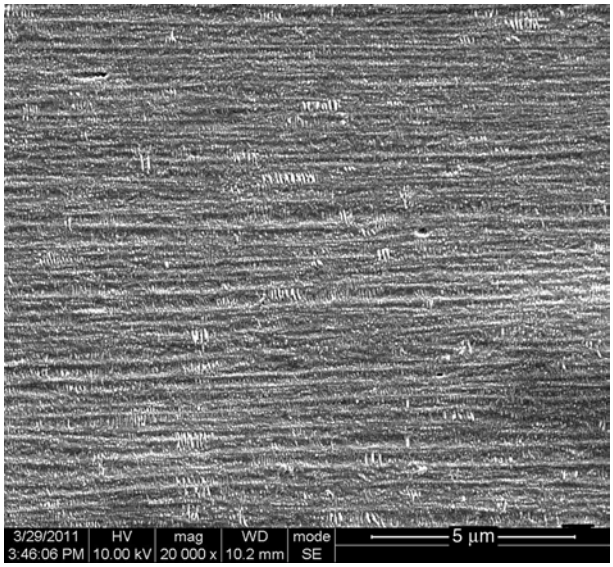

Figure 6. SEM figure of shish-kebab layer

The other layer contains much larger shish-kebab structures, which can be observed by PLM, is also shown by SEM in Figure 7. The layer can be named as shish-kebab-like cylindrite layer. However, the shish shown in Figure 5 is not observed, which was etched. According to the SEM figures, the shish-kebab-like cylindrite structure is schematically drawn in Figure 8: in the center of the core a single fiber-like shish exists, which is induced by shear; Around the shish, the α-to-β growth transition or α β-bifurcation took place during crystal growth, which led to the formation of randomly dispersed β-nuclei; as long as the kinetic requirement for a

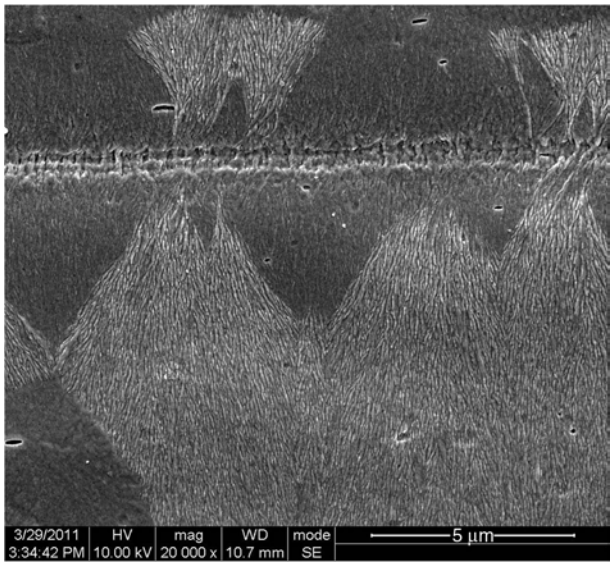

Figure 7. SEM figure of shish-kebab-like cylindrite structures

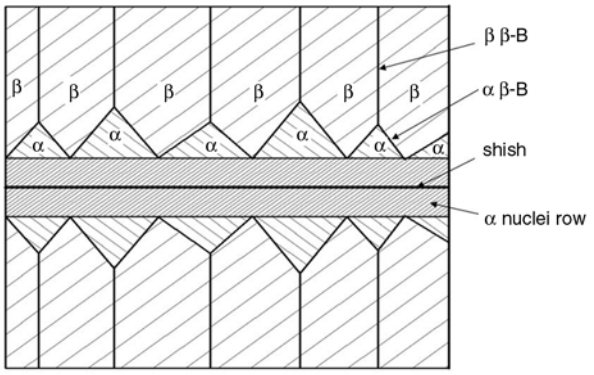

Figure 8. Schematic diagram of the cylindrite structure

higher growth rate of the β-phase (G_β) than α-phase (G_α) was achieved, these β-nuclei can induce epitaxial growth of β-phase along the α-core [34].

The shish-kebab-like cylindrite structure with mixed α- and β-modification is very fascinating. The structure is expected to be able to greatly improve the mechanical performance of iPP sample. It is similar to reed-stem vessel: these kebabs are formed by β-crystal; the core is formed by rigid α-crystals. During yielding process, acting as thin walled cylindrical shell structure in reed stem, the ductile β-crystal can deform more easily than the α-crystal. And transformation from β-form to α-form crystal can also absorb energy in impacting process [35].

3.3. Orientation and crystallinity of samples by 2D-WAXD

Figure 9 shows 2D WAXD patterns of CIM sample and PVIM sample at different distances from the skin. Except 1000 μm diffraction pattern, which characterizes the structure of core, the other diffraction patterns of the PVIM sample exhibit more pronounced arcing compared with those of the CIM samples. It indicates a pronounced orientation of iPP chains within lamellae in PVIM sample.

The (040) reflection, which can be detected in all layers, is chosen to quantitatively evaluate the orientation level of CIM and PVIM samples. The orientation parameters estimated are plotted in Figure 10.

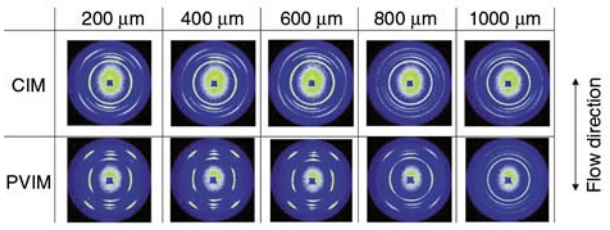

Figure 9. X-ray diffraction patterns of CIM and PVIM samples

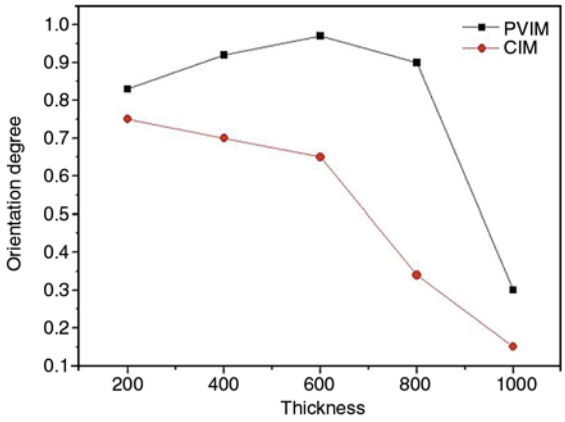

Figure 10. The evolution of orientation parameter

Orientation degree of CIM sample gradually decreases from skin (0.75) to core (0.15). However, orientation distribution of PVIM sample is obviously different: from 200 to 600 μm in thickness direction, the orientation degree increases gradually to the highest value of 0.95. At 800 μm, it is still as high as 0.9. In the core (1000 μm), it decreases to 0.3. It indicates that overall orientation of PVIM sample is higher and more narrowly distributed than CIM sample. Combined with PLM observation, an obvious conclusion can be drawn that the heterogeneity of shin-core structure of the CIM samples is suppressed to some degree in PVIM sample. In PVIM process, the formation of multi-layer morphology is a stepwise procedure. That is to say, after the solidification of one layer, on the surface of which the rest of melt is forced to flow in next oscillation period.

From these 2D-WAXD patterns in Figure 9, the β crystal content is calculated, which is induced by shear flow. The evolution of β relative crystal con-

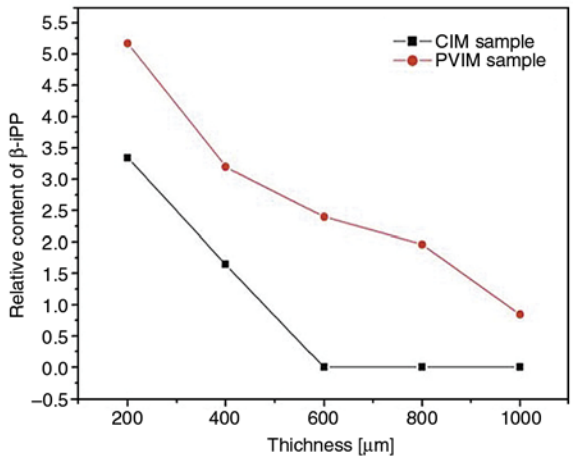

Figure 11. The evolution of β relative crystal content

tent is shown in Figure 11. The β content in PVIM sample is much more than that of CIM sample. Generally, β crystals are formed in appropriate fields, such as quenching the melt to a certain temperature range [36], directional crystallization in a thermal gradient field [37], shearing or elongation of the melt during crystallization [38], or using β-nucleating agents [39]. It should be noted that the β crystal is also found in 800 and 1000 μm layers due to optimization of shear flow by PVIM. Obviously, it is attributed to more appropriate shear and thermal field provided by PVIM than CIM.

3.4. Formation mechanism of reed-stem-like bionic multi-layer structure

The formation mechanism of multi-layer morphology is schematically shown in Figure 12. Before injection, iPP resin melt is in homogeneous state. Molecular chains present random coil state, as show in Figure 12(a). Under shear, molecular chain network is oriented in flow direction. This phenomenon is so-called coil-to-stretched chain transition, as show in Figure 12(b). Then, Figure 12(c) presents formation of shish from stretched chain network. These shishes act as crystal nuclei. Polymer melt crystallization is typically controlled by nucleation [40]. Lamellae epitaxially grow along shish leading to formation of plentiful shish-kebab structures, as shown in Figure 12(d), 12(e). Finally, the multi-layer morphology forms, as shown in Figure 12(f).

In this scenario, it's worth noting that, both nano and Shish-kebab-like cylindrite structures are formed from oriented shear-induced nucleating sites. Why the difference of dimension is so great? It is obvious that there exist three different kinds of nuclei, which can induce spherulites, shish-kebab-like and nano-scale shish-kebab, respectively. The competition between different crystal nuclei may be the reason for the difference. It is a competition for absorbing free crystalline lamellae. In shear field, the spherulite growth is suppressed. Herein, we pay attention to the shear-induced structures. Although both shish-kebab-like and nano-scale shish-kebab are shear-induced, their morphology is quite different. The difference is due to the distinction of density of the two layers. As shown in Figure 10, increased degree of orientation of shish-kebab layer indicates that more molecules of the layer are oriented.

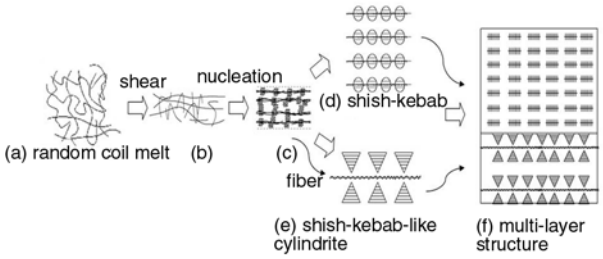

Figure 12. Schematic illustration of mechanism of the formation of multi-layer morphology

As Hsiao *et al*. [25] proposed that kebab growth rate is diffusion-controlled. Therefore, too high density of oriented structures can hinder the molecule chains to be absorbed onto shish. Therefore, the cylindrite structures, which need about 10~20 μm space to absorb the kebab, cannot be induced in shish-kebab layer, where too little space is left to absorb enough molecules.

According to the observed morphological features, it may be taken for granted that there exists a processing parameter window, which can balance the competition of different kinds of nuclei, enables the formation of reed-stem-like multi-layer structures.

3.5. Mechanical properties

The tensile strength of CIM sample is 31.9 MPa. Tensile strength of PVIM sample reaches 46.7 MPa; comparing to CIM sample, it increase by 46.4%. At low temperature (from –100 to –10°C), as shown in Figure 13, storage modulus of PVIM sample increases by about 25%; the loss modulus of PVIM increases by 100 MPa at low temperature. These data indicate that mechanical properties of the bioinspired sample can be improved greatly, especially high toughness of iPP parts is obtained at low temperature.

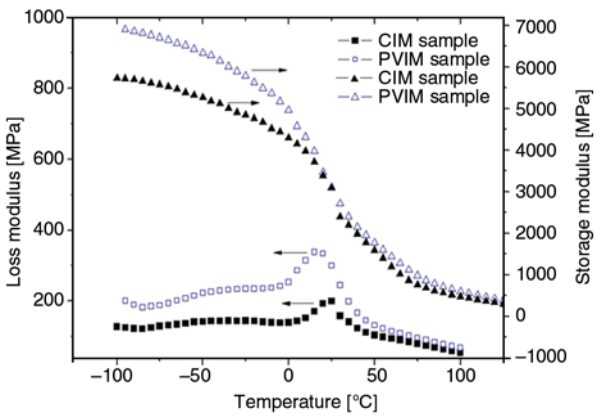

Figure 13. Mechanical properties of CIM and PVIM samples, the storage modulus and the loss modulus evolution by DMA

4. Conclusions

In this study, bioinspired samples with reed-stem-like multi-layer structure were developed under periodical shear via pressure vibration injection molding (PVIM). Sample with this structure has better mechanical properties than that of CIM sample. New viewpoint is put forward about transformation from traditional skin-core structure to highly oriented and multi-layer morphology. Toughening and strengthening of iPP samples are achieved. This evolution from nano to shish-kebab-like shish kebab structures is embodied in the multi-layer structure due to gradient of shear and thermal fields. The method is feasible in industry. The result leads to new insights into the structure and formation of polymer shish-kebabs under shear flow.

Acknowledgements

We would like to express our great thanks to National Natural Science Foundation of China (50873072) and the Special Funds for State Key Laboratory for financial support. We are indebted to the National Synchrotron Radiation Laboratory (NSRL) in University of Science and Technology of China and Prof. Guoqiang Pan (NSRL) for his help in synchrotron WAXD experiment.

References

[1] Bonderer L. J., Studart A. R., Gauckler L. J.: Bioinspired design and assembly of platelet reinforced polymer films. Science, **319**, 1069–1073 (2008). DOI: 10.1126/science.1148726

[2] Yugui Q., Liansheng C.: SEM-EDAX study on reed stem (in Chinese). Transactions of China Pulp and Paper, **20**, 5–7 (2005).

[3] Kim S-E., Kim C-S.: Buckling strength of the cylindrical shell and tank subjected to axially compressive loads. Thin-Walled Structures, **40**, 329–353 (2002). DOI: 10.1016/s0263-8231(01)00066-0

[4] Han L., Chrysanthou A., Young K. W.: Mechanical behaviour of self-piercing riveted multi-layer joints under different specimen configurations. Materials and Design, **28**, 2024–2033 (2007). DOI: 10.1016/j.matdes.2006.06.015

[5] Walker M., Smith R.: A procedure to select the best material combinations and optimally design composite sandwich cylindrical shells for minimum mass. Materials and Design, **27**, 160–165 (2006). DOI: 10.1016/j.matdes.2004.10.003

[6] Rajesh J. J., Soulestin J., Lacrampe M. F., Krawczak P.: Effect of injection molding parameters on nanofillers dispersion in masterbatch based PP-clay nanocomposites. Express Polymer Letters, **6**, 237–248 (2012). DOI: 10.3144/expresspolymlett.2012.26

[7] Viana J. C.: Structural interpretation of the strain-rate, temperature and morphology dependence of the yield stress of injection molded semicrystalline polymers. Polymer, **46**, 11773–11785 (2005). DOI: 10.1016/j.polymer.2005.10.024

[8] Geng Y., Wang G., Cong Y., Bai L., Li L., Yang C.: Shear-induced nucleation and growth of long helices in supercooled isotactic polypropylene. Macromolecules, **42**, 4751–4757 (2009). DOI: 10.1021/ma9004567

[9] Ogino Y., Fukushima H., Takahashi N., Matsuba G., Nishida K., Kanaya T.: Crystallization of isotactic polypropylene under shear flow observed in a wide spatial scale. Macromolecules, **39**, 7617–7625 (2006). DOI: 10.1021/ma061254t

[10] Somani R. H., Yang L., Hsiao B. S., Agarwal P. K., Fruitwala H. A., Tsou A. H.: Shear-induced precursor structures in isotactic polypropylene melt by *in-situ* rheo-SAXS and rheo-WAXD studies. Macromolecules, **35**, 9096–9104 (2002). DOI: 10.1021/ma020785o

[11] Somani R. H., Yang L., Hsiao B. S., Sun T., Pogodina N. V., Lustiger A.: Shear-induced molecular orientation and crystallization in isotactic polypropylene: Effects of the deformation rate and strain. Macromolecules, **38**, 1244–1255 (2005). DOI: 10.1021/ma048285d

[12] Mano J. F., Sousa R. A., Reis R. L., Cunha A. M., Bevis M. J.: Viscoelastic behaviour and time–temperature correspondence of HDPE with varying levels of process-induced orientation. Polymer, **42**, 6187–6198 (2001). DOI: 10.1016/s0032-3861(01)00090-8

[13] Kalay G., Allan P., Bevis M. J.: γ phase in injection moulded isotactic polypropylene. Polymer, **35**, 2480–2482 (1994). DOI: 10.1016/0032-3861(94)90366-2

[14] Su R., Zhang Z., Gao X., Ge Y., Wang K., Fu Q.: Polypropylene injection molded part with novel macroscopic bamboo-like bionic structure. The Journal of Physical Chemistry B, **114**, 9994–10001 (2010). DOI: 10.1021/jp1020802

[15] Zhong G-J., Li L., Mendes E., Byelov D., Fu Q., Li Z-M.: Suppression of skin–core structure in injection-molded polymer parts by *in situ* incorporation of a microfibrillar network. Macromolecules, **39**, 6771–6775 (2006). DOI: 10.1021/ma0604845

[16] Chen Y-H., Zhong G-J., Wang Y., Li Z-M., Li L.: Unusual tuning of mechanical properties of isotactic polypropylene using counteraction of shear flow and β-nucleating agent on β-form nucleation. Macromolecules, **42**, 4343–4348 (2009). DOI: 10.1021/ma900411f

[17] Zhang J., Shen K., Na S., Fu Q.: Vibration-induced change of crystal structure in isotactic polypropylene and its improved mechanical properties. Journal of Polymer Science Part B: Polymer Physics, **42**, 2385–2390 (2004).
DOI: 10.1002/polb.20110

[18] Kalay G., Zhong Z., Allan P., Bevis M. J.: The occurrence of the γ-phase in injection moulded polypropylene in relation to the processing conditions. Polymer, **37**, 2077–2085 (1996).
DOI: 10.1016/0032-3861(96)85852-6

[19] Stern C., Frick A. R., Weickert G., Michler G. H., Henning S.: Processing, morphology, and mechanical properties of liquid pool polypropylene with different molecular weights. Macromolecular Materials and Engineering, **290**, 621–635 (2005).
DOI: 10.1002/mame.200500081

[20] Prashantha K., Lacrampe M. F., Krawczak P.: Processing and characterization of halloysite nanotubes filled polypropylene nanocomposites based on a masterbatch route: Effect of halloysites treatment on structural and mechanical properties. Express Polymer Letters, **5**, 295–307 (2011).
DOI: 10.3144/expresspolymlett.2011.30

[21] Ning N., Luo F., Wang K., Zhang Q., Chen F., Du R., An C., Pan B., Fu Q.: Molecular weight dependence of hybrid shish kebab structure in injection molded bar of polyethylene/inorganic whisker composites. The Journal of Physical Chemistry B, **112**, 14140–14148 (2008).
DOI: 10.1021/jp8056515

[22] Fang L. M., Gao P., Cao X W.: Temperature window effect and its application in extrusion of ultrahigh molecular weight polyethylene. Express Polymer Letters, **5**, 674–684 (2011).
DOI: 10.3144/expresspolymlett.2011.66

[23] Zhang C., Hu H., Wang X., Yao Y., Dong X., Wang D., Wang Z., Han C. C.: Formation of cylindrite structures in shear-induced crystallization of isotactic polypropylene at low shear rate. Polymer, **48**, 1105–1115 (2007).
DOI: 10.1016/j.polymer.2006.12.025

[24] Zhang C., Hu H., Wang D., Yan S., Han C. C.: *In situ* optical microscope study of the shear-induced crystallization of isotactic polypropylene. Polymer, **46**, 8157–8161 (2005).
DOI: 10.1016/j.polymer.2005.06.074

[25] Hsiao B. S., Yang L., Somani R. H., Avila-Orta C. A., Zhu L.: Unexpected shish-kebab structure in a sheared polyethylene melt. Physical Review Letters, **94**, 117802/1–117802/4 (2005).
DOI: 10.1103/PhysRevLett.94.117802

[26] Zhou Q., Liu F., Guo C., Fu Q., Shen K., Zhang J.: Shish–kebab-like cylindrulite structures resulted from periodical shear-induced crystallization of isotactic polypropylene. Polymer, **52**, 2970–2978 (2011).
DOI: 10.1016/j.polymer.2011.05.002

[27] Duplay C., Monasse B., Haudin J-M., Costa J-L.: Shear-induced crystallization of polypropylene: Influence of molecular structure. Polymer International, **48**, 320–326 (1999).
DOI: 10.1002/(sici)1097-0126(199904)48:4<320::aid-pi164>3.0.co;2-7

[28] Varga J., Karger-Kocsis J.: Rules of supermolecular structure formation in sheared isotactic polypropylene melts. Journal of Polymer Science Part B: Polymer Physics, **34**, 657–670 (1996).
DOI: 10.1002/(sici)1099-0488(199603)34:4<657::aid-polb6>3.0.co;2-n

[29] Wu C-M., Chen M., Karger-Kocsis J.: The role of metastability in the micromorphologic features of sheared isotactic polypropylene melts. Polymer, **40**, 4195–4203 (1999).
DOI: 10.1016/s0032-3861(98)00682-x

[30] Varga J., Karger-Kocsis J.: Direct evidence of row-nucleated cylindritic crystallization in glass fiber-reinforced polypropylene composites. Polymer Bulletin, **30**, 105–110 (1993).
DOI: 10.1007/bf00296241

[31] Li H., Jiang S., Wang J., Wang D., Yan S.: Optical microscopic study on the morphologies of isotactic polypropylene induced by its homogeneity fibers. Macromolecules, **36**, 2802–2807 (2003).
DOI: 10.1021/ma034062w

[32] Bogoeva-Gaceva G., Janevski A., Mader E.: Nucleation activity of glass fibers towards iPP evaluated by DSC and polarizing light microscopy. Polymer, **42**, 4409–4416 (2001).
DOI: 10.1016/s0032-3861(00)00659-5

[33] Yamazaki S., Itoh M., Oka T., Kimura K.: Formation and morphology of 'shish-like' fibril crystals of aliphatic polyesters from the sheared melt. European Polymer Journal, **46**, 58–68 (2010).
DOI: 10.1016/j.eurpolymj.2009.09.003

[34] Hobbs J. K., Register R. A.: Imaging block copolymer crystallization in real time with the atomic force microscope. Macromolecules, **39**, 703–710 (2005).
DOI: 10.1021/ma0514020

[35] Wang Y., Meng K., Hong S., Xie X., Zhang C., Han C. C.: Shear-induced crystallization in a blend of isotactic polypropylene and high density polyethylene. Polymer, **50**, 636–644 (2009).
DOI: 10.1016/j.polymer.2008.11.041

[36] Machado G., Kinast E. J., Scholten J. D., Thompson A., De Vargas T., Teixeira S. R., Samios D.: Morphological and crystalline studies of isotactic polypropylene plastically deformed and evaluated by small-angle X-ray scattering, scanning electron microscopy and X-ray diffraction. European Polymer Journal, **45**, 700–713 (2009).
DOI: 10.1016/j.eurpolymj.2008.12.015

[37] Li J. X., Cheung W. L., Jia D.: A study on the heat of fusion of β-polypropylene. Polymer, **40**, 1219–1222 (1999).
DOI: 10.1016/s0032-3861(98)00345-0

[38] Zheng G-Q., Huang L., Yang W., Yang B., Yang M-B., Li Q., Shen C-Y.: Hierarchical crystalline structure of HDPE molded by gas-assisted injection molding. Polymer, **48**, 5486–5492 (2007).
DOI: 10.1016/j.polymer.2007.05.047

[39] Zhao S., Xin Z., Zhang J., Han T.: Combined effect of organic phosphate sodium and nanoclay on the mechanical properties and crystallization behavior of isotactic polypropylene. Journal of Applied Polymer Science, **123**, 617–626 (2012).
DOI: 10.1002/app.34527

[40] Wang M.: Hierarchical orientational relaxation inducing shish-kebab formations in polymer melt crystallization. The Journal of Physical Chemistry B, **114**, 3488–3493 (2010).
DOI: 10.1021/jp911193r

eXPRESS Polymer Letters Vol.7, No.4 (2013) 365–374
Available online at www.expresspolymlett.com
DOI: 10.3144/expresspolymlett.2013.33

Crosslinking effect on the deformation and fracture of monodisperse polystyrene-co-divinylbenzene particles

J. Y. He[1], Z. L. Zhang[1], H. Kristiansen[2], K. Redford[2], G. Fonnum[3], G. I. Modahl[3]*

[1]NTNU Nanomechanical Lab, Department of Structural Engineering, Norwegian University of Science and Technology (NTNU), 7491 Trondheim, Norway
[2]Conpart AS, 2013 Kjeller, Norway
[3]Invitrogen Dynal AS, P.O.Box 114, Smestad, 0309 Oslo, Norway

Received 27 September 2012; accepted in revised form 9 December 2012

Abstract. This study focuses on the effect of crosslinking density on the mechanical response of polystyrene-co-divinylbenzene (PS-DVB) particles under compression by means of nanoindentation-based flat punch method combined with SEM observation of particle morphologies. The monodisperse PS-DVB particles with about 5 μm in diameter are produced by the Ugelstad activated swelling method and the crosslinking density defined as the weight percentage of activated crosslinker DVB during the preparation process varies from 2.0 to 55.3%. Results show that the particle stress–strain behaviour is independent of the crosslinking density if the strain is less than 10%. With increasing strain level over 10%, a higher crosslinking leads to a stiffer behaviour of the particles. While slightly crosslinked (2.0 and 5.0 wt%) particles undergo plastic deformation with crazing and residual strain, highly crosslinked (21.3, 32.0 and 55.3 wt%) counterparts experience perfectly viscoelastic deformation. The crosslinking density significantly influences the fracture property as well as the failure morphology. Slightly crosslinked particles become permanently deformed after compression, while highly crosslinked ones are entirely fragmented once a critical strain is reached.

Keywords: *nanocomposites, nanoindentation, mechanical properties, crosslinking density, damage mechanism*

1. Introduction

Micron-sized polymer particles have been widely used in chemical analysis and biotechnology, such as chromatographic supports, molecules carriers, additives in coating and ink products, and so on [1–3]. Recently increasing attention has been drawn to the use of polymer particles in electronic packaging technologies, for example Anisotropic Conductive Adhesive (ACA) by metallizing polymer particles [4, 5]. The use of metalized polymer particles with a typical size in the range of 3~10 μm, as substitute for compact metal particles, brings significant advantages in terms of decreasing package size, reducing environmental impact, increasing the interconnection compliance and hence improving the electrical reliability. To obtain a low resistance connection, large contact area between the particles and the contact pads is preferred, and thus the particles are exposed to a deformation exceeding 30% [6]. The mechanical characterization of particles under such a large deformation is necessary in order to ensure the electrical performance.

Polystyrene-co-divinylbenzene (PS–DVB) particles, due to their good mechanical properties, susceptibility to chemical modification and adaptability in a wide pH range, have been utilized in numerous applications, including in electronic packaging technology [7–10]. There are several methods available to synthesize crosslinked PS–DVB particles, such as suspension polymerization, dispersion poly-

*Corresponding author, e-mail: jianying.he@ntnu.no

merization, emulsion polymerization and seeded polymerization. However, these methods more or less have limitation on the preparation of PS–DVB particles for ACA. For example, by using suspension polymerization the particle size distribution is largely determined by stirring intensity, resulting in a broad size distribution and large particle diameter in the range of 20~1000 μm [11]. Dispersion polymerization is usually utilized to prepare particles with a low crosslinking density less than 1 wt%; otherwise it will lead to irregular shapes of particles [12]. The drawback of emulsion polymerization is that the technology for the required emulsion breaking is difficult to control [13]. Seeded polymerization is a relatively promising method to produce crosslinked particles but the enlargement of particles has been a hard work [14]. In contrast, the reformed seeded polymerization, known as Ugelstad method, has been developed to prepare highly monodisperse polymer particles which are well-controlled with a wide range of particle size, chemical composition and surface property [15,16]. In this study the Ugelstad method has been used to prepare monodisperse PS–DVB particles with same size and different crosslinking density.

Most theoretical and experimental studies on the mechanical properties of polymer materials have focused on bulky samples under tensile or shear test. The literature concerning mechanical properties of individual free-standing particles is relatively sparse and the existing ones mainly deal with particles larger than 100 μm [17]. Due to the small volume, spherical geometry and large deformation of polymer particles involved in ACA application, the mechanical characterization of individual micron-sized particles challenges the conventional experimental techniques in aspect of testing scale and resolution [18]. To cope with this, a nanoindentation-based flat punch method has been developed to successfully measure mechanical response of individual particles under compression [19, 20]. The deformation behaviour and failure properties of individual metal coated and uncoated polymer particles have been systematically investigated [21–23]. In a previous study, a striking size effect on the stress–strain relationship of PS–DVB particles with identical crosslinking density but different size has been discovered, which indicates that the smaller the diameter is, the harder the particle behaves [24].

In this work, we extend our research to another horizon toward the effect of crosslinking density on the mechanical properties of PS–DVB particles. The particles with identical size but different crosslinking density are measured by using the nanoindentation-based flat punch method. The nominal compression stress–strain behaviors of individual particles are obtained, and the deformation process as well as fracture properties of particles are analyzed with respect to the crosslinking density. The results facilitate the design of the crosslinked PS–DVB particles with desired mechanical properties.

2. Experimental

2.1. PS–DVB particles

Five groups of PS–DVB particles were synthesized by means of Ugelstad method, which was based on seeded polymerization and emulsion polymerization, involving a two-step activated swelling process, as shown in Figure 1 [15, 16, 25]. The particle matrices were poly(styrene-co-divinylbenzene). The crosslinking density of particles was determined by the amount of crosslinker – activated DVB during the synthesis, covering the following percentages 2.0, 5.0, 21.3, 32.0 and 55.3% by weight. The size of particles was controlled around 5 μm. The size distribution within each batch, given by the coefficient of variance (C.V.) was less than 3%, where C.V. was defined as the ratio of the standard deviation to the mean diameter. All PS–DVB particles were of amorphous type at room temperature. It was found that the glass transition temperature T_g of non-crosslinked linear polystyrene was about 100°C, and T_g increased while the thermal expansion coefficient decreased with increasing crosslink-

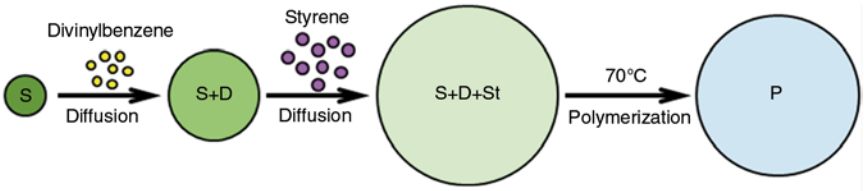

Figure 1. Preparation of highly monodisperse PS-DVB particles by using Ugelstad method, S: seed; D: divinylbenzene; St: styrene; P: particle

Table 1. The properties of PS–DVB particles. The amount of DVB presents the crosslinking density of particles

Particles	DVB [wt%]	Styrene [wt%]	Diameter [μm]	CV [%]
PSA	2.0	98.0	5.1	0.8
PSB	5.0	95.0	5.2	1.4
PSC	21.3	78.7	5.3	2.8
PSD	32.0	68.0	5.2	1.6
PSE	55.3	44.7	5.2	1.6

ing density [26, 27]. This implied that all particles remained amorphous during the measurement at room temperature. According to the crosslinking degree, particles could be divided into two groups in which PSA and PSB were slightly crosslinked and the rest three PSC, PSD and PSE were highly crosslinked. The dispersion method developed in the previous study was used to obtain individual particles [24]. The particles and the corresponding physical properties are given in Table 1.

2.2. Nanomechanical test

The mechanical testing of particles was performed by using the nanoindentation-based flat punch technique (TriboIndenter® Hysitron) [19]. It could be considered as an inverse nanoindentation schematically shown in Figure 2. Instead of an ordinary sharp indenter with pyramidal or spherical geometry for nanohardness measurement, a diamond flat punch with a flat end of about 10 μm in diameter was designed to compress individual particles. The standard load-control mode for common nanoindentation measurement was employed, in which the applied load followed a predefined load function. A three-step loading protocol was used, including linear loading with 2 mN/s loading rate, 2 s holding at the peak load and linear unloading with –2 mN/s loading rate. The applied force and the contact displacement were monitored during test and the real-time force–displacement relationship was obtained. The compression test was repeated on different individual particles from the same group to ensure the repeatability of the results. Experience with Ugelstad PS–DVB particles proved that particles from the same manufacturing batch showed remarkably consistent behaviour [24]. This indicated a homogeneous material from perspective of geometry and microstructure, even with highly reproducible experimental setup.

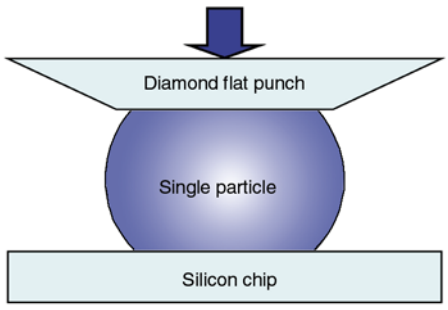

Figure 2. Schematic of the nanoindentation-based flat punch test

2.3. SEM observation

The as-prepared particle morphology was characterized by using scanning electron microscope (SEM) (FEI Helios NanoLab DualBeam™). The applied electron high tension (EHT) and the working distance (WD) were set to 5.0 kV and 4.0 mm, respectively. The fracture pattern was examined by a field emission SEM (Zeiss Ultra 55 LE FESEM®). Prior to imaging, the compressed particles rested in a clean environment for two weeks in order to complete the recovery of potential residual deformation. To minimize the damage from the electron beam and charge dissipation, the EHT and WD were set to relatively low values 0.5 kV and 2.0 mm.

3. Results and discussion

3.1. Particles morphology

The surface morphologies of five groups of PS–DVB particles obtained by Ugelstad method are shown in Figure 3. The monodisperse size distribution and the spherical shape of particles are displayed, which indicates the well-controlled process of Ugelstad method. The particles with different crosslinking density keep nearly identical size about 5 μm in diameter. While the surfaces of the slightly crosslinked particles are smoother than that of the highly crosslinked ones. Tiny pores on the surface of highly crosslinked particles exist and aggravate with the increasing crosslinking density.

During the synthesis of particles, the polymerization is a coupled process of chemical (reaction) control and diffusion control. Resulting from an inhomogeneous distribution of crosslinking monomer, an inhomogeneous microstructure consisting of granules can form [28]. The granules can be considered as the aggregates of typically tiny particles with higher crosslinking density than the average. These highly crosslinked aggregates act as inclusions or second phase particles within polymer.

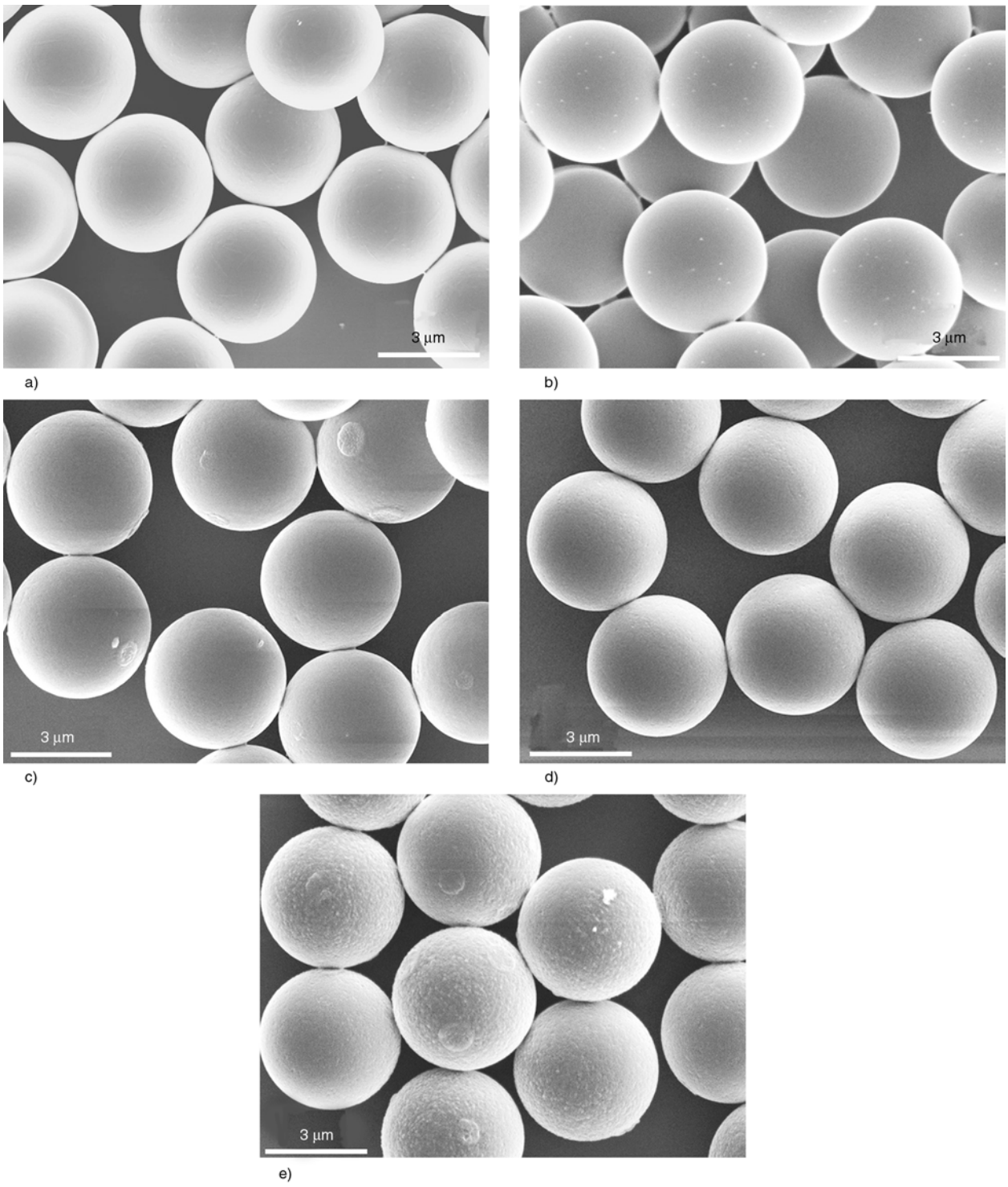

Figure 3. SEM photograph of the PS–DVB particle. (a–e) present particle PSA, PSB, PSC, PSD and PSE, respectively. Electron high tension (EHT) = 5.0 kV; working distance (WD) = 4.0 mm.

Although they are in an ultrafine scale, the presence of such aggregates strongly affects the mechanical properties of polymer matrix. It has been observed that the more densely crosslinked polymer is more heterogeneous and the crack in such polymer materials propagates in the regions with a relatively low crosslinking density between highly crosslinked clusters, which is consistent with our findings [28].

3.2. Compression behaviour

Systematic experiments show that the two slightly crosslinked particles have nearly identical behaviour and three highly crosslinked ones follow the same deformation pattern. The representative force–displacement curves of the lowest crosslinked particle PSA and the highest crosslinked PSE are plotted in Figure 4 and Figure 5, respectively. The com-

pression peak loads are 1.5 and 20 mN applied on PSA, and 5 and 20 mN on PSE. In each figure two or three force–displacement curves of virgin particles are presented. It can be observed that the loading segments of the two groups of particles are repeatable and consistent. This is in contrast to bulky polymer materials in which the mechanical properties, especially the fracture point, often show a large scatter due to heterogeneous microstructure, and microscopic defects including variation in local crosslinking density and anisotropy, etc. [29]. The particle deformation is defined as the ratio of the contact displacement to the undeformed particle diameter. Under the compression at small peak load 1.5 mN, particle PSA hardly recovers any deformation, while PSE compressed to 5 mN shows over 60% recovery of the deformation immediately after unloading. When compressed to the peak load 20 mN, the particle PSA deforms continuously although a significant displacement burst occurs on the loading segment of PSE. The displacement burst, also called 'pop-in', implies destructive failure of the particles [20]. Whereas the displacement increases a relatively large extent at the pop-in, the contact force drops because infinitesimal counterforce arises from the crushed particle. During unloading both particles have negligible deformation recovery. For the two slightly crosslinked particles we found that even increasing the peak load to 30 mN there is no displacement burst. Moreover, the three highly crosslinked particles always show a large deformation recovery when unloading starts prior to the displacement burst.

The characteristic SEM images of particle PSA and PSE corresponding to the force–displacement curves in Figure 4 and Figure 5 are shown in Figure 6. All images are taken from the top view, in the direction of compression. While undeformed particle PSA has a smooth surface morphology, PSE is relatively rough. In Figure 6a, for particle PSA compressed at

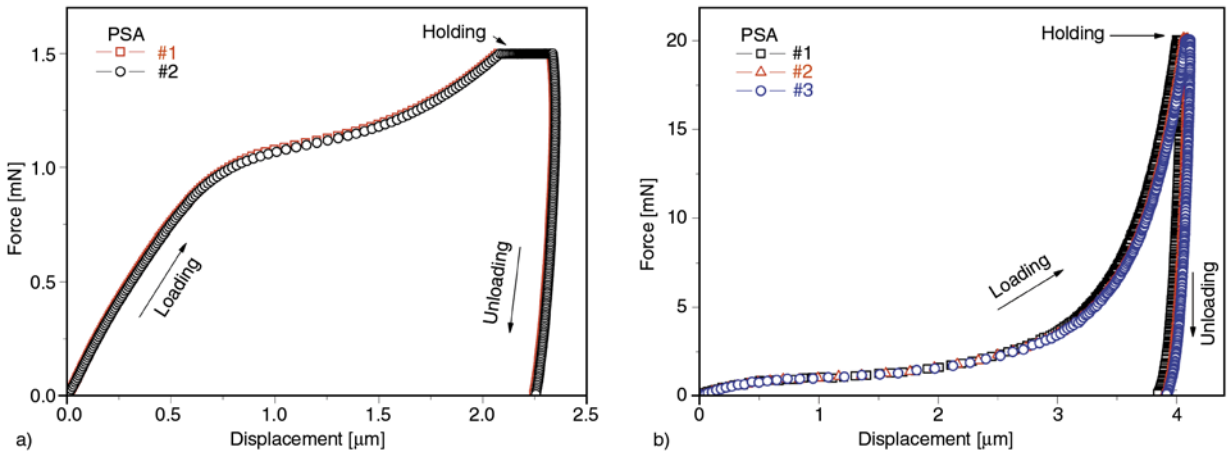

Figure 4. The representative force–displacement curves of slightly crosslinked particle PSA at different peak load (a) 1.5 mN and (b) 20 mN

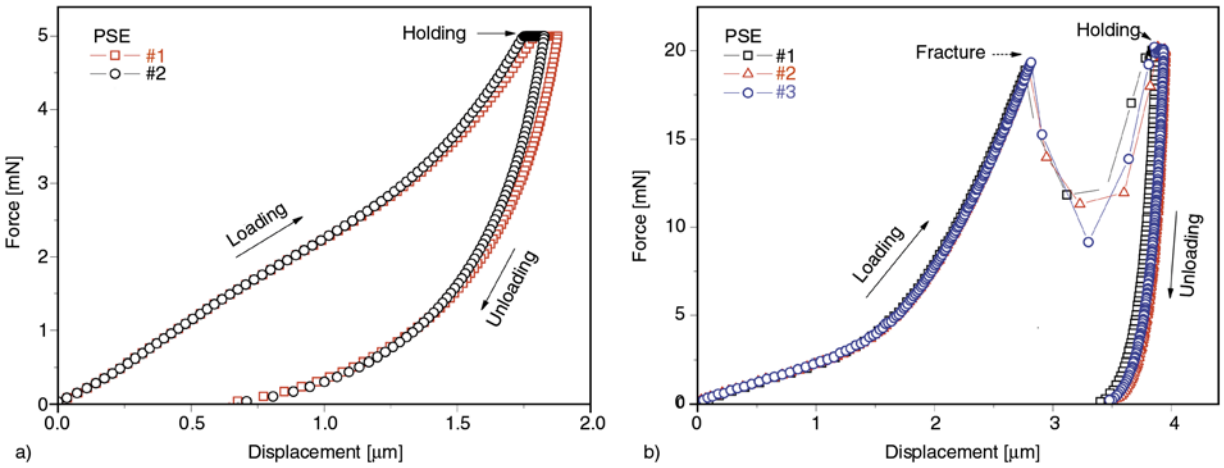

Figure 5. The representative force–displacement curves of highly crosslinked particle PSE at different peak load (a) 5 mN and (b) 20 mN

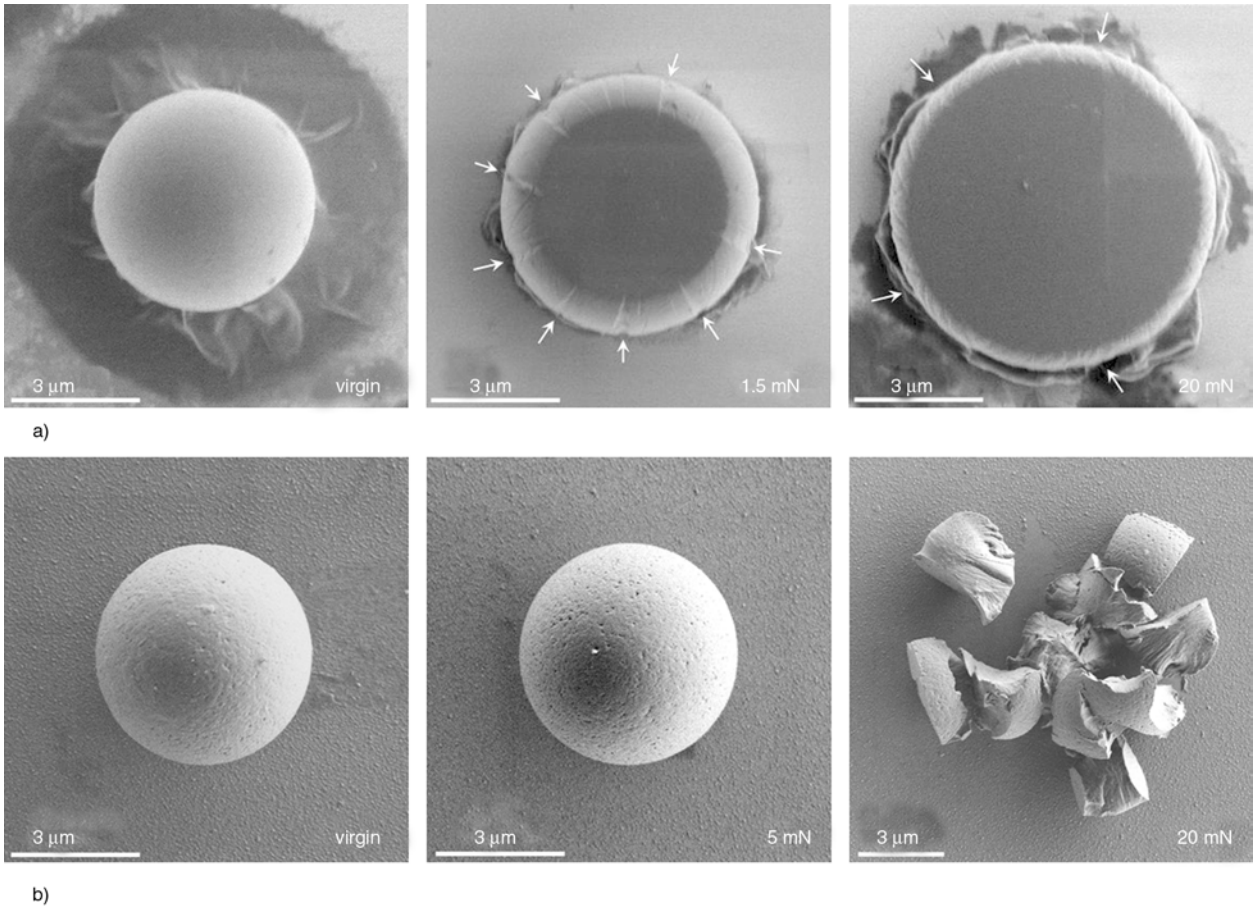

Figure 6. The characteristic SEM images of particle morphology after compression, (a) PSA and (b) PSE. Electron high tension (EHT) = 0.5 kV; working distance (WD) = 2.0 mm.

1.5 mN peak load, a flattened surface area is observed which corresponds to the expected contact area and indicates the residual deformation. Isolated crazes can be observed, as indicated by arrows in the corresponding micrograph. The craze formation is originated from the tensile region of deformed drum-like particles under compression. When the peak load is up to 20 mN, the particle becomes oblate with a large number of interacted crazes around the edge. In Figure 6b, particle PSE shows a drastically different behavior from particle PSA. In the case of compression at the peak load of 5 mN, there is no craze, even no evidence of the contact area observed. The particle completely recovers the residual deformation presented in Figure 5a and has identical size with the undeformed one. Further compressing the particle to 20 mN, fragmentation occurs.

The results of compression test and SEM observation suggest that the slightly crosslinked particles behave plastically with the presence of local brittle crazes and residual deformation after unloading; while the highly crosslinked counterparts display viscoelastic behaviour, which recover completely within a certain time after unloading.

3.3. Deformation process and fracture

Both microstructure and geometry influence the mechanical response of the particle. To eliminate the effect of variation in particle size, the force–displacement results are normalized to the stress–strain relationship. Similar to the previous study, the nominal compression stress–strain relationships of the particles are adopted, as shown by Equations (1) and (2) [18]:

$$\sigma_C = \frac{P}{\pi R^2} \tag{1}$$

$$\varepsilon_C = \frac{D}{2R} \tag{2}$$

where σ_C is the nominal compression stress, ε_C is the nominal compression strain, R is the initial radius of the particle, P is the contact force, and D is the particle displacement. The nominal compression stress–strain curves of the five groups of parti-

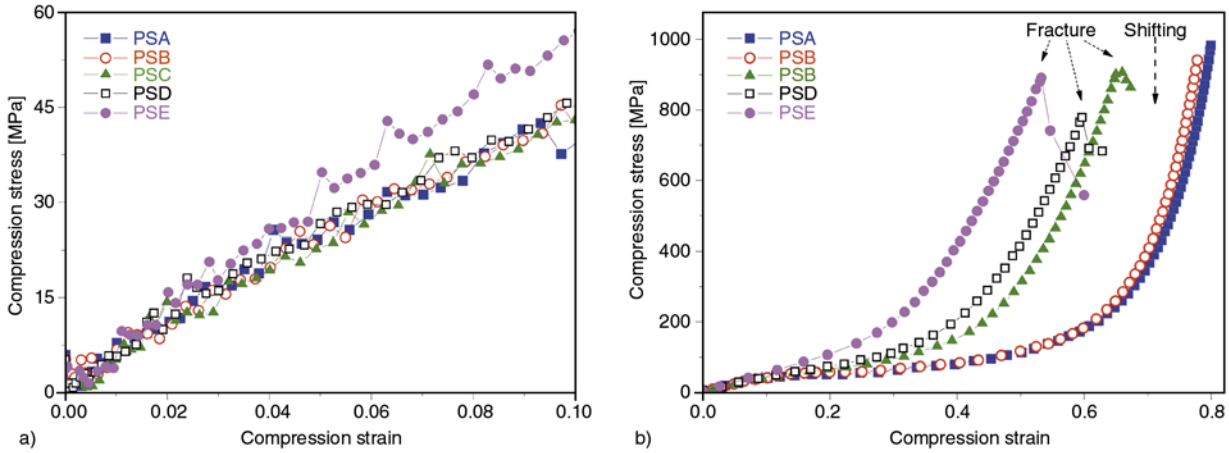

Figure 7. Compression stress–strain curves of five PS–DVB particles (a) at small strain level and (b) at large strain level

cles at different strain levels are plotted in Figure 7. The focus of this study is on the loading behaviour of particles, thus the holding and unloading segments on the stress–strain curves are disregarded. During the large deformation of particles under compression, the contact between the particle and punch/substrate changed from point to a finite area continuously and the spherical geometry induce highly nonlinear stress–strain behaviour.

At small strain level below 10%, as shown in Figure 7a, the stress–strain behaviour of particles appears independent on the crosslinking density, indicating that the reduced *E*-modulus at small strains are similar for different crosslinked particles. The macroscopic elastic deformation is mainly determined by the elastic properties of the polymer chain [30]; accordingly the effect of different crosslinking density is suppressed. However, as the strain increases over the level of 10%, the effect of crosslinking becomes pronounced. The higher crosslinking density induces stiffer behaviour, as shown in Figure 7b. At this stage, a significant rearrangement of the polymer chains for the slightly crosslinked particles is expected, whereas the structure is much more locked for the highly crosslinked ones. The major difference occurs at high strains where the two slightly crosslinked particles PSA and PSB can deform up to 80% without stress drop, while the highly crosslinked PSC, PSD and PSE show a complete fragmentation of the particles.

The compression stress of PS–DVB particles at different strain levels are summarized in Figure 8 where the distinct effect of crosslinking density is illustrated. At the strain level less than 10%, the effect of crosslinking density is relatively mild, as shown in Figure 8a, for example the five groups of particles have nearly identical compression stress when the stain level is 2%. As increasing the strain level above 10%, the effect of the crosslinking density becomes more and more evident. To deform the

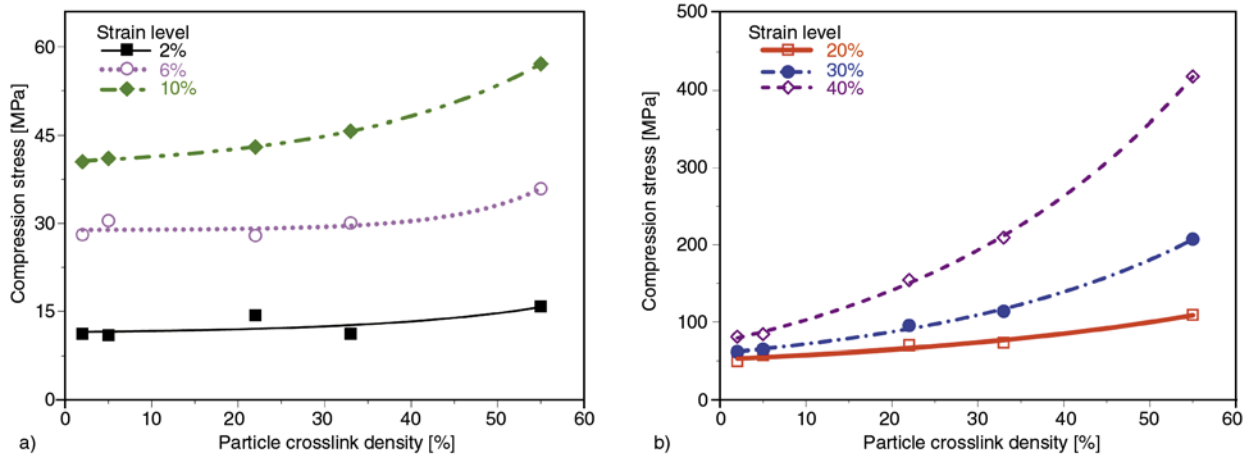

Figure 8. The crosslinking density effect on the compression stress of five PS–DVB particles (a) at small strain scale and (b) at large strain scale. The lines are guides for the eye.

five groups of particles to a relatively large strain level, the compression stress dramatically raise with the crosslinking density.

The deformation behaviour in polymer materials is often classified in three modes: plastic behaviour, rubber-like behaviour and brittle fracture behaviour [31]. Non-crosslinked linear polystyrene is found to exhibit brittle crazing in tension, while plastic behaviour in compression through shear banding or shear yielding [32]. Crazing is a localized yielding behaviour and characterized as whitening of the polymer in the region of maximum deformation through formation of micro-cracks, which are bridged by polymer fibrils. Shear banding, which is highly dependent on temperature and strain rate, is featured by planes of slip at 45° to the direction of stress and involves the local orientation of the polymer. For bulky crosslinked polymers, it is known that the mechanical properties are sensitive to the crosslinking density [33]. Crosslinking increases the tightness of the polymer network and limits the molecular mobility of chains between the junctions. The randomly crosslinked network of polymers undergoes a transition from a fluid to an amorphous solid state behaviour as the crosslinking increases [34]. The characteristic length between crosslinking decreases with the increasing crosslinking density. This means that the available degrees of freedom in rearranging the molecular chain decreases with an increasing degree of crosslinking.

However, in the present work, the spherical geometry increases the complexities of the stress and strain distribution in the particle. The compression on the particles induces a drum-like pattern consisting of both compressive and tensile components. The maximum tensile stress induced by the compression is located in the circumferential direction Thus a number of crazes at the toroid surface and residual deformation are observed on the slightly crosslinked particles with plastic behaviour, whose deformation is comparable with the linear polystyrene. There is no definite yielding point on the stress–strain curves but a long plateau implying the plastic flow following by strain hardening, as shown in Figure 7b. With increasing crosslinking density, the crosslinking restricts the deformability and three highly crosslinked particles show viscoelastic behaviour. The SEM observation confirms full recovery of particles or fragmentation at high peak load without craze formation although there are compressive and tensile region during compression.

When increasing the crosslinking density from 5.0 to 21.3 wt%, the particle deformation changes from plastic deformation to viscoelastic behaviour. Due to the lack of PS–DVB particles located in the region between 5.0 and 21.3 wt% of crosslinking density, the more detailed information of the shift of fracture pattern is not available. According to the nature of polymer materials, this change is influenced by strain rate and temperature. It is difficult to define an exact shift point of a critical crosslinking density.

It is worth noting that the deformation and fracture pattern of particles observed in this study is simply valid for the PS–DVB particles within the sampling crosslinking density. As mentioned above, the crosslinking density is determined by the amount of DVB containing two vinyl groups during particle preparation. When adding more DVB, it might be supersaturated and not fully reacted with styrene monomer. It will result in a lower effective crosslinking density than calculated from the amount of DVB.

4. Conclusions

By using a nanoindentation-based flat punch method, the effect of the crosslinking density on the mechanical properties of monodisperse PS–DVB particles has been systematically investigated. The monodisperse PS-DVB particles are prepared by the well-known Ugelstad activated swelling method. The amount of crosslinking agent in the particles varies from 2.0 to 55.3% by weight and the diameter of particles is kept around 5 μm. The deformation mechanism of slightly crosslinked particles has been clarified to be plastic behaviour while highly crosslinking ones are viscoelastic. At the strain level below 10%, particle deformation appears to be nearly independent of the crosslinking density. This is associated with the elasticity of styrene segments between neighboring crosslinking points. With the increase of strain, the crosslinking density effect becomes pronounced. The major difference occurs on the fracture behaviour. The slightly crosslinked particles show densely crazes and the failure of the highly crosslinked ones is presented by the direct evidence of fragmentation. The mechanism behind the observation is that the high

crosslinking restricts the deformability of particles and also causes a heterogeneous microstructure.

Acknowledgements

This work is supported by The Research Council of Norway via NANOMAT KMB Projects NanoPCP (Grant No. NANOMAT-169737/S10) and MS2MP (Grant No. NANOMAT-187269), and long-term support from NorFab Norway. The authors gratefully acknowledge Wilhelm Dall for assistance with SEM operation.

References

[1] Ahmad H., Tauer K.: Effects of chain transfer agent on the radical polymerization of styrene in non-aqueous dispersion. Colloid and Polymer Science, **281**, 686–689 (2003).
DOI: 10.1007/s00396-002-0847-0

[2] Toprak M. S., Mckenna B. J., Mikhaylova M., Waite J. H., Stucky G. D.: Spontaneous assembly of magnetic microspheres. Advanced Materials, **19**, 1362–1368 (2007).
DOI: 10.1002/adma.200602114

[3] Kim K., Kim Y., Ko N. R., Choe S.: Effect of molecular weight on the surface morphology of crosslinked polymer particles in the RITP-dispersion polymerization. Polymer, **52**, 5439–5444 (2011).
DOI: 10.1016/j.polymer.2011.10.015

[4] Kwon W-S., Paik K-W.: Experimental analysis of mechanical and electrical characteristics of metal-coated conductive spheres for anisotropic conductive adhesives (ACAs) interconnection. IEEE Transactions on Components and Packaging Technologies, **29**, 528–534 (2006).
DOI: 10.1109/TCAPT.2006.880513

[5] Lin Y. C., Zhong J.: A review of the influencing factors on anisotropic conductive adhesives joining technology in electrical applications. Journal of Materials Science, **43**, 3072–3093 (2008).
DOI: 10.1007/s10853-007-2320-4

[6] Kristiansen H., Liu J.: Overview of conductive adhesive interconnection technologies for LCDs. IEEE Transactions on Components, Packaging, and Manufacturing Technology, **21**, 208–214 (1998).
DOI: 10.1109/95.705466

[7] Ellingsen T., Aune O., Ugelstad J., Hagen S.: Monosized stationary phases for chromatography. Journal of Chromatography A, **535**, 147–161 (1990).
DOI: 10.1016/S0021-9673(01)88940-8

[8] Song J-S., Winnik M. A.: Monodisperse, micrometer-sized low molar mass polystyrene particles by two-stage dispersion polymerization. Polymer, **47**, 4557–4563 (2006).
DOI: 10.1016/j.polymer.2006.04.025

[9] Tanaka T., Suzuki T., Saka Y., Zetterlund P. B., Okubo M.: Mechanical properties of cross-linked polymer particles prepared by nitroxide-mediated radical polymerization in aqueous micro-suspension. Polymer, **48**, 3836–3843 (2007).
DOI: 10.1016/j.polymer.2007.04.040

[10] Li L., Fang T.: Anisotropic conductive adhesive films for flip chip on flex packages. in 'Proceedings of the 4th International Conference on Adhesive Joining and Coating Technology in Electronics Manufacturing, Espoo, Finland' 129–135 (2000).
DOI: 10.1109/ADHES.2000.860586

[11] Ahmed S. M.: Effects of agitation, and the nature of protective colloid on particle size during suspension polymerization. Journal of Dispersion Science and Technology, **5**, 421–432 (1984).
DOI: 10.1080/01932698408943229

[12] Thomson B., Rudin A., Lajoie G.: Dispersion copolymerization of styrene and divinylbenzene. II. Effect of crosslinker on particle morphology. Journal of Applied Polymer Science, **59**, 2009–2028 (1996).
DOI: 10.1002/(SICI)1097-4628(19960328)59:13<2009::AID-APP6>3.0.CO;2-L

[13] Ishizu K., Tahara N.: Microsphere synthesis by emulsion copolymerization of methyl methacrylate with binary macromonomer blends. Polymer, **37**, 1729–1734 (1996).
DOI: 10.1016/0032-3861(96)83726-8

[14] Okubo M., Shiozaki M., Tsujihiro M., Tsukuda Y.: Preparation of micron-size monodisperse polymer particles by seeded polymerization utilizing the dynamic monomer swelling method. Colloid and Polymer Science, **269**, 222–226 (1991).
DOI: 10.1007/BF00665495

[15] Ugelstad J., Mørk P. C., Kaggerud K. H., Ellingsen T., Berge A.: Swelling of oligomer-polymer particles. New methods of preparation. Advances in Colloid and Interface Science, **13**, 101–140 (1980).
DOI: 10.1016/0001-8686(80)87003-5

[16] Ugelstad J., Berge A., Ellingsen T., Schmid R., Nilsen T. N., Mørk P. C., Stenstad P., Hornes E., Olsvik Ø.: Preparation and application of new monosized polymer particles. Progress in Polymer Science, **17**, 87–161 (1992).
DOI: 10.1016/0079-6700(92)90017-S

[17] Liu K-K.: Deformation behaviour of soft particles: A review. Journal of Physics D: Applied Physics, **39**, R189–R199 (2006).
DOI: 10.1088/0022-3727/39/11/R01

[18] Zhang Z. L., Kristiansen H., Liu J.: A method for determining elastic properties of micron-sized polymer particles by using flat punch test. Computational Materials Science, **39**, 305–314 (2007).
DOI: 10.1016/j.commatsci.2006.06.009

[19] He J. Y., Zhang Z. L., Kristiansen H.: Nanomechanical characterization of single micron-sized polymer particles. Journal of Applied Polymer Science, **113**, 1398–1405 (2009).
DOI: 10.1002/app.29913

[20] Kim D. O., Jin J. H.: Investigation for surface morphology and mechanical property variations of single polymer particles. Journal of Applied Polymer Science, **104**, 2350–2360 (2007).
DOI: 10.1002/app.25717

[21] He J. Y., Zhang Z. L., Kristiansen H.: Compression properties of individual micron-sized acrylic particles. Materials Letters, **63**, 1696–1698 (2009).
DOI: 10.1016/j.matlet.2009.05.013

[22] He J. Y., Helland T., Zhang Z. L., Kristiansen H.: Fracture of micron-sized Ni/Au coated polymer particles. Journal of Physics D: Applied Physics, **42**, 085405/1–085405/5 (2009).
DOI: 10.1088/0022-3727/42/8/085405

[23] He J. Y., Nagao S., Kristiansen H., Zhang Z. L.: Loading rate effects on the fracture of Ni/Au nano-coated acrylic particles. Express Polymer Letters, **6**, 198–203 (2012).
DOI: 10.3144/expresspolymlett.2012.22

[24] He J. Y., Zhang Z. L., Midttun M., Fonnum G., Modahl G. I., Kristiansen H., Redford K.: Size effect on mechanical properties of micron-sized PS–DVB polymer particles. Polymer, **49**, 3993–3999 (2008).
DOI: 10.1016/j.polymer.2008.07.015

[25] Ugelstad J.: Monodisperse polymer particles and dispersions thereof. U.S. Patent 4459378, USA (1984).

[26] Ding J., Xue G., Dai Q., Cheng R.: Glass transition temperature of polystyrene microparticles. Polymer, **34**, 3325–3327 (1993).
DOI: 10.1016/0032-3861(93)90412-4

[27] Bandyopadhyay A., Valavala P. K., Clancy T. C., Wise K. E., Odegard G. M.: Molecular modeling of crosslinked epoxy polymers: The effect of crosslink density on thermomechanical properties. Polymer, **52**, 2445–2452 (2011).
DOI: 10.1016/j.polymer.2011.03.052

[28] Rey L., Duchet J., Galy J., Sautereau H., Vouagner D., Carrion L.: Structural heterogeneities and mechanical properties of vinyl/dimethacrylate networks synthesized by thermal free radical polymerisation. Polymer, **43**, 4375–4384 (2002).
DOI: 10.1016/S0032-3861(02)00266-5

[29] VanLandingham M. R., Villarrubia J. S., Guthrie W. F., Meyers G. F.: Nanoindentation of polymers: An overview. Macromolecular Symposia, **167**, 15–44 (2001).
DOI: 10.1002/1521-3900(200103)167:1<15::AID-MASY15>3.0.CO;2-T

[30] Vakil U. M., Martin G. C.: Crosslinked epoxies: Network structure characterization and physical–mechanical properties. Journal of Applied Polymer Science, **46**, 2089–2099 (1992).
DOI: 10.1002/app.1992.070461204

[31] Strobl G.: The physics of polymers. Springer, Heidelberg (2007).

[32] Chow T. S.: Stress–strain behavior of polymers in tension, compression, and shear. Journal of Rheology, **36**, 1707–1717 (1992).
DOI: 10.1122/1.550281

[33] Wang S., Yaszemski M. J., Gruetzmacher J. A., Lu L.: Photo-crosslinked poly(ε-caprolactone fumarate) networks: Roles of crystallinity and crosslinking density in determining mechanical properties. Polymer, **49**, 5692–5699 (2008).
DOI: 10.1016/j.polymer.2008.10.021

[34] Ulrich S., Mao X., Goldbart P. M., Zippelius A.: Elasticity of highly cross-linked random networks. Europhysics Letters, **76**, 677–682 (2006).
DOI: 10.1209/epl/i2006-10310-7

eXPRESS Polymer Letters Vol.7, No.4 (2013) 375–382
Available online at www.expresspolymlett.com
DOI: 10.3144/expresspolymlett.2013.34

Zener tunneling in conductive graphite/epoxy composites: Dielectric breakdown aspects

*L. X. He, S. C. Tjong**

Department of Physics and Materials Science, City University of Hong Kong, Hong Kong

Received 29 october 2012; accepted in revised form 3 January 2013

Abstract. The electrical responses of conductive graphite/epoxy composites subjected to an applied electric field were investigated. The results showed that reversible dielectric breakdown can easily occur inside the composites even under low macroscopic field strengths. This is attributed to the Zener effect induced by an intense internal electric field. The dielectric breakdown can yield new conducting paths in the graphite/epoxy composites, thereby contributing to overall electrical conduction process.

Keywords: *polymer composites, electrical properties, physical methods of analysis, Zener effect*

1. Introduction

Polymer composites with conducting particles such as metals and carbon blacks (CBs) find useful industrial applications in the fields of switching elements, sensors, actuators and electromagnetic shielding [1–4]. For these composites, the electrical conductivity (σ) increases slowly with increasing filler concentration (p), but then rises significantly when their filler content reaches a critical concentration, generally known as the percolation threshold (p_c). From the percolation theory, the relation between σ and p_c is given by Equation (1) [5–7]:

$$\sigma = \sigma_0(p - p_c)^t \quad (1)$$

where σ_0 is the conductivity scale factor related to the intrinsic conductivity of the filler and t the critical exponent depending on the dimensionality of the system, i.e. 1.6–2.0 for three dimensional, and 1.0–1.3 for two dimensional systems [7].

Percolative polymer composites usually display nonlinear electrical conduction behavior [8–12]. The application of electrical field in the composites can also lead to a nonlinear response. This is because the resistance of the composites changes from linear to nonlinear as the applied filed increases. When the field exceeds relatively large values, local joule heating of the elements occurs, causing irreversible damage in the structure of materials [13]. This is commonly referred to as the electrical failure or dielectric breakdown of the system. The irreversibility can be prevented if the current through the material is well-controlled. Alternatively, materials with nanoscale dimensions are reported to be effective for providing local heat sinks and preventing irreversible changes in the materials [14]. Therefore, dielectric breakdown of the polymer composites with conductive and nonconductive nanofillers has received considerable attention recently [14–17]. Very recently, Song *et al*. [16] reported factors influencing the breakdown strength of the ceramic oxide particle/polymer nanocomposites.

Nonlinear electrical transport can also occur in the composite materials by applying relatively small

*Corresponding author, e-mail: aptjong@cityu.edu.hk

electric field. The reversible nonlinear response is more complicated in the presence of tunneling conduction. The physical mechanisms responsible for such nonlinearity remain unclear. Sen *et al.* [18, 19] reviewed and analyzed nonlinear and dielectric breakdown of disordered composite materials systematically. Particular attention was paid to the reversible breakdown of the materials. In a previous study, we explored the effect of Zener tunneling in various carbon/polymer composites [20]. In this work, we attempt to establish a relationship for nonlinear electrical transport in the graphite/epoxy composites. We show that the reversible nonlinear behavior of the composite derives from local dielectric breakdown, or Zener tunneling.

2. Experimental

Graphite powder flakes of irregular shapes with an average size of ~20 μm (Product No. 332461, Sigma-Aldrich) and epoxy resin (86.4% bisphenol and 13.6% N-butly glycidyl ether; Cat. No. Ultra-3000R-128, Pace Technologies, Inc.) were used as conducting fillers and insulating matrix respectively. In a typical fabrication process, the epoxy was dissolved in acetone, followed by adding graphite powders. The suspension was sonicated for 2 h to ensure homogeneous dispersion of the graphite powders. Then the solution was kept at 50°C for 12 h for fully removal of acetone. This was followed by adding the hardener (100% diethylenetriamine; Cat. No. Ultra-3000H-32, Pace Technologies, Inc.) to the graphite/epoxy mixture at a ratio of 1:10 by weight. The mixed liquid was stirred for 10 min in order to ensure homogeneous filler dispersion and to achieve good epoxy/hardener blending. Then the mixture was left in vacuum at room temperature for 24 h. This led to full curing and crosslinking of the epoxy, yielding better dispersion of the fillers in the epoxy resin [21]. After curing, disk-like samples with a diameter of 10 mm and a thickness of about 1 mm were obtained. They were treated with silver paste to form the electrodes for the electrical measurements. A Hewlett Packard 4140B pA meter/DC voltage source with pulse testing voltage was used to measure the electrical responses. It required about 2–3 seconds for achieving the equilibrium DC conductivity. The voltage used to determine the DC conductivity was 500 mV. Ten samples were measured for each composite, and the obtained values were averaged. The scatter bars in the plot indicate the fluctuation of the conductivity. The dispersion of the graphite powders was examined using an optical microscope (OM, Olympus BH-2) in a transmission mode. The morphology of the composites was examined in a JSM 820 scanning electron microscope (SEM). The specimens for the microscopic observations were cut to about 20 μm using a Reichert Ultra Cut S cutter.

3. Results and discussion

Figure 1 shows the optical micrographs of the fabricated graphite/epoxy composites. Figure 2 shows the SEM micrographs of several composite samples. The graphite powders are dispersed uniformly in the polymer matrix when the filler content ≤8 vol%. At a higher filler loading (9.3 vol%), the graphite powders tend to aggregate somewhat in the polymer matrix (see Figure 1f).

Figure 3 shows the plot of static conductivity $\sigma(p)$ against filler content for the samples studied. The conductivity follows the percolation theory as expected. By fitting the data to Equation (1), the percolation threshold pc and the critical exponent t are determined to be 4.8±0.6 and 2.3±0.4, respectively. When the graphite content reaches near 4.8 vol%, an infinite conducting network spanning the whole system begins to form. And the static conductivity at this content is expected to show a sharp increase. As mentioned above, t takes the value of 1.6–2.0 for three dimensional, and 1.0–1.3 for two dimensional system. However, it may become non-universal due to a large variation in the distribution of distances among conductive fillers within the polymer matrix [22]. Large t values have also been reported in other polymer composite systems [23–25].

The current density (J) as a function of electric field (E) for these samples is shown in Figures 4a–4f, respectively. These experimental data is highly reproducible and completely reversible, indicating no damage to the material by the electric field. However, the electrical conductivity of all samples rises with increasing field strength. This reversible conductivity is considered to be of particular interest. It may arise from two ways: in one case, the conducting elements are nonohmic while in another, the conducting elements are ohmic but their macroscopic conductivity becomes nonohmic due to the creation of additional channels for conduction [26]. Herein, we use a two dimensional random-bond model (Figure 5) to illustrate the conduction paths

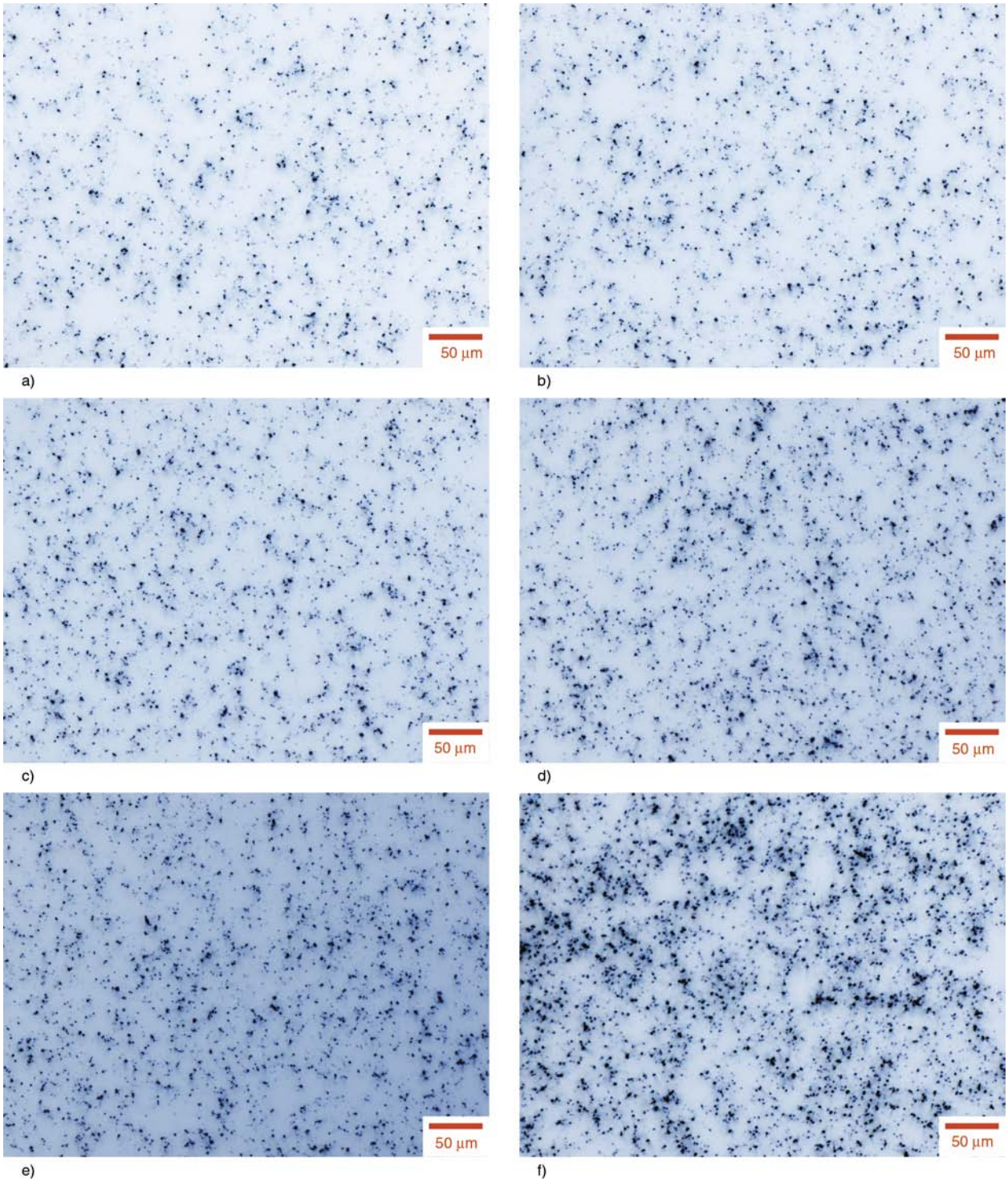

Figure 1. Transmission optical micrographs of graphite/epoxy composites with (a) 6 vol%, (b) 6.4 vol%, (c) 6.8 vol%, (d) 7.4 vol%, (e) 8 vol% and (f) 9.3 vol% filler content

involved in the graphite/epoxy composites. Because of the presence of the conducting clusters in the insulating matrix, local discontinuities in the field strength can be expected. For narrow insulating gaps between these clusters (①), the field strength is magnified by a factor γ given by the ratio of the average size of the conducting clusters to the average gap width [27]. At the tips of these clusters, this magnified field concentrates locally to a large extent. Likewise, high electric field may also establish between different parts of the backbone (②), or between the backbone and the clusters (③). Therefore, it is proposed that micro dielectric breakdown would occur at these insulating layers. The conduction paths induced by dielectric breakdown would lead to an additional conducting network, i.e. a

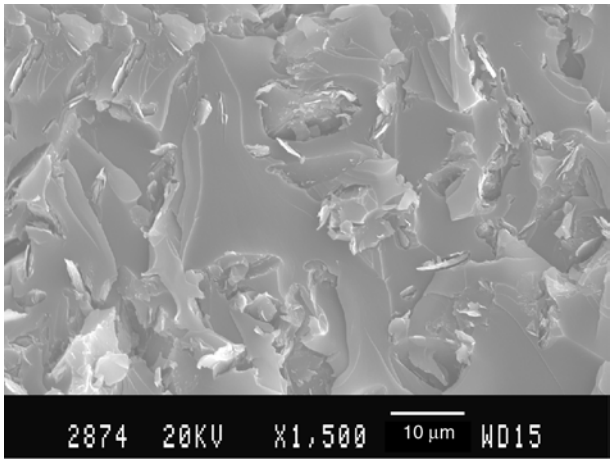

a)

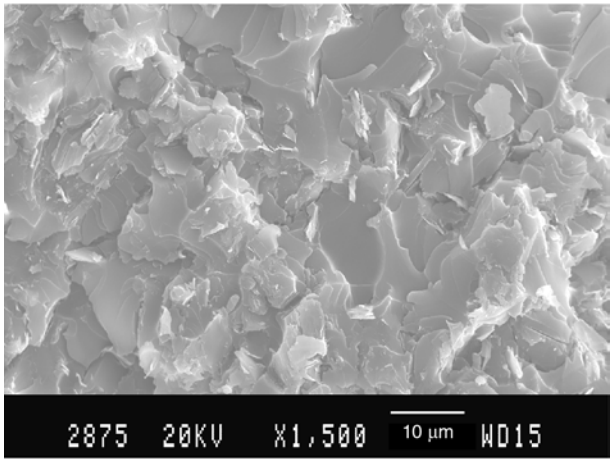

b)

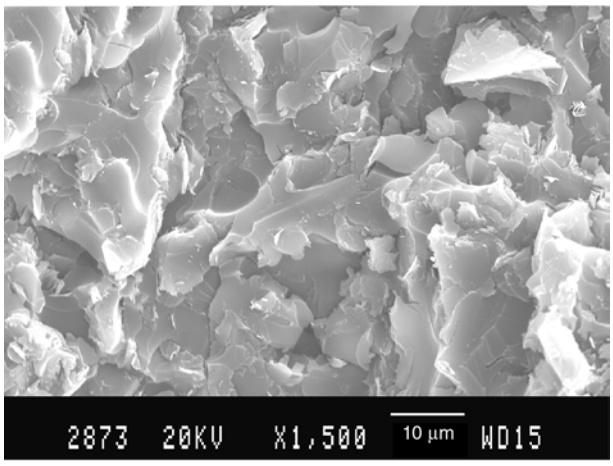

c)

Figure 2. SEM images of graphite/epoxy composites with (a) 6 vol%, (b) 8 vol% and (c) 9.3 vol% filler content

breakdown network, which is responsible for the macroscopic dielectric breakdown. This network can lead to a nonlinear increase in the conductivity of the system.

The specific dielectric breakdown mechanism can be categorized into two types. The most common is avalanche breakdown, which takes place in extreme

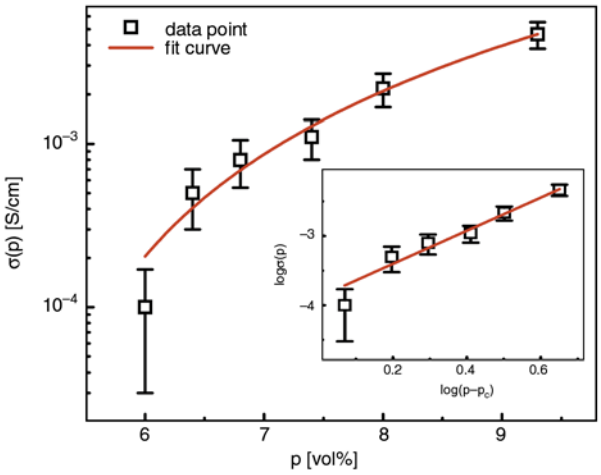

Figure 3. Static conductivity of the graphite/epoxy composites of various filler contents. The red solid lines are nonlinear fits to Equation (1). Ten samples were tested for each composite

conditions under the application of very large electric field. The avalanche breakdown is caused by an impact ionization that produces a large amount of charge carriers. This is often associated with a large current increment. To gain enough energy for ionizing the atoms, the electrons must move under a very strong electric field over a long distance. Avalanche breakdown usually refers to the permanent damage in insulators caused by a large electric field. Thus even the field strength decreases, the current still remains at a high level. In other words, the *J–E* curve is irreversible. In the present study, it is observed that the current density rises moderately with increasing field strength, and all the *J–E* curves are reversible (Figure 4). This excludes the possibility of avalanche breakdown. The second is the Zener breakdown, which involves the transitions of charge carriers between the valence and conduction band induced by appreciable electric fields [28]. It is also widely referred to as the interband tunneling, and commonly observed in semiconductor crystals [29], such as heavily doped *p–n* junctions [30]. As recognized, conventional tunneling involves the transition of charge carriers over an energy barrier. The Fowler-Nordheim tunneling is associated with the pulling of electrons from a conductor to vacuum by an intense electric field. Zener tunneling involves the pulling of electrons from the valence band to the conduction band of an insulator, thus rendering it conductive by producing movable charge carriers. It can be regarded as a special form of Fowler-Nordheim tunneling.

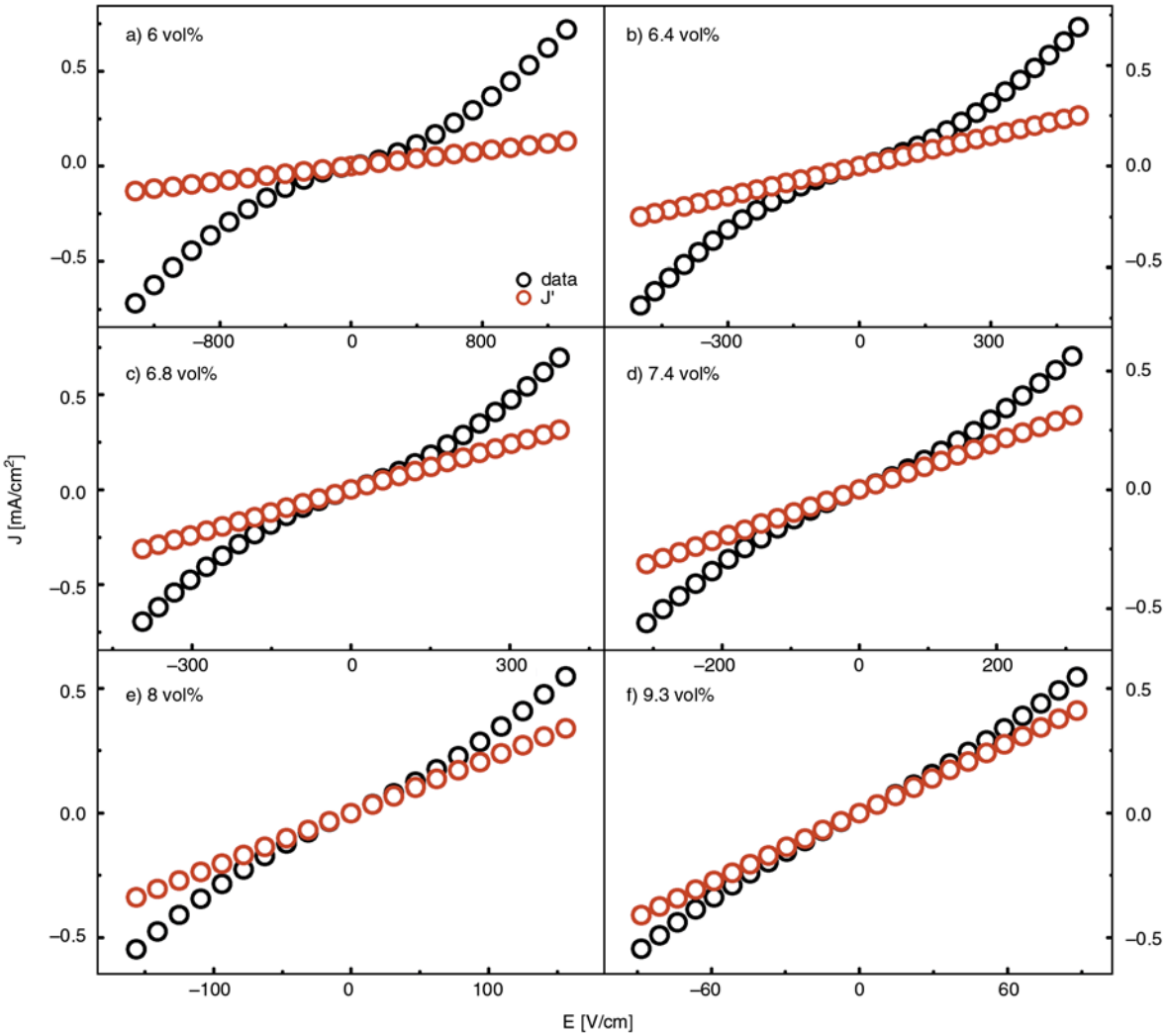

Figure 4. *J–E* characteristics of graphite/epoxy composites with various filler contents (a–f). The black open circles are experimental data; red open circles are linear current density *J′* deduced from $\sigma(p)E$.

Actually, the working principle of certain electronic devices is based on this mechanism [31, 32]. Since Zener breakdown is caused by the band-to-band tunneling, thus it would not disrupt the structure of material, i.e. the *J–E* characteristic is reversible. The current density caused by the Zener breakdown is given by Equation (2) [28]:

$$J(E) = AE^{n}\exp\left(-\frac{B}{E}\right) \tag{2}$$

where *A*, *B*, and *n* are constants; the value of *n* lies usually between 1 and 3, depending on various corrections or approximations included in the approach. A is related to the transition frequency, i.e. the number of attempts per second made by the charge carriers to cross the barrier. *B* is a measure of the energy barrier between the insulating matrix and the filler material. Thus the factor exp(–*B*/*E*) represents the transition probability of charge carriers between the conductive fillers and the matrix material. Although the reversible dielectric breakdown of the composites is caused by Zener tunneling as shown in Figure 4, the composite samples do not behave fully like a real Zener diode.

By separating linear $J''(\sigma(p)E)$ from the overall nonlinear current density, the remnant J'' (J–J') is obtained, as illustrated in Figure 6a. Figure 6b shows the $\ln(J''/E^{n})$ vs. $1/E$ plot for all composite samples. The apparent linear relationship provides strong support for the occurrence of Zener breakdown. To the best of our knowledge, no other physical models can fit the experimental results well. The fitting parameters were extracted and summarized in Table 1. The normalized $J-E$ relationship is shown in Figure 6c. Similar to the case of alternating current conductivity of the conductor/insulator system, the data points for different composite samples fall into one curve. Accordingly, Zener effect

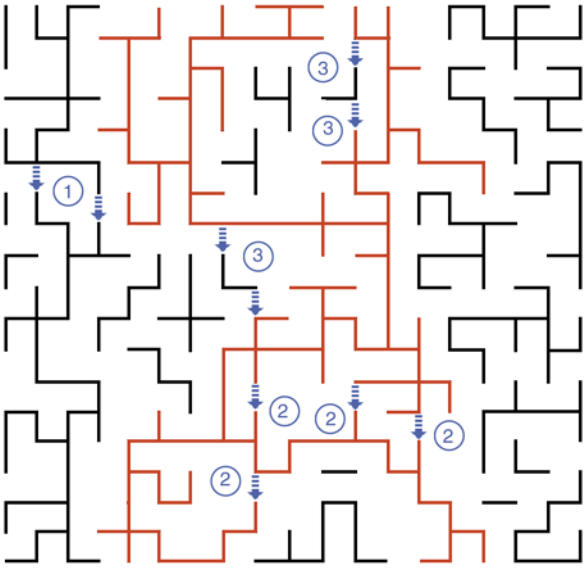

Figure 5. Two dimensional random-bond model of graphite/epoxy system above the percolation threshold. ①, ②, ③ and ③ correspond to the occurrence of dielectric breakdown between conducting clusters, between different parts of the conducting backbone, and between the clusters and the backbone, respectively.

Table 1. Parameters characterizing Zener current for the graphite/epoxy composites

p	n	lnA	B [V/cm]
6.0 vol%	1.75±0.02	–12.74±0.32	28.69±4.21
6.4 vol%	1.86±0.03	–12.34±0.30	17.23±3.15
6.8 vol%	1.85±0.03	–12.03±0.27	5.52±1.32
7.4 vol%	1.82±0.03	–11.86±0.26	4.08±1.02
8.0 vol%	1.84±0.03	–10.93±0.21	2.64±0.34
9.3 vol%	1.73±0.02	–9.43±0.15	8.89±1.73

reflects intrinsic properties of a certain conductor/insulator system.

For the composites with higher graphite concentration, a larger number of charge carriers are available, causing an increase of the transition frequency of charge carriers. This is manifested by larger A values. Therefore, A is not only related to the filler concentration but also to the filler dispersion. In addition, the internal insulating gaps tend to become smaller with increasing graphite concentration (see Figure 1), assuming that the graphite powders are dispersed uniformly in the polymer matrix. This leads to smaller B values with increasing filler content up to 8 vol%, favoring the occurrence of Zener breakdown. However, the B value rises sharply at 9.3 vol% graphite content. This is because the viscosity of liquid mixture during the composite processing is very large. In this case, pure stirring cannot effectively disperse graphite fillers homogeneously in the matrix material. This results in the formation of aggregates (see Figure 1f), thereby producing higher energy barrier for the charge carriers

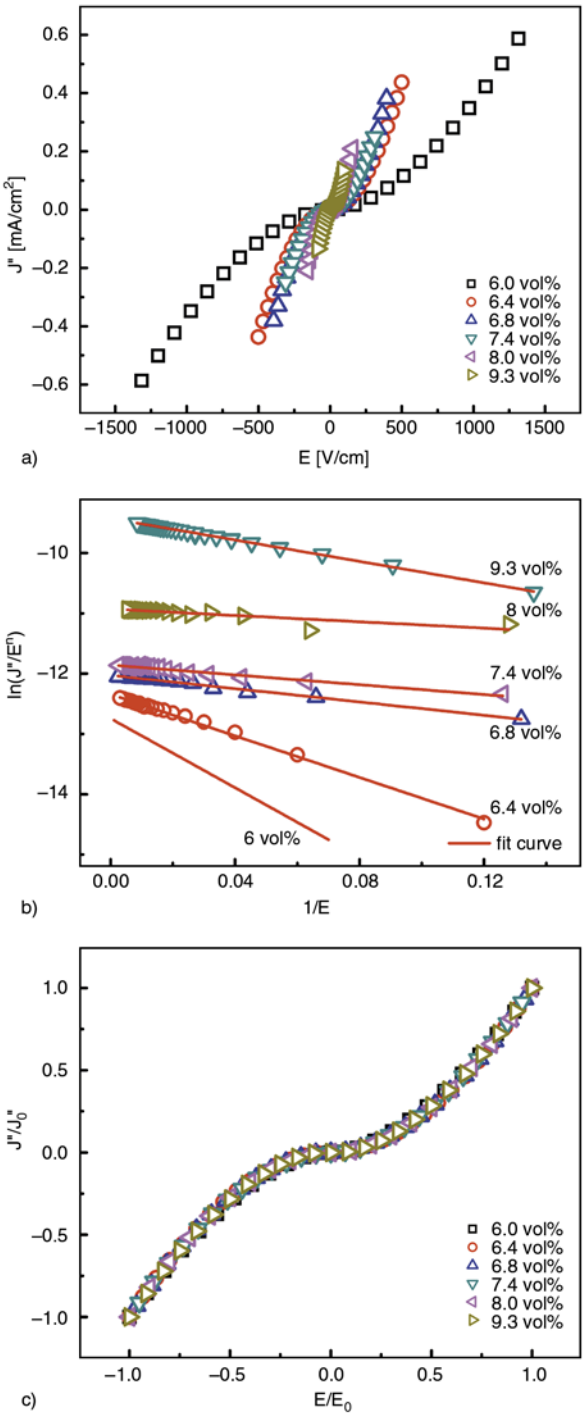

Figure 6. (a) Plot of J'' vs. E for graphite/epoxy composite samples with various filler contents. (b) Relationship between $\ln(J''/E^n)$ and $1/E$, where the linear fitting results are shown in red solid lines. n is evaluated from the data in (a). (c) Normalized relationship of J'' vs. E. J''_0 and E_0 are the maximum testing field strength and corresponding Zener current density as shown in (a).

to tunnel through. The aggregation also influences the static conductivity of the composites. However, the graphite/epoxy composites still exhibit percolative behavior as shown in Figure 3. Overall, Zener current tends to increase with filler content due to the presence of large amount of internal charge carriers.

As Zener breakdown relates to the band-to-band tunneling of charge carriers (from valence band to conduction band for electrons and vise versa for holes), the band gap and band tilt due to the external field are two main factors governing the generation of charge carriers, as illustrated in Figure 7. Obviously, a narrower band gap shortens the tunneling distance, facilitating interband tunneling. Similarly, a large electric field decreases the tunneling distance by tilting the band seriously. For the polymer composites, the width of the forbidden band is influenced by the nature of polymer matrix, while the internal field strength is determined by the dispersion of the conducting fillers. In order to suppress the Zener effect, the polymer matrix with a wide forbidden band is preferred (Figure 7b). Also, a poor dispersion of conductive fillers within the insulating matrix can also achieve the same results.

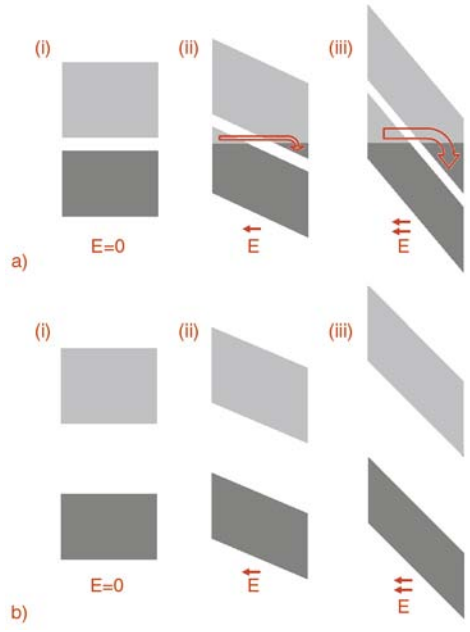

Figure 7. Transition of electrons from valence band to conduction band for insulating matrix with a (a) narrow and (b) wide forbidden band. (i), (ii), and (iii) illustrate the cases in which the insulating matrix subjected to no electric field, intermediate electric field, and large electric field, respectively.

4. Conclusions

In summary, nonlinear electrical transport is observed in the graphite/epoxy composites. The electrical nonlinearity is attributed to reversible dielectric breakdown inside the system. Such reversible breakdown is caused by the Zener effect, resulting from a magnified internal electric field imposed to thin insulating polymer layers. The experimental results provide strong support for the occurrence of Zener breakdown. The characteristics of Zener breakdown reveal certain important aspects relating to the electrical conduction within the composite system, such as the properties of the fillers, the dispersion of the fillers, and the nature of the polymer matrix.

Acknowledgements

This work is supported by a Strategic Grant (No. 7002772), City University of Hong Kong.

References

[1] Oh J-H., Oh K-S., Kim C-G., Hong C-S.: Design of radar absorbing structures using glass/epoxy composite containing carbon black in X-band frequency ranges. Composites Part B: Engineering, **35**, 49–56 (2004). DOI: 10.1016/j.compositesb.2003.08.011

[2] Arshak K., Morris D., Arshak A., Korostynska O.: Sensitivity of polyvinyl butyral/carbon-black sensors to pressure. Thin Solid Films, **516**, 3298–3304 (2008). DOI: 10.1016/j.tsf.2007.09.006

[3] Mrozek R. A., Cole P. J., Mondy L. A., Rao R. R., Bieg L. F., Lenhar J. L.: Highly conductive, melt processable polymer composites based on nickel and low melting eutectic metal. Polymer, **51**, 2954–2958 (2010). DOI: 10.1016/j.polymer.2010.04.067

[4] Psarras G. C.: Hopping conductivity in polymer matrix–metal particles composites. Composites Part A: Applied Science and Manufacturing, **37**, 1545–1553 (2006). DOI: 10.1016/j.compositesa.2005.11.004

[5] Dang Z-M., Yuan J-K., Zha J-W., Zhou T., Li S-T., Hu G-H.: Fundamentals, processes and applications of high-permittivity polymer–matrix composites. Progress in Materials Science, **57**, 660–723 (2012). DOI: 10.1016/j.pmatsci.2011.08.001

[6] Dang Z-M., Wang L., Yin Y., Zhang Q., Lei Q-Q.: Giant dielectric permittivities in functionalized carbon-nanotube/ electroactive-polymer nanocomposites. Advanced Materials, **19**, 852–857 (2007). DOI: 10.1002/adma.200600703

[7] Stauffer A. D.: Introduction to percolation theory. Taylor and Francis, London (2003).

[8] Dye J. C., Schrøder T. B.: Universality of ac conduction in disordered solids. Review of Modern Physics, **72**, 873–892 (2000). DOI: 10.1103/RevModPhys.72.873

[9] Lin H., Lu W., Chen G.: Nonlinear DC conduction behavior in epoxy resin/graphite nanosheets composites. Physica B: Condensed Matter, **400**, 229–236 (2007). DOI: 10.1016/j.physb.2007.07.015

[10] Chen G., Weng W., Wu D., Wu C.: Nonlinear conduction in nylon-6/foliated graphite nanocomposites above the percolation threshold. Journal of Polymer Science Part B: Polymer Physics, **42**, 155–167 (2004). DOI: 10.1002/polb.10682

[11] Zheng Q., Song Y., Wu G., Yi X.: Reversible nonlinear conduction behavior for high-density polyethylene/graphite powder composites near the percolation threshold. Journal of Polymer Science Part B: Polymer Physics, **39**, 2833–2842 (2001). DOI: 10.1002/polb.10042

[12] Celzard A., Furdin G., Marêché J. F., McRae E.: Nonlinear current-voltage characteristics in anisotropic epoxy resin-graphite flake composites. Journal of Materials Science, **32**, 1849–1853 (1997). DOI: 10.1023/A:1018504906935

[13] Alam M. A., Weir B. E., Silverman P. J.: A study of soft and hard breakdown – Part I: Analysis of statistical percolation conductance. IEEE Transactions on Electron Devices, **49**, 232–238 (2002). DOI: 10.1109/16.981212

[14] Kim J., Grzybowski B. A.: Controlling reversible dielectric breakdown in metal/polymer nanocomposites. Advanced Materials, **24**, 1850–1855 (2012). DOI: 10.1002/adma.201104334

[15] Zhou L., Lin J., Chen G.: Electrical breakdown in high-density polyethylene/graphite nanosheets conductive composites. Journal of Polymer Science Part B: Polymer Physics, **47**, 576–582 (2009). DOI: 10.1002/polb.21663

[16] Song Y., Shen Y., Liu H., Lin Y., Li M., Nan C-Y.: Improving the dielectric constants and breakdown strength of polymer composites: Effects of the shape of the $BaTiO_3$ nanoinclusions, surface modification and polymer matrix. Journal of Materials Chemistry, **22**, 16491–16498 (2012). DOI: 10.1039/C2JM32579A

[17] Schuman T. P., Siddabattuni S., Cox O., Dogan F.: Improved dielectric breakdown strength of covalently-bonded interface polymer–particle nanocomposites. Composite Interfaces, **17**, 719–731 (2010). DOI: 10.1163/092764410X495315

[18] Sen A. K.: Nonlinear response, semi-classical percolation and breakdown in the RRTN Mode l. in 'Lecture notes in physics: Quantum and semi-classical percolation and breakdown in disordered solids' (eds.: Chakrabarti B. K., Bardhan K. K., Sen A. K.) Springer, Heildelberg, Vol 762, 1–62 (2009).

[19] Gupta A. K., Sen A. K.: Nonlinear dc response in composites: A percolative study. Physical Review B, **57**, 3375–3388 (1998). DOI: 10.1103/PhysRevB.57.3375

[20] He L. X., Tjong S-C.: Universality of Zener tunneling in carbon/polymer composites. Synthetic Metals, **161**, 2647–2650 (2012). DOI: 10.1016/j.synthmet.2011.09.037

[21] Song Y. S., Youn J. R.: Influence of dispersion states of carbon nanotubes on physical properties of epoxy nanocomposites. Carbon, **43**, 1378–1385 (2005). DOI: 10.1016/j.carbon.2005.01.007

[22] Balberg I.: A comprehensive picture of the electrical phenomena in carbon black–polymer composites. Carbon, **40**, 139–143 (2002). DOI: 10.1016/S0008-6223(01)00164-6

[23] Ezquerra T. A., Kulescza M., Cruz C. S., Baltá-Calleja F. J.: Charge transport in polyethylene–graphite composite materials. Advanced Materials, **2**, 597–600 (1990). DOI: 10.1002/adma.19900021209

[24] Mamunya Y. P., Muzychenko Y. V., Pissis P., Lebedev E. V., Shut M. I.: Percolation phenomena in polymers containing dispersed iron. Polymer Engineering and Science, **42**, 90–100 (2002). DOI: 10.1002/pen.10930

[25] Logakis E., Pandis Ch., Peoglos V., Pissis P., Pionteck J., Pötschke P., Mičušík M., Omastová M.: Electrical/dielectric properties and conduction mechanism in melt processed polyamide/multi-walled carbon nanotubes composites. Polymer, **50**, 5103–5111 (2009) DOI: 10.1016/j.polymer.2009.08.038

[26] Gefen Y., Shih W-H., Laibowitz R. B., Viggiano J. M.: Nonlinear behavior near the percolation metal-insulator transition. Physical Review Letters, **57**, 3097–3100 (1986). DOI: 10.1103/PhysRevLett.57.3097

[27] Sheng P., Sichel E. K., Gittleman J. I.: Fluctuation-induced tunneling conduction in carbon-polyvinylchloride composites. Physical Review Letters, **40**, 1197–1200 (1978). DOI: 10.1103/PhysRevLett.40.1197

[28] Zener C.: A theory of the electrical breakdown of solid dielectrics. Proceedings of Royal Society A, **145**, 523–539 (1934). DOI: 10.1098/rspa.1934.0116

[29] Chynoweth A. G.: Progress in semiconductors. John Wiley and Sons, New York (1960).

[30] McAfee K. B., Ryder E. J., Shockley W., Sparks M.: Observations of Zener current in germanium p-n junctions. Physical Review, **83**, 650–651 (1951). DOI: 10.1103/PhysRev.83.650

[31] Kleemann H., Gutierrez R., Lindner F., Avdoshenko S., Manrique P. D., Lüssem B., Cuniberti G., Leo K.: Organic Zener diodes: Tunneling across the gap in organic semiconductor materials. Nano Letters, **10**, 4929–4934 (2010). DOI: 10.1021/nl102916n

[32] Reddick W. M., Amaratunga G. A. J.: Silicon surface tunnel transistor. Applied Physics Letters, **67**, 494–496 (1995). DOI: 10.1063/1.114547

eXPRESS Polymer Letters Vol.7, No.4 (2013) 383–395
Available online at www.expresspolymlett.com
DOI: 10.3144/expresspolymlett.2013.35

Stochastic analysis of inter- and intra-laminar damage in notched PEEK laminates

*M. Naderi, M. M. Khonsari**

Department of Mechanical Engineering, Louisiana State University, LA 70803 Baton Rouge, USA

Received 21 October 2012; accepted in revised form 13 January 2013

Abstract. This paper presents a finite element model to predict the progressive damage mechanisms in open-hole PEEK (Poly-Ether-Ether-Ketone) laminates. The stochastic laminate's properties with non-uniform stress distribution are considered from element to element using the Gaussian distribution function. The failure modes considered are: fiber tension/compression, matrix tension/compression, fiber/matrix shear, and delamination damage. The onset of damage initiation and propagation are predicted and compared with three different failure criteria: strain-based damage criterion, Hashin-based degradation approach and stress-based damage criterion which is proposed by the authors of the present work. The inter-laminar damage modes associated with fiber/matrix shearing and delamination are modeled using the cohesive elements technique in ABAQUS™ with fracture energy evolution law. Mesh sensitivity and the effect of various viscous regularization factors are investigated. Damage propagation and failure path are examined by re-running the program for several times.

Keywords: *polymer composites, modeling and simulation, damage mechanism, cohesive element, stochastic material properties*

1. Introduction

Fiber reinforced thermoplastic composite laminates are in high demand in advanced aerospace structures owing to their light weight, high stiffness, high strength, good toughness, long durability, superior impact resistance and favorable damage-tolerance properties. Yet, despite many advantages compared to their metal counterparts, these laminates are not exempt from deterioration and damage, especially in the presence of a stress concentration. Of particular interest here is to study a common type of thermoplastic composite known as AS4/PEEK laminate composed of poly-ether-ether-ketone (PEEK) reinforced by AS4 carbon fiber. We seek to predict the strength of this type of laminate in the presence of stress concentration in the form of a hole or a notch in pinned- and bolt-joints. This information is useful at the design stage.

It is appropriate to begin with a brief survey of the open literature since numerous investigations dedicated to the prediction of progressive damage and strength of the laminates with stress concentrations already exist. For example, Chang *et al*. [1] studied the progressive damage for T300/976 graphite epoxy containing a hole under tensile loading using the modified Hashin [2] failure criteria. Their approach was to reduce the material properties to zero when failure criteria is satisfied by implementing the so-called '*sudden degradation rule*'. Lessard and Shokrieh [3] modified Hashin failure criteria by taking into account the non-linear characteristic of material as well as implementing the sudden material degradation rule. Dano *et al*. [4] investigated the bearing strength of glass/epoxy pinned-joint laminates using the commercial software ABAQUS™. Later, Icten and Karakuzu [5] investigated different

*Corresponding author, e-mail: khonsari@me.lsu.edu

failure modes and bearing strength in woven carbon/epoxy laminates using the failure criteria proposed by Hoffman [6] and Hashin [2] both numerically and experimentally. Maa and Cheng [7] developed a failure model using the continuum damage mechanics (CDM)-based failure model using elastic-plastic constitutive equations implemented in ABAQUS. Also reported was their experimental data for AS4/PEEK laminates containing a circular hole. In a similar way, Ding *et al*. [8] carried out a three-dimensional finite element analysis of an open-hole thermoplastic AS4/PEEK laminate to interpret the results of their experimental observations.

To consider delamination and inter-laminar damage, Lapczyk and Hurtado [9] developed an anisotropic damage model for predicting failure and post-failure behavior in fiber reinforced materials based on the concept of fracture energy dissipation. They addressed the convergence of the numerical model in the softening regime by introducing a viscous regularization factor in the computations. Recently, Falzon and Apruzzese [10] carried out a three-dimensional CDM-based model in ABAQUS/Explicit to simulate the intra-laminar degradation of fiber-reinforced laminates based on ply failure mechanisms. Their focus was on the non-linear response of the shear failure mode and the interaction with other failure modes.

Recent literature in mechanic-based understanding and modeling of progressive damage analysis and prediction of strength of composite laminates specially notched laminates in composite research community contains many noteworthy studies such as the works reported by Camanho *et al*. [11], Abisset *et al*. [12], van der Meer *et al*. [13] and Fang *et al*. [14], Daghia and Ladeveze [15]. Among them, Camanho *et al*. [11] examined a continuum damage model to predict the strength and size effects of notched carbon–epoxy laminates. They experimentally and analytically studied the effects of size and the development of a fracture process zone before final failure. Abisset *et al*. [12] investigated progressive degradation in an open-hole IM7/8552 carbon/epoxy laminate using a damage mesomodel developed based on a micromechanical approach. They compared experimental and numerical results considering the ply's thickness and the in-plane scaling effect to capture the change in failure mode and the effect of the specimen's scale on tensile strength. Van der Meer *et al*. [13] simulated progressive failure, matrix cracking, interface elements for delamination, and a continuum damage model for fiber failure using phantom-node computational method. They validated their computational framework against experimental observations for open-hole tests and compact tension tests. Fang *et al*. [14] presented a new augmented finite element method (A-FEM) which can account for arbitrary crack path, and different intra-element discontinuities. They showed that within their new formulation one is able to derive an explicit and fully condensed elemental equilibrium equations using augmented elements without additional external nodes or degree of freedom.

A survey of the published works clearly reveals that while substantial progress has been made especially in computational simulation of composites failure, predicting their progressive failure and arbitrary crack path considering randomness in material properties distribution remain a challenging task due to the complexity of the interactions among multiple damage processes. While some computational methods, i.e. phantom-node method [16], extended-finite element method (X-FEM) [17] and augmented-finite element method (A-FEM) [18, 19] to simulate progressive arbitrary failure in composite materials can yield more accurate results than numerical methods considering reducing the material properties to zero at the time of failure and turning the element's load carrying capacity off, the objective of the present work is to investigate the progressive degradation, delamination behavior, and strength of an open-hole AS4/PEEK laminate with the stochastic distribution of material properties using a three-dimensional numerical simulation. The cohesive elements technique proposed by Camanho and Dávila [20] are considered between two adjacent layers to model the failure due to delamination. The progressive intra-laminar damage model based on the sudden degradation rule is compared to the other approaches with strain-based continuum damage formulation proposed by Linde *et al*. [21]. The procedure of the progressive inter- and intra-laminar damage evolution is implemented in commercial software ABAQUS™ [22] using programming in UMAT (user-defined material) subroutine.

2. Progressive damage models

In order to establish a progressive damage analysis, a set of failure criteria and material property degradation rules are required. The failure criteria must properly take into account the damage mechanisms such as fiber breakage, matrix cracking, fiber/matrix shearing and delamination. In the following sections, different failure methods used in the current work are explained in details. Two methods (Method I and Method II) are according to the strain and stress-based continuum damage mechanics formulation. These methods consider the gradual material property degradation controlled by the individual fracture energies in both the fiber and the matrix. The onset of damage initiation in Method II is based on the Hashin failure criteria while the one in Method I is based on an exponential damage initiation law (a strain-based evolution approach) developed by Linde *et al*. [21]. However, the damage evolution in Method II is stress-based and incorporates a modification of Method I proposed by the authors of the present work. The third method (Method III) is based on Hashin failure criteria [2] and takes into account the effect of sudden material degradation rule. Inter-laminar damage or delamination in Methods I and II are according to cohesive zone technique while Method III uses the Hashin failure criteria. The details of these methods are described in the following sections.

2.1. Method I

2.1.1. Intra-laminar damage model

The failure criteria of Method I is a strain-based continuum damage formulation with different failure criteria for matrix and fiber [21]. It takes into account the gradual degradation of the material controlled by the individual fracture energies of matrix and fiber. Matrix failure initiates if the failure index, *MF*, defined below in Equation (1), exceeds the transverse tensile failure strain, ε_T^t:

$$MF^2 = \left[\frac{\varepsilon_T^t}{\varepsilon_T^c}(\varepsilon_{22})^2 + \left(\varepsilon_T^t - \frac{(\varepsilon_{22})^2}{\varepsilon_T^c}\right)\varepsilon_{22} + \left(\frac{\varepsilon_T^t}{\varepsilon_s}\right)^2(\varepsilon_{12})^2\right] > (\varepsilon_T^t)^2 \tag{1}$$

where ε_T^c and ε_s represent the transverse compressive failure strain and the shear failure strain, respectively. ε_{22} and ε_{12} are the strain components perpendicular to fiber direction and shear direction, respectively. The matrix failure strains can be obtained from the following expressions shown as Equation (2):

$$\varepsilon_T^t = \frac{Y_t}{E_{22}}; \quad \varepsilon_T^c = \frac{Y_c}{E_{22}}; \quad \varepsilon_s = \frac{S_{12}}{E_{12}} \tag{2}$$

where E_{22} and E_{12} are the undamaged laminate's transverse and shear stiffness, respectively. Y_t and Y_c represent transverse tensile and compressive failure strength, respectively. The shear failure strength is S_{12}.

Damage evolution variable, d_m, is a function of the strain at failure, undamaged material stiffness, and the current value of the failure initiation variable. Also considered in the damage variable calculations are the fiber and matrix fracture energies (G_f and G_m) and the element characteristic length (L_c) to reduce the mesh sensitivity of the numerical model. The matrix damage, d_m, takes place in the direction perpendicular to the fibers, and the fiber damage, d_f, occurs in the direction parallel to the fibers. The matrix damage evolution parameter, d_m, is calculated by Equation (3) [21]:

$$d_m = 1 - \frac{\varepsilon_T^t}{MF} e^{[C_{22}\varepsilon_T^t(MF-\varepsilon_T^t)L_c/G_m]} \tag{3}$$

where C_{22} is the stiffness matrix component in the direction perpendicular to that of the fibers.

The fiber failure, *FF*, initiates if the following criterion defined by Equation (4) [21]:

$$FF^2 = \left[\frac{\varepsilon_L^t}{\varepsilon_L^c}(\varepsilon_{11})^2 + \left(\varepsilon_L^t - \frac{(\varepsilon_{11})^2}{\varepsilon_L^c}\right)\varepsilon_{11}\right] > (\varepsilon_L^t)^2 \tag{4}$$

where ε_L^c and ε_L^c are longitudinal tensile and compressive failure strain, respectively and ε_{11} is the longitudinal strain component.

The fiber failure strains can be obtained from Equation (5):

$$\varepsilon_L^t = \frac{X_t}{E_{11}}, \quad \varepsilon_L^c = \frac{X_c}{E_{11}} \tag{5}$$

where E_{11} is the initial laminate's longitudinal stiffness. X_t and X_c represent longitudinal tensile and compressive failure strength, respectively.

Once Equation (4) is satisfied, the fiber damage parameter d_f evolves as shown in Equation (6) [21]:

$$d_f = 1 - \frac{\varepsilon_L^t}{FF} e^{[C_{11}\varepsilon_L^t(FF-\varepsilon_L^t)L_c/G_f]} \tag{6}$$

where C_{11} is the component of stiffness matrix.

Once damage initiates in the laminate, the laminates' stiffness degrades. Considering fiber and matrix damage evolution and transverse isotropy, the laminate's stiffness matrix is written as shown by Equation (7) [21]:

$$C_{\mathrm{d}}=\begin{bmatrix} (1-d_{\mathrm{f}})C_{11} & (1-d_{\mathrm{f}})(1-d_{\mathrm{m}})C_{12} & (1-d_{\mathrm{f}})C_{13} & 0 & 0 & 0 \\ & (1-d_{\mathrm{m}})C_{22} & (1-d_{\mathrm{f}})(1-d_{\mathrm{m}})C_{23} & 0 & 0 & 0 \\ & & C_{33} & 0 & 0 & 0 \\ & & & (1-d_{\mathrm{m}})(1-d_{\mathrm{m}})C_{44} & 0 & 0 \\ & & & & C_{55} & 0 \\ \textit{symmetry} & & & & & C_{66} \end{bmatrix} \tag{7}$$

where

$$C_{11}=\frac{1-\nu_{23}^2}{E_{22}E_{33}\Delta};\quad C_{22}=\frac{1-\nu_{13}\nu_{31}}{E_{22}E_{11}\Delta};\quad C_{33}=C_{22};$$

$$C_{12}=\frac{\nu_{12}+\nu_{32}\nu_{13}}{E_{22}E_{11}\Delta};\quad C_{13}=\frac{\nu_{13}+\nu_{23}\nu_{12}}{E_{22}E_{11}\Delta};$$

$$C_{23}=\frac{\nu_{23}+\nu_{21}\nu_{13}}{E_{22}E_{11}\Delta};\quad C_{44}=E_{23};\quad C_{55}=E_{13};$$

$$C_{66}=E_{12};\quad \Delta=\frac{1-\nu_{23}^2-\nu_{13}\nu_{31}-2\nu_{21}\nu_{32}\nu_{13}}{E_{11}E_{22}E_{33}}$$

where υ_{ij} $(i, j = 1, 2, 3)$ is the Poisson ratio.
The damage growth reduces the stiffness and consequently the stress tends to redistribute in each element of the material.

2.1.2. Inter-laminar damage (delamination) model

Inter-laminar damage is simulated by placing cohesive elements between two adjacent layers. The constitutive response of the cohesive elements is described by a linear traction-separation law as presented in Figure 1. Figure 1 shows the schematic of material response in normal, shear and mixed mode loading. The triangles in the two vertical coordinate planes ($(\sigma, \delta_{\mathrm{I}})$ and $(\sigma, \delta_{\mathrm{Shear}})$ planes) represent the response under pure normal and pure shear deformation, respectively. The intermediate vertical plane ($(\sigma, \delta_{\mathrm{m}})$ plane) represents the damage response under mixed mode condition. This figure shows that the material response is linear until it reaches a peak value of stress after which it softens linearly in the post-peak region. The initiation under different modes of pure normal (δ_{I}^0), pure shear ($\delta_{\mathrm{Shear}}^0$) and mixed mode loading (δ_{m}^0) occurs when the inter-laminar stress reaches the inter-laminar pure normal strength (σ_{I}), pure shear strength (σ_{Shear}), or mixed mode strength (σ_{m}) depending on the mode of the loading. The growth regime represents the softening and separation behavior of the degraded material's element. The material's element is completely delaminated once the area under traction-displacement (Figure 1) reaches the fracture energy, G_{c}, and the failure displacement, $\sigma_{\mathrm{m}}^{\mathrm{f}}$, is reached. The cohesive elements and their constitutive responses are programmed in ABAQUS™ for the prediction of delamination initiation and propagation. A high initial stiffness (the so-called penalty stiffness; K_{p}) is defined to avoid de-cohesion of two surfaces in the linear elastic range.

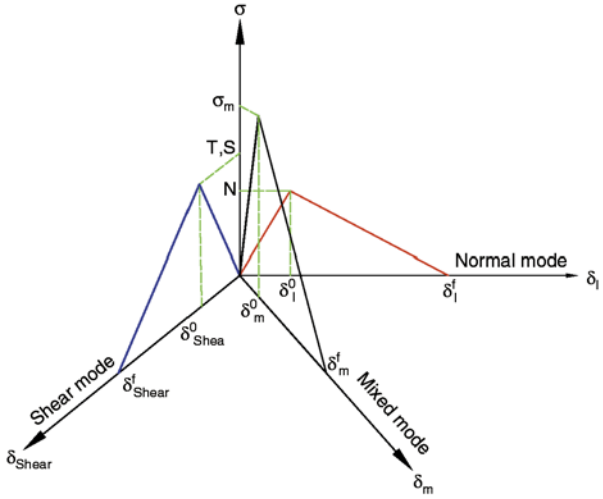

Figure 1. Schematic of bilinear constitutive behavior of cohesive zone for different modes of failure

Delamination initiation:
The onset of delamination initiation is determined based on a quadratic nominal strain criterion [22]. The strength of the adhesive in the normal and shear directions are used as input data, as shown by Equation (8):

$$\left(\frac{\varepsilon_n}{\varepsilon_n^f}\right)^2 + \left(\frac{\varepsilon_s}{\varepsilon_s^f}\right)^2 + \left(\frac{\varepsilon_t}{\varepsilon_s^f}\right)^2 > 1 \text{ with } \quad \varepsilon_n^f = \frac{N}{K_p};$$

$$\varepsilon_s^f = \frac{S}{K_p} = \frac{T}{K_p} \tag{8}$$

where ε_n^f, ε_s^f are inter-laminar tensile and shear strain. ε_s is tensile strain component, ε_s and ε_t are shear strain component. Parameter N is the inter-laminar tensile strength; S and T represent the inter-laminar shear strength. It is noted that for convenience, we considered a constitutive thickness of 1.0 mm such that there is no need to distinguish between the nominal strain and the separation displacement in the above equation.

Delamination growth:

The damage evolution or delamination propagation law postulates that the material stiffness is degraded once the corresponding initiation criterion is met. The damage propagation prediction is usually studied in terms of energy release rate and fracture toughness. Mixed-mode delamination growth is predicted when mixed mode fracture energy (G_T) is greater than critical fracture energy (G_C). Several laws implemented in FEM codes have been considered to compute the fracture toughness for mixed-mode failure, such as Benzeggagh-Kenane (B-K) criterion [23] the power law criterion [24], and the Reeder criterion [25]. Demonstration of applications of B-K criterion can be found in the work of Camanho *et al*. [26] for PEEK and epoxy composites. In this study, the 'power law criterion' proposed by Benzeggagh-Kenane – the so-called B-K criterion – [23] is used. This criterion is established in terms of an interaction between the energy release rates to predict the delamination evolution as shown by Equation (9):

$$G_{Ic} + (G_{IIc} - G_{Ic})\left(\frac{G_{II} + G_{III}}{G_T}\right)^{\eta} = G_c, \text{ with}$$

$$T = G_I + G_{II} + G_{III} \tag{9}$$

where η is a material parameter and G_{Ic} and G_{IIc} are the fracture energies of Mode I and II at failure, respectively. G_c is critical fracture energy. G_I, G_{II} and G_{III} are fracture energies of Mode I, II, and III.

2.2. Method II

Method II is the modified of Method I and is a stress-based continuum damage formulation with the fiber and matrix failure proposed by the present authors. The main difference between Methods I and II is in the definition of matrix and fiber failure indices (*MF* and *FF*) in which the former uses the strain-based approach and the latter II uses the stress-based approach. Damage initiation is based on the Hashin failure criteria summarized in Table 1.

As summarized in Table 1, seven sets of initiation criteria are considered. For detecting fiber, matrix and delamination some indices are defined, i.e., *MF* for matrix failure in either tension or compression, *FF* for fiber failure in either tension or compression, *DELT* delamination failure in tension and *DELC* for delamination failure in compression. Once each of the indices reaches the unit value, failure is initiated and softening process in the material begins.

The matrix damage evolution parameter d_m is the modified version of Equation (3) and based on stress approach described by Equation (10) (Please see Section 2.1. for more details):

$$d_m = 1 - \frac{Y_t}{E_{22}MF} e^{\left[Y_t\left(MF - \frac{Y_t}{\varepsilon_{22}}\right)L_c/G_m\right]} \tag{10}$$

The fiber damage evolution d_f is obtained using Equation (11):

$$d_f = 1 - \frac{X_t}{E_{11}FF} e^{\left[X_t\left(FF - \frac{X_t}{E_{11}}\right)L_c/G_f\right]} \tag{11}$$

The procedure for evaluation of delamination or inter-laminar damage is the same as the delamination method described in Section 2.1.2. (Please see Section 2.1 for more details).

2.3. Method III

Method III uses the Hashin failure criteria as summarized in Table 1. This method is used for identifying matrix tensile/compressive cracking, fiber tensile/compressive breakage, fiber/matrix shear failure, and tension/compression delamination. If failure criterion is satisfied in an element, the material properties of that failed element is changed by a set of material properties in accordance with the sudden degradation rule. Corresponding to the type of the failure, the laminate response against the load is changed in the case of the damage. The sudden stiff-

Table 1. Hashin failure criteria and material degradation rules [2, 3, 15]

Failure mode	Failure index	Failure approach	Material degradation rule (for Method III)
Matrix tensile failure ($\sigma_{22}>0$)	$MF^2=\left(\frac{\sigma_{22}}{Y_t}\right)^2+\left(\frac{\sigma_{12}}{S_{12}}\right)^2+\left(\frac{\sigma_{23}}{S_{23}}\right)^2>1$	Method II and III	$E_{22}\rightarrow 0.2E_{22}$, $E_{12}\rightarrow 0.2E_{12}$, $E_{23}\rightarrow 0.2E_{23}$
Matrix compression failure ($\sigma_{22}<0$)	$MF^2=\left(\frac{\sigma_{22}}{Y_c}\right)^2+\left(\frac{\sigma_{12}}{S_{12}}\right)^2+\left(\frac{\sigma_{23}}{S_{23}}\right)^2>1$	Method II and III	$E_{22}\rightarrow 0.4E_{22}$, $E_{12}\rightarrow 0.4E_{12}$, $E_{23}\rightarrow 0.4E_{23}$
Fiber tensile failure ($\sigma_{11}>0$)	$FF^2=\left(\frac{\sigma_{11}}{X_t}\right)^2+\left(\frac{\sigma_{12}}{S_{12}}\right)^2+\left(\frac{\sigma_{13}}{S_{13}}\right)^2>1$	Method II and III	$E_{11}\rightarrow 0.07E_{11}$
Fiber compression failure ($\sigma_{11}<0$)	$FF^2=\left(\frac{\sigma_{11}}{X_c}\right)^2>1$	Method II and III	$E_{11}\rightarrow 0.14E_{11}$
Fiber/matrix shear failure	$FF^2=\left(\frac{\sigma_{11}}{X_c}\right)^2+\left(\frac{\sigma_{12}}{S_{12}}\right)^2+\left(\frac{\sigma_{13}}{S_{13}}\right)^2>1$	Method III	$E_{11}\rightarrow 0$
Inter-laminar tensile failure ($\sigma_{33}>0$)	$DELT^2=\left(\frac{\sigma_{33}}{Z_t}\right)^2+\left(\frac{\sigma_{13}}{S_{13}}\right)^2+\left(\frac{\sigma_{23}}{S_{23}}\right)^2>1$	Method III	$E_{33}, E_{23}, E_{13}, \rightarrow 0$
Inter-laminar compression failure ($\sigma_{33}>0$)	$DELC^2=\left(\frac{\sigma_{33}}{Z_c}\right)^2+\left(\frac{\sigma_{13}}{S_{13}}\right)^2+\left(\frac{\sigma_{23}}{S_{23}}\right)^2>1$	Method III	$E_{33}, E_{23}, E_{13}, \rightarrow 0$

ness degradation of the failed element in the matrix and fibers is different. For example, once the matrix fails in tension, the transverse stiffness, E_{22}, drops to $0.2E_{22}$ while at the onset of the fiber failure the longitudinal stiffness, E_{11}, reduces to $0.07E_{11}$. Therefore, in the current work, the material degradation rules are based on the work of [27, 28] for matrix tensile/compressive failure and for fiber tensile/compressive failure (See Table 1). Note that fiber/matrix shear and delamination failure were not considered in the work of [27, 28] and therefore material property is reduced to a small value for these damage modes.

3. Model development

To perform stress and progressive damage analysis based on Methods I, II, III, a three-dimensional finite element model is created in ABAQUS™ [22]. One end of the laminate is clamped in x, y, and z and the other end is subjected to the uniform displacement of v (Figure 2a). ABAQUS 6-node linear triangular prism (C3D6) is defined to mesh the composite laminate such that each ply has one element through the thickness direction. ABAQUS 6-node, three-dimensional cohesive element (COH3D6) is defined to mesh the cohesive layers with 0.001 mm thickness. Two types of laminates configuration are considered in the model. The first one is $[0/60/-45/+45]_{3s}$ described in details in Section 5. The second one is $[0/45/90/-45]_{2s}$ for which experimental data and numerical results are available in [7]. The latter is chosen to verify the results of the presented simulation; See Table 2. In each case, because of the symmetry condition, only one quarter of the specimen is modeled. That is, the model is in the shape of the specimen is cut in half in XZ plane and then cut in half in YZ plane. Boundary conditions are shown in Figure 2a.

Table 2. Mesh specifications of the model

	Number of elements	Average aspect ratio
Mesh 1	8 937	2.45
Mesh 2	24 854	1.7
Mesh 3	54 374	1.4

3.1. Stochastic material properties distribution

The laminate's stiffness and strength are generated using the Gaussian distribution function with around ±1% of variation to consider spatial stochastic properties in the model. A typical Gaussian distribution of the AS4/PEEK longitudinal stiffness is shown in Figure 2b. Gaussian distribution function is defined in user-subroutine SDVINI in ABAQUS which enables the user to specify the initial solution-dependent state variables with stochastic material properties.

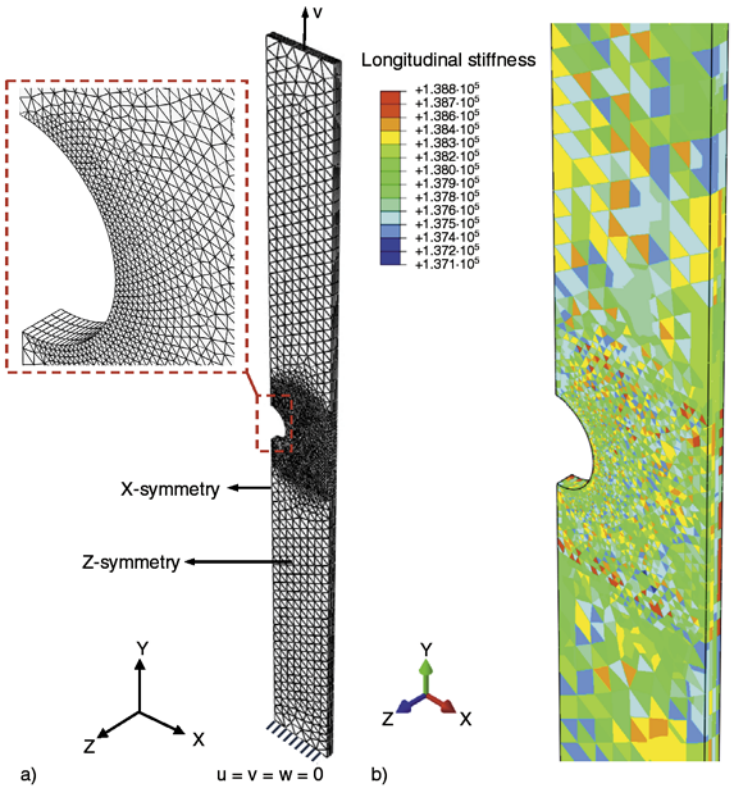

Figure 2. (a) 3D Finite element mesh and boundary conditions, (b) Gaussian distribution of longitudinal stiffness

3.2. Numerical procedure

The progressive damage model is implemented in ABAQUS™ through the user-defined subroutine UMAT to describe the specific material characteristics. This subroutine is called to determine the material properties at each point. The stresses and solution-dependent state variables are updated at the end of each iteration and the Jacobian matrix is recalculated accordingly. The simulation starts with the model preparation as presented in the flowchart of the procedure; See Figure 3. Then, a Gaussian distribution for the laminate properties is applied to all the elements. Stress analysis is then performed based on the applied displacement followed by the failure analysis. The values of the failure indexes are stored as the solution-dependent state variables. If the damage initiation criterion is satisfied, damage evolution laws are applied for Methods I and II. In Method III, if the damage initiation criterion is met, the material properties are treated according to the sudden material degradation rule. If there is no failure, an incremental displacement, δv, is added to the last displacement amplitude, v_i. Next, a new Jacobian is computed, the stress is redistributed accordingly, and the calculations are repeated. The failure occurs when the laminate cannot tolerate any more load increment. Physically, this represents a large deflection and excessive damage at which point the program is terminated. Program is stopped at this stage and simulation cannot pass any new increment. It is noted that the case in which there is no failure does not have any inconsistency with equilibrium solution and new increment successfully run.

4. Sensitivity analysis parameters

Sensitivity studies are performed to examine the influence of various parameters on the load-displacement curves of the progressive damage models. The parameters of particular interest pertain to mesh density and viscous regularization (μ).

Mesh dependency:

The problem of strain localization induced by damage localization is treated by a method that minimizes the mesh dependency in the numerical results. This is done by using the fracture energy-based damage evolution and considering the characteristic length of the element into the damage evolution law. The calculation of the characteristic length without considering the crack direction depends on the element geometry and formulations. Hence, the problem of mesh dependency still exists [13]. In order to minimize the problem of mesh dependency, elements' aspect ratio (the ratio of shortest edge to the

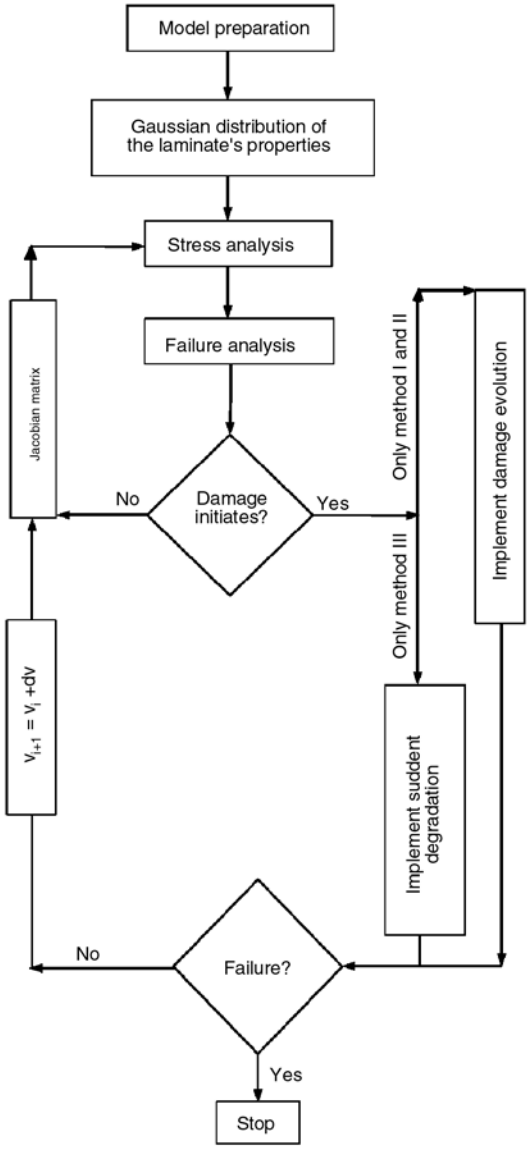

Figure 3. Damage flowchart implemented in ABAQUS™

longest edge of an element) should be close to one. The results of three different mesh refinements are summarized in Table 2.

Viscous regularization factor (μ):

Material models that exhibits softening behavior and stiffness degradation often tend to have severe convergence difficulties. A common technique to alleviate the associated convergence difficulties is to implement the so-called viscous regularization factor which through the introduction of a viscosity term in the damage evolution of Equations (10) and (11) forces the tangent stiffness matrix of the softening material to be positive definite for adequately small time increments [9, 22]. It is important to check that the energy associated with viscous regularization is small compared to the overall strain energy. The time evolution equation of viscous damage variable is as defined by Equations (12) and (13) [9, 22]:

$$\dot{d}_{\mathrm{m}}^{\mathrm{v}} = \frac{1}{\mu}(d_{\mathrm{m}} - d_{\mathrm{m}}^{\mathrm{v}}) \tag{12}$$

$$\dot{d}_{\mathrm{f}}^{\mathrm{v}} = \frac{1}{\mu}(d_{\mathrm{f}} - d_{\mathrm{f}}^{\mathrm{v}}) \tag{13}$$

where $d_{\mathrm{m}}^{\mathrm{v}}$ and $d_{\mathrm{f}}^{\mathrm{v}}$ are the regularized matrix and fiber damage variables used in the calculation of damage stiffness matrix and Jacobian matrix, respectively.

5. Material and experiment

The material of the present work is an AS4/PEEK quasi-isotropic laminate $[0/90/–45/+45]_{3s}$ with polyether-ether-ketone matrix and carbon fiber and fabricated using the autoclave method from the prepreg (APC-2). The volume fraction of the fibers is 60% according to the data provided by the manufacturer. The specimens are prepared according to ASTM D3039M with a centrally circular hole. The specimen dimensions and mechanical properties of AS4/PEEK laminate are summarized in Table 3 and Table 4, respectively. As presented in Table 3, L is the length of specimen, W is the width and D is the hole diameter. Fracture properties are summarized in Table 5 [29] and the values of fracture energies of the fiber and matrix in Table 5 are from [9]. Static tests were performed on a universal fatigue test

Table 3. The laminate dimensions

Laminate configuration	L [mm]	W [mm]	D [mm]	Thickness of each layer [mm]
$[0/90/–45/+45]_{3s}$	254	25.4	6.35	0.139
$[0/+45/90/-45]_{2s}$	100	20	5	0.125

Table 4. Material properties of AS4/PEEK

Material properties	AS4/PEEK
E_{11} [GPa]	138
$E_{22} = E_{33}$ [GPa]	10.2
$E_{12} = E_{13}$ [GPa]	5.7
E_{23}	3.7
$v_{12} = v_{13}$	0.3
v_{23}	0.45
X_{t} [MPa]	2070
X_{c} [MPa]	1360
$Y_{\mathrm{t}} = Z_{\mathrm{t}}$ [MPa]	86
$Y_{\mathrm{c}} = Z_{\mathrm{c}}$ [MPa]	230
$S_{12} = S_{13}$ [MPa]	186
S_{23} [MPa]	86

Table 5. Fracture properties of AS4/PEEK laminate

G_{Ic} [N/mm]	$G_{IIc} = G_{IIIc}$ [N/mm]	N [MPa]	S = T [MPa]	G_f [N/mm]	G_m [N/mm]	η	K_p [MPa/mm]
1.7	2	80	100	12.5	1.0	2.284	10^6

machine (TESTRESOURCES Model 930LX50-T2000).

6. Results and discussions

Numerical results of the progressive damage analysis of two quasi-isotropic open-hole specimens with the laminates' configuration of $[0/90/–45/+45]_{3s}$ and $[0/45/90/–45]_{2s}$ are presented in this section. First, degradation and failure analysis of the laminate with the configuration of $[0/45/90/–45]_{2s}$ is performed using the three different methods and compared to the numerical and experimental results of [7] to validate the model. Also presented are the results of the dependency of the present model to viscous regularization parameter and a mesh refinement study. Second, the predicted failure strength and damage of the laminate with the configuration of $[0/90/–45/+45]_{3s}$ is compared to the experimental results.

6.1. $[0/45/90/–45]_{2s}$ laminate

Figure 4 shows the comparison of load-displacement curves of different progressive damage approaches (Method I, II, and III) with the experimental and numerical data of [7] for $[0/45/90/–45]_{2s}$ AS4/PEEK laminate. It shows that once the damage accumulation increases and the laminate is not able to sustain more load, the strength reduces and numerical simulation is stopped due to excessive element distortion. Three regions can be seen in these curves: a linear response, softening trend representing the initiation and propagation of the damage such as fiber and matrix failure when damage occurs in critical number of elements, followed by a region in which the load capacity drops. Compared to the experimental and numerical data, the prediction of the current numerical simulations are quite close.

Mesh size study is performed to evaluate the effect of mesh density on the prediction of failure strength. Three different meshes ranges from a coarse (Mesh I), medium (Mesh II) to a fine (Mesh III) for the area around the hole are shown in Figure 5. The viscous regularization factor of 0.003 is used with the degradation analysis of Method I. It can be seen that for Mesh I the abrupt decrease of the ultimate strength is slightly greater than the experimental result and that it overestimates the failure strength by about 3 percent. By refining the mesh and reducing the aspect ratio of the meshes to close to 1, the results of Mesh II and III predictions show close agreement with those obtained experimentally. Although the characteristic length is considered in the damage analysis to minimize the mesh size effect, a slight dependency to the mesh size still exists in the numerical results.

Figure 6 gives the load-displacement results of different values of the viscosity parameter in Methods I and II. It can be seen that the smaller the viscous regularization factor, the more abrupt the failure and the smaller failure strength become. Since two

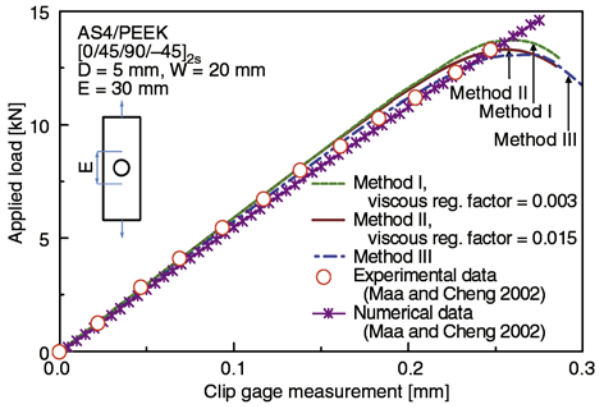

Figure 4. Comparison of predicted load-displacement curves of different progressive damage methods with the experimental and numerical data of [7] for $[0/45/90/–45]_{2s}$ AS4/PEEK laminate

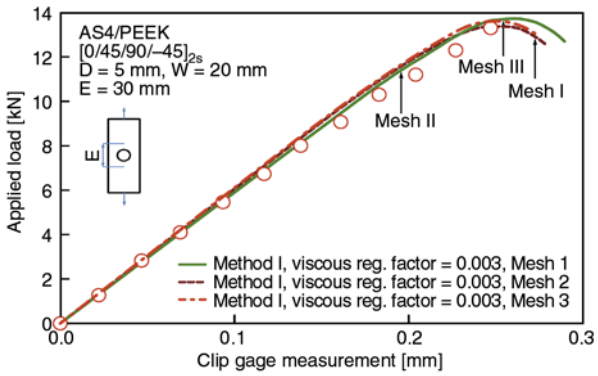

Figure 5. Comparison of load-displacement curves of different mesh sizes using Method I with the experimental data of [7] for $[0/45/90/–45]_{2s}$ AS4/PEEK laminate

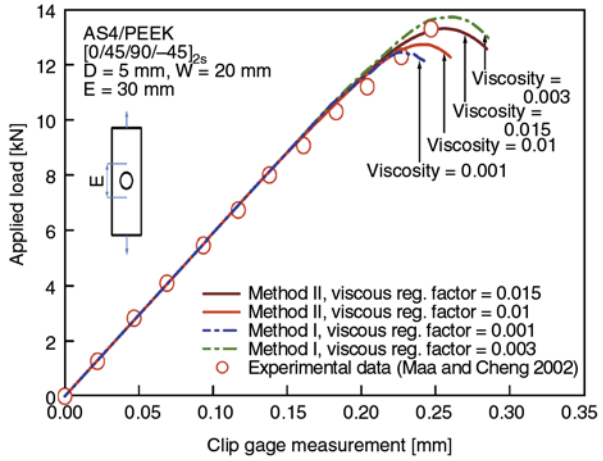

Figure 6. Comparison of predicted load-displacement curves of different values of viscosity parameters using Method I and II with the experimental data of [7] for $[0/45/90/–45]_{2s}$ AS4/PEEK laminate

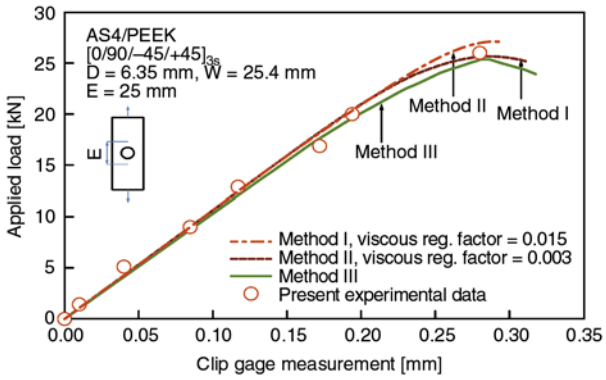

Figure 7. Comparison of predicted load-displacement curves of different progressive damage methods with the current experimental data of [7] for $[0/90/–45/+45]_{3s}$ AS4/PEEK laminate

approaches use different failure criteria, two different viscosity parameters are considered in the simulations. The intra-laminar damage initiation based on stress criteria seems to have higher viscosity factor than that of with strain criteria.

6.2. $[0/90/–45/+45]_{3s}$ laminate

The comparison of load-displacement curves of different progressive damage approaches (Method I, II, and III) with the experiment for $[0/90/–45/+45]_{3s}$ AS4/PEEK laminate is presented in Figure 7. The same viscous regularization factor as in the case of $[0/90/–45/+45]_{3s}$ laminate is used for this simulation. The simulation results are consistent with the experimental results.

Figure 8 shows inter-laminar or delamination damage pattern at 0/90°, 90/–45°, and –45/45° interface of $[0/90/–45/+45]_{3s}$ AS4/PEEK laminate at the time when the laminate strength start to drop. As shown in this figure, the delamination at 90/–45° and –45/45° interfaces are more severe than the delamination at 0/90° interface. Since the dominant failure stress in 0/90° interface is the normal stress, delamination pattern is in the zero degree direction. In the case of 90/–45° and –45/45° interface, the delamination patterns tend toward the 45° failure direction.

A contour plot of fiber and matrix damage variables d_f and d_m defined in Equations (11) and (12) as well as the surfaces of the failed specimen for $[0/90/–45/+45]_{3s}$ AS4/PEEK laminate is shown in Figure 9. Figure 9 also shows how implementation of the stochastic in material properties changes the failure behavior and path of the laminate. As seen in Figures 9a–9c the intra-laminar damage of the 0° fibers which are the most catastrophic failure types within the laminate initiates at the tip of the hole and propagates in the direction perpendicular to the load direction. In order to show the randomness behavior of failure due to probable distribution of the material properties, the scatter of the 0° fiber failure path is obtained by re-running the model for three times (paths 1, 2, 3). In each run, the failure path differs in the direction perpendicular to the fiber directions. Comparing Figures 9a–9c with the

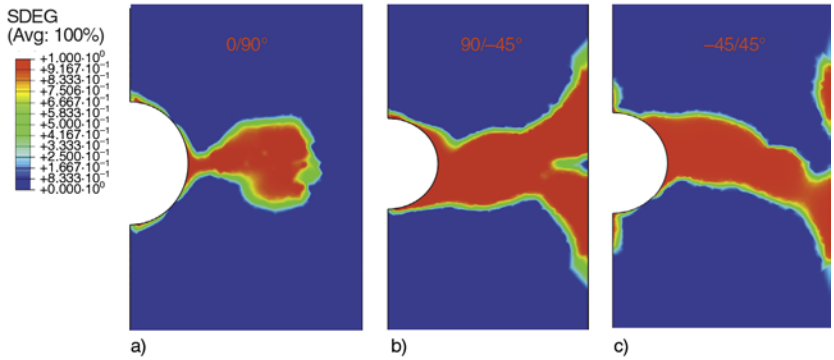

Figure 8. Delamination failure at the interface of 0/90° (a), 90/–45° (b), and –45/45° (c) for $[0/90/–45/+45]_{3s}$ AS4/PEEK laminate using Method I

image of failed specimen (Figure 9d), the results indicate that the failure of 0° plies can be either in the direction perpendicular to the fibers or in the inclined direction depending on sub-critical damage development in the adjacent plies. The numerical failure paths in Figures 9a–9c are consistent with the image of the failed laminate. Figures 9e–9f show the damage patterns for matrix failure in 90 and 45° plies, respectively. The matrix strength, Y_t, is small compared to the fiber strength, X_t, and matrix failure is the sever type of the damage in 90, 45, and –45° plies. As seen in Figures 9e–9f, the matrix failure path of 90 and 45° plies is in the 0 and 45 directions, respectively (path 4, 5).

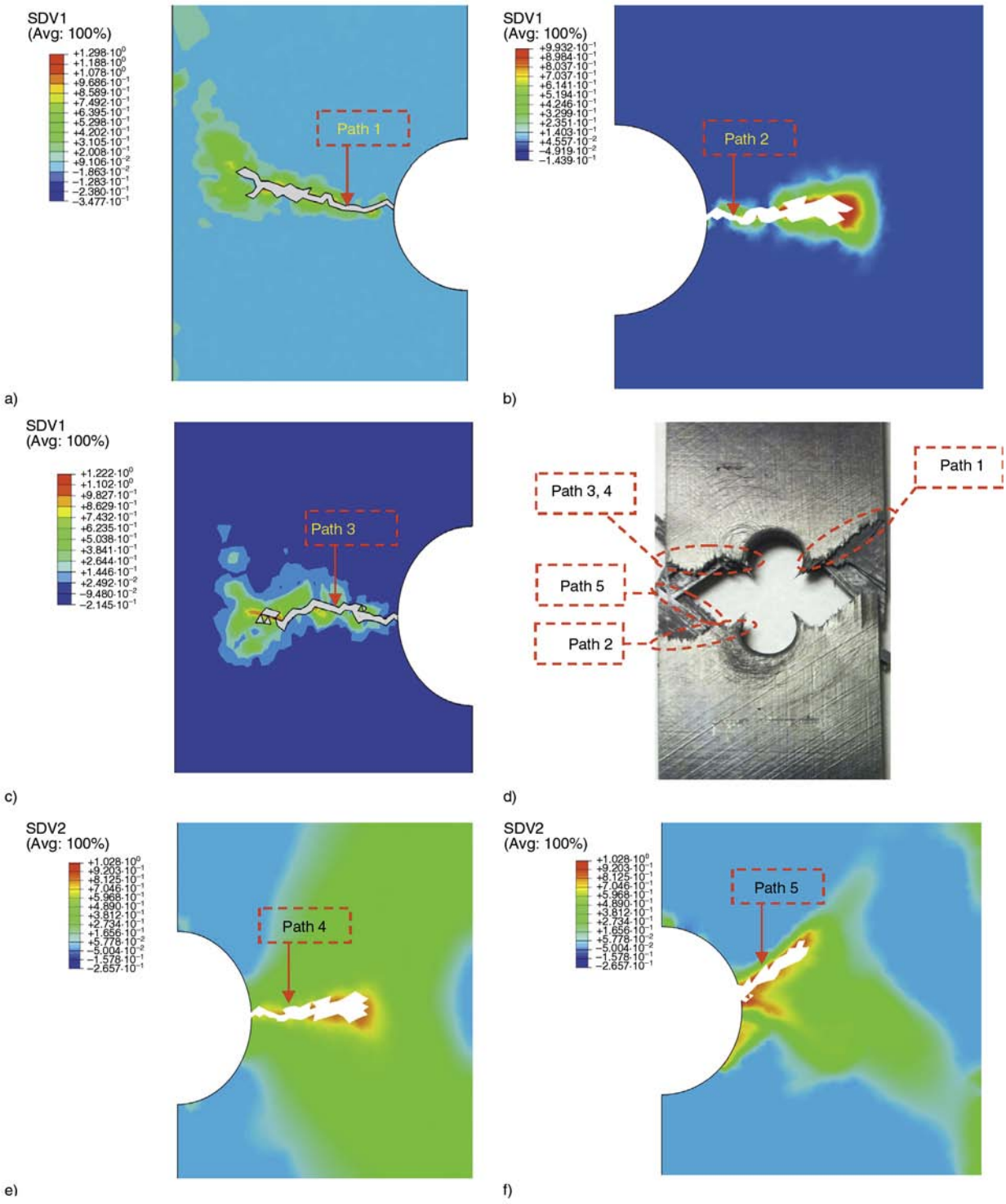

Figure 9. Intra-laminar damage patterns of fiber and matrix for $[0/90/–45/+45]_{3s}$ AS4/PEEK laminate at the time of abrupt strength reduction. a, b, c) fiber damage image in 0° layer for different simulation runs. d) an open-hole failed specimen under static test. e) matrix damage pattern in 90° layer. f) matrix damage pattern in 45° layer.

Although the presented simulation results of progressive damage obtained from different methods are in agreement with experiments, several points about the comparison of different methods would be in order. Methods I and II have the advantage of modeling delamination, fiber and matrix failure using a damage parameter and embedded cohesive elements in the model. However, their computational time is more expensive and numerical convergence is more problematic than those of Method III. Method III uses the sudden material property degradation rule which may raises questions and difficulties in validation of numerical results for complex geometry and laminate. However, from engineering point of view, Method III is fast and may give a realistic approximation of the laminate's strength. All of these methods depend on mesh type, mesh number, viscous regularization factor, and material property degradation rule. Future works considering the above-mentioned restrictions along with more recent computational methods such as X-FEM and A-FEM with considerations of randomness in the distribution of material properties are necessary to tackle the design of open-hole or notched laminates in a more realistic manner. Further, numerical results show how the numerical results are sensitive to mesh type, viscous regularization factor and distribution of material properties. Questions such as how should the variation of material properties be chosen and how sensitive are the mesh type and size to a random function of material distribution can be answered once a realistic material morphology is available. Future research is needed to study the effect of material property distribution functions along with a realistic characterization of the laminate morphology that can be implemented in a robust computational method such as X-FEM or A-FEM. Capability to model arbitrary crack path and discrete damage in a composite laminate are thus needed.

7. Conclusions

The present paper presents a study of the progressive intra- and inter-laminar damage coupled with cohesive elements for the failure simulation of two quasi-isotropic open-hole AS4/PEEK laminates with $[0/90/–45/+45]_{3s}$ and $[0/45/90/–45/]_{2s}$ configurations. Three different approaches (Method I, II and III) are implemented in ABAQUS™ user subroutine (UMAT) to simulate the degradation. Method I is a strain-based damage evolution while Method II is the modified of Method I and stress-based damage evolution proposed in this work. Method III obeys the Hashin-based degradation evolution criteria. Gaussian distribution is considered to model the scatter of material properties during the simulation. The model is applied to predict the strength of the open-hole laminate and the simulation results correlate well with the experimental data of the present work and [7]. A parametric study is performed for the effect of different mesh sizes and viscous regularization factors. The results show that in Methods I and II the damage prediction is sensitive to viscous regularization factor and mesh sizes. However, in latter, the characteristic length of the elements is considered to minimize the effect of the mesh size. The results of different damage patterns of the 0° fibers indicates that depending on the stochastic material properties, the failure path differs each time the model is run. The study on the effects of Gaussian distribution of material properties shows that depending on the scattering of material properties, the damage propagation and failure path vary each time the numerical simulation is run. The failure paths obtained from re-running the simulation for several times are in close agreement with the image of fractured specimen.

References

[1] Chang K-Y., Liu S., Chang F-K.: Damage tolerance of laminated composites containing an open hole and subjected to tensile loadings. Journal of Composite Materials, **25**, 274–301 (1991).
DOI: 10.1177/002199839102500303

[2] Hashin Z.: Failure criteria for unidirectional fiber composites. Journal of Applied Mechanics, **47**, 329–334 (1980).
DOI: 10.1115/1.3153664

[3] Lessard L. B., Shokrieh M.: Two-dimensional modeling of composite pinned-joint failure. Journal of Composite Materials, **29**, 671–697 (1995).
DOI: 10.1177/002199839502900507

[4] Dano M-L., Gendron G., Picard A.: Stress and failure analysis of mechanically fastened joints in composite laminates. Composite Structures, **50**, 287–296 (2000).
DOI: 10.1016/S0263-8223(00)00119-7

[5] İçten B. M., Karakuzu R.: Progressive failure analysis of pin-loaded carbon–epoxy woven composite plates. Composites Science and Technology, **62**, 1259–1271 (2002).
DOI: 10.1016/S0266-3538(02)00071-4

[6] Hoffman O.: The brittle strength of orthotropic materials. Journal of Composite Materials, **1**, 200–206 (1967). DOI: 10.1177/002199836700100210

[7] Maa R-H., Cheng J-H.: A CDM-based failure model for predicting strength of notched composite laminates. Composites Part B: Engineering, **33**, 479–489 (2000). DOI: 10.1016/S1359-8368(02)00030-6

[8] Ding S., Tong J. W., Wang Z. Y., Huo Y.: Fracture characters and damage mechanism of the notched AS4/PEEK composite laminate. Journal of Thermoplastic Composite Materials, **23**, 565–581 (2010). DOI: 10.1177/0892705709347094

[9] Lapczyk I., Hurtado J. A.: Progressive damage modeling in fiber-reinforced materials. Composites Part A: Applied Science and Manufacturing, **38**, 2333–2341 (2007). DOI: 10.1016/j.compositesa.2007.01.017

[10] Falzon B. G., Apruzzese P.: Numerical analysis of intralaminar failure mechanisms in composite structures. Part II: Applications. Composite Structures, **93**, 1047–1053 (2011). DOI: 10.1016/j.compstruct.2010.06.022

[11] Camanho P. P., Maimí P., Dávila C. G.: Prediction of size effects in notched laminates using continuum damage mechanics. Composites Science and Technology, **67**, 2715–2727 (2007). DOI: 10.1016/j.compscitech.2007.02.005

[12] Abisset E., Daghia F., Ladevèze P.: On the validation of a damage mesomodel for laminated composites by means of open-hole tensile tests on quasi-isotropic laminates. Composites Part A: Applied Science and Manufacturing, **42**, 1515–1524 (2011). DOI: 10.1016/j.compositesa.2011.07.004

[13] van der Meer F. P., Sluys L. J., Hallett S. R., Wisnom M. R.: Computational modeling of complex failure mechanisms in laminates. Journal of Composite Materials, **46**, 603–623 (2012). DOI: 10.1177/0021998311410473

[14] Fang X. J., Zhou Z. Q., Cox B. N., Yang Q. D.: High-fidelity simulations of multiple fracture processes in a laminated composite in tension. Journal of the Mechanics and Physics of Solids, **59**, 1355–1373 (2011). DOI: 10.1016/j.jmps.2011.04.007

[15] Daghia F., Ladevèze P.: A micro–meso computational strategy for the prediction of the damage and failure of laminates. Composite Structures, **94**, 3644–3653 (2012). DOI: 10.1016/j.compstruct.2012.05.028

[16] van der Meer F. P., Sluys L. J.: A phantom node formulation with mixed mode cohesive law for splitting in laminates. International Journal of Fracture, **158**, 107–124 (2009). DOI: 10.1007/s10704-009-9344-5

[17] Moës N., Belytschko T.: Extended finite element method for cohesive crack growth. Engineering Fracture Mechanics, **69**, 813–833 (2002). DOI: 10.1016/S0013-7944(01)00128-X

[18] Yang Q. D., Liu W., Mohammadizadeh S., Su X-Y., Ling D-S.: An accurate and efficient A-FEM for arbitrary crack interactions. Journal of Mechanics of Materials, in press (2013). DOI: 10.1115/1.4007970

[19] Hansbo A., Hansbo P.: A finite element method for the simulation of strong and weak discontinuities in solid mechanics. Computer Methods in Applied Mechanics and Engineering, **193**, 3523–3540 (2004). DOI: 10.1016/j.cma.2003.12.041

[20] Camanho P. P., Dávila C. G.: Mixed-mode decohesion finite elements for the simulation of delamination in composite materials. NASA/TM-2002–211737 2002, 1–37 (2002).

[21] Linde P., Pleitner J., Boer H., Carmone C.: Modeling and simulation of fiber metal laminates. in 'ABAQUS users' Conference, Boston, USA' 421–439 (2004).

[22] ABAQUS/standard version 6.10. User Manual, Hibbit, Karlsson and Sorensen Inc., Rhode Island, USA (2010).

[23] Benzeggagh M. L., Kenane M.: Measurement of mixed-mode delamination fracture toughness of unidirectional glass/epoxy composites with mixed-mode bending apparatus. Composites Science and Technology, **56**, 439–449 (1996). DOI: 10.1016/0266-3538(96)00005-X

[24] Wu E. M., Reuter R. C.: Crack extension in fiberglass reinforced plastics. T&M Report 275, University of Illinois, USA (1965).

[25] Reeder J., Kyongchan S., Chunchu P. B., Ambur R.: Postbuckling and growth of delaminations in composite plates subjected to axial compression. in 'AIAA/ASME/ASCE/AHS/ASC Structures, Structural Dynamics, and Materials Conference, Denver, Colorado' p.10 (2002).

[26] Camanho P. P., Daliva C., G., de Moura M. F.: Numerical simulation of mixed-mode progressive delamination in composite materials. Journal of Composite Materials, **37**, 1415–1438 (2003). DOI: 10.1177/0021998303034505

[27] Camanho P. P., Matthews F. L.: A progressive damage model for mechanically fastened joints in composite laminates. Journal of Composite Materials, **33**, 2248–2280 (1999). DOI: 10.1177/002199839903302402

[28] Tan S. C., Nuismer R. J.: A theory for progressive matrix cracking in composite laminates. Journal of Composite Materials, **23**, 1029–1047 (1989). DOI: 10.1177/002199838902301006

[29] Reeder J. R., Crews J. R.: Mixed-mode bending method for delamination testing. AIAA Journal, **28**, 1270–1276 (1990).

eXPRESS Polymer Letters Vol.7, No.4 (2013) 396–405
Available online at www.expresspolymlett.com
DOI: 10.3144/expresspolymlett.2013.36

Lamellar assembly and orientation-induced internal micro-voids by cross-sectional dissection of poly(ethylene oxide)/poly(L-lactic acid) blend

*Y. T. Hsieh, E. M. Woo**

Department of Chemical Engineering, National Cheng Kung University, 701 Tainan, Taiwan

Received 3 November 2012; accepted in revised form 13 January 2013

Abstract. Micro-lamellar patterns and orientation-induced micro-voids (cracks) in spherulites are probed in step-crystallized blends of two crystalline polymers: poly(ethylene oxide) (PEO) and low-molecular-weight poly(L-lactic acid) (PLLA) in different weight fractions, using polarizing light optical microscopy (POM), and scanning electron microscopy (SEM) with water-etching technique. It is revealed that blend composition led to entirely different PLLA lamellar regularities and void patterns. Water-etching into interiors of PEO/PLLA blends show 3D assembly of PLLA lamellae patterns. It is an important datum for structure modeling of banded polymer spherulites in bulk state. The mechanisms for the void/crack patterns and lamellar orientation are exemplified via dissecting into interior spherulites of bulk-form samples.

Keywords: *biodegradable polymers, biocompatible polymers, PLLA, bulk*

1. Introduction

Biodegradable polymer materials have attracted great scientific and technological interest at many application areas, such as packaging, biomedical material [1, 2]. For the packaging and medical applications, poly(lactic acid) (PLA) has one of the highest potentials among biopolyesters [1]. To tailor its crystallization behavior, degradation rate and other material properties for the applications, blending PLA with other biocompatible polymers is a practical and economical approach. PLA also is the one of the interesting polyesters in issues of chiral effect, crack and ring patterns, and spherulitic morphology in polymer physical research [3–7].

Rings and cracks in some semicrystalline polymers have been reported during cooling, crystallization or in contacting with solvents [4–10]. Overall, the conventionally known fact of thermal shrinkage/contraction upon cooling in different directions accounts only partially for the cracks. Updated studies have pointed out for biodegradable polyesters that cracks and ring bands can be inter-related and interrelations between rings and cracks can be more clearly resolved if interiors of the banding/cracking polymers can be exposed for examination.

Poly(ethylene oxide) (PEO), a water soluble polyether, possesses good biocompatibility and has very low toxicity in bio-medical applications [11, 12]. Phase behavior and biocompatibility of blends of PEO/poly(L-lactic acid) (PLLA) has been studied [13–15], and partial miscibility with phase domains in blends of PEO with PLLA of high molecular weights has been claimed. However, PEO also has been proven to be miscible with low-molecular-weight PLLA in our previous work [16]. An early pioneering work by Lustiger *et al*. [17] dealt with interior morphology correlating with surface ring bands in polyethylene (PE) bulk samples. In that

*Corresponding author, e-mail: emwoo@mail.ncku.edu.tw

work, the fracture surface as examined by SEM was exposed to reveal a central hole (on nuclei center) in banding PE spherulites. However, the interior morphology for general lamellar textures is not clear enough, as comparison to much better resolved top-surface rings and their lamellae patterns. Analyses of bulk PE were thus mainly based on the top-surface morphology, leaving issues of the interior lamellar assembly in banding spherulites still unresolved. This work, using PEO/PLLA blend as a model, intended to probe further, focusing on interior lamellae assembly in correlation with surface/interior cracking and banding by taking advantage of the water-soluble property of PEO under water-etching treatment. Such 3D dissection approach was also successfully adapted to interpret the correlation between the inner lamellar assembly, outer surface banding and 3D banding spheroids in poly(ethylene adipate) crystallized at T_c = 28±1°C [18].

Objectives in this letter were to utilize a technique of selectively removing the PEO component for exposing the cross-sectional surfaces of bulk-form samples for dissecting the inner PLLA lamellae to probe the correlations between inner cracks and outer ring bands in PEO/PLLA blend's crystal phases. Lamellar patterns and ring-band types in blends were found to vary with respect to blend compositions. The PEO component, used for helping to induce rings and suppressing cracks, could be easily etched out using pure water after its co-crystallization with PLLA in blends. As PEO and PLLA co-crystallized in two stage-crystallization, the role of PEO in the crystallized PEO/PLLA blend can be regarded as a temporary moldable filler among the PLLA lamellae. In continuing the previous study [16], correlations between the rings, cracks and lamellar pattern in ring-banded spherulites in PEO/PLLA blends were probed in greater details by comparing the lamellae and crack behavior of PLLA crystallizing with different PEO contents in blends. This study mainly focused on the PEO-rich blend compositions, and within this composition range, the blends were known to show unusual radial and irregular crack patterns instead of concentric cracks [16]. Objectives were further probing the mechanisms of lamellar patterns and orientation in ring bands responsible for inducing special types of surface rings and interior lamellar assembly and cracks in crystallized and cooled polymers at micro-scale, by delicately removing PEO from crystallized PEO/PLLA blends, but without altering the already fixed PLLA crystals, to expose more details of interior morphology.

2. Experimental

2.1. Materials

PEO with M_w = 20 000 g/mol, PDI = 1.16, T_g = –60°C and T_m = 64°C, was obtained from Aldrich (USA). PLLA was purchased from Polysciences, Inc. (USA), with M_w = 11 000 g/mol, PDI = 1.11, T_g = 45.3°C and T_m = 155°C. Materials were used as received without further purification.

2.2. Preparation of PEO/PLLA thin films

Blends sample films of PLLA with PEO were prepared by solution-casting using chloroform as solvent. Two polymers of intended compositions were dissolved in solvent with a concentration of 4 wt%, well stirred, and cast onto micro glass slides at 45°C. The solvent in blend films was first evaporated and dried at 45°C for 24 h, and then further dried in vacuum at ~40°C for several days.

Blend samples were pressed as thin films between two micro glass slides to obtain uniform film thickness (~10 μm) on a heating stage. Crystallization of blend samples was done at isothermal 110°C (crystallization temperature, T_c) by quenching from the molten state at maximum melting temperature (T_{max}) = 190°C. Degradation of neat PLLA under static air was analyzed using thermogravimetric analysis (TGA). In air, degradation of neat PLLA initiated at ~200°C. As a result, 190°C was used as T_{max} in this study. As PEO in blends is easily water soluble, PEO could be water-etched from PEO/PLLA blends, leaving the PLLA lamellae unaltered by dripping deionized water on to tilted sample. For this purpose, an easily releasable polyimide (PI) film was used for temporary covering the samples during crystallization; after crystallization and cooling, PI film was peeled off from blend samples. Furthermore, a gentle etching process was conducted to maintain the polymer film sticking on the substrate rather than floating on water.

2.3. Sample characterization

A polarizing optical microscope (Optiphot-2-POL, Nikon, Japan), equipped with a digital camera charge-coupled device (CCD) and a microscopic hot stage (Linkam THMS-600 with TP-92 tempera-

ture programmer), was used for characterizing crystalline morphology of the polymers.

Samples of solution-cast films of PEO/PLLA blends were also examined using a scanning electron microscope (SEM) (Quanta-400F, FEI, USA), and its accelerating voltage was 10 kV for revealing the lamellar pattern of spherulites. The top surfaces of the exposed film samples on the bottom micro glass slides were then coated with gold by vacuum-sputtering prior to SEM characterization.

3. Results and discussion

POM and optical microscopy (OM) characterization was performed on the 110°C-crystallized PEO/PLLA blends of several PEO-rich compositions (PEO ≧ 50 wt%) for further clarifying the correlations between the patterns of the crystalline ring bands and cracks. During the two-stage crystallization (first at crystallization temperature T_c = 110°C then cooling to ambient temperature) of the PEO/PLLA blends, the pre-formed PLLA ring-banded lamellae at T_c serves as nucleating templates for the later-crystallizing PEO species upon cooling to ambient temperature, and then the cracks could be observed after the PEO crystallizing. Figure 1 shows with increasing of the PEO content, the PLLA optical ring bands became less ordered. Under in-situ observation by using POM, long cracks always took place at the impingement of PEO spherulites with the preformed PLLA crystals. At 80 wt% of PEO in the PEO-rich blend, the PLLA optical ring bands in the spherulites are not distinct or entirely disrupted at all, as shown in the POM graph of Figure 1c. And, the crack pattern was changing from the long radial type to the short irregular type as the content of PEO increase to 80 wt%. There could be found a transition stage of the crack patterns at PEO/PLLA (70/30) blend which had both the radial and the irregular cracks on one sample. Cooling-induced thermal shrinkage due to directional CTE difference alone may not be sufficient in fully accounting for the cracks of these different types.

Figure 2 shows the POM and OM graphs of the water-etched PEO/PLLA blends after the two-stage crystallization. Upon water-etching, it was found that PEO was dominantly and selectively removed from the ridge bands to expose the inner PLLA crystals underneath the ridges. As will be shown in latter results/discussion, PLLA lamellar crystal plates in the ridge region are perpendicular to top surface of

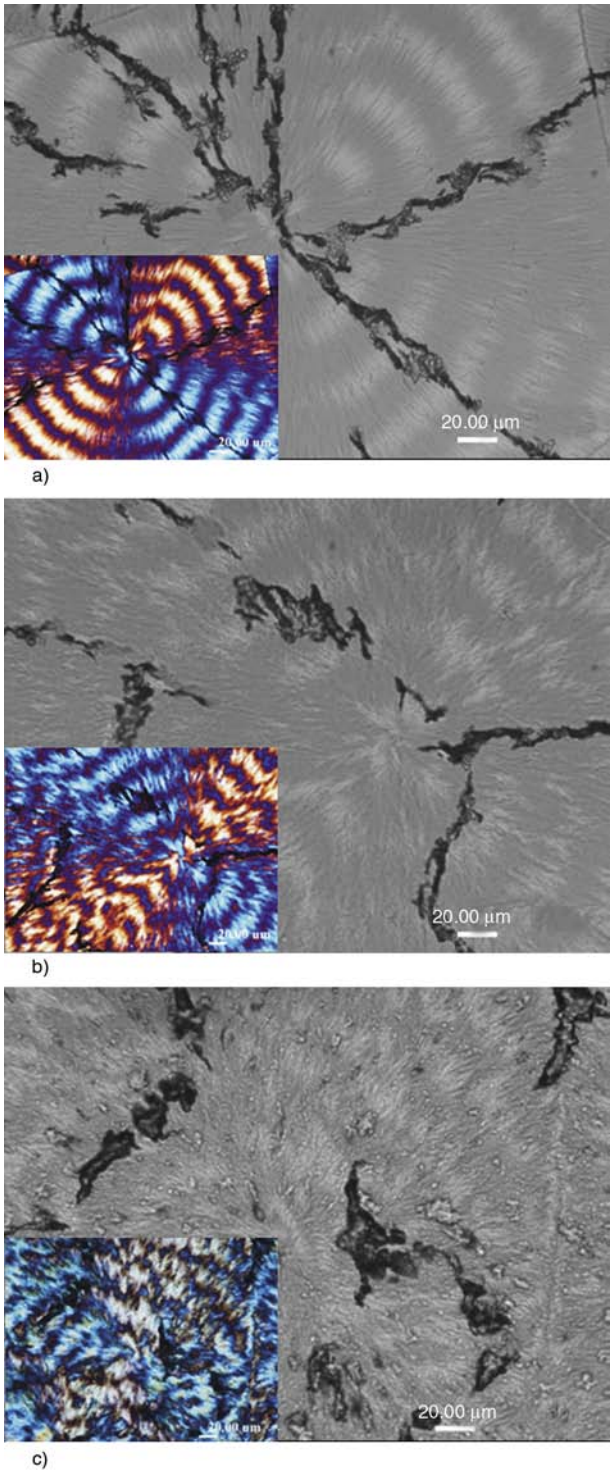

Figure 1. OM graphs of PEO/PLLA blends (unetched) crystallized at 110°C then cooled to ambient temperature (25–28°C) of compositions: (a) 60/40, (b) 70/30, and (c) 80/20 (Insets: POM graphs revealing ring-band patterns)

the samples, and PEO component tends to aggregate between the PLLA lamellae that point upwards. Thus, upon water-etching, the ridge bands were visibly lined with lenticular-shape voids/cracks that were previously occupied by PEO components. The

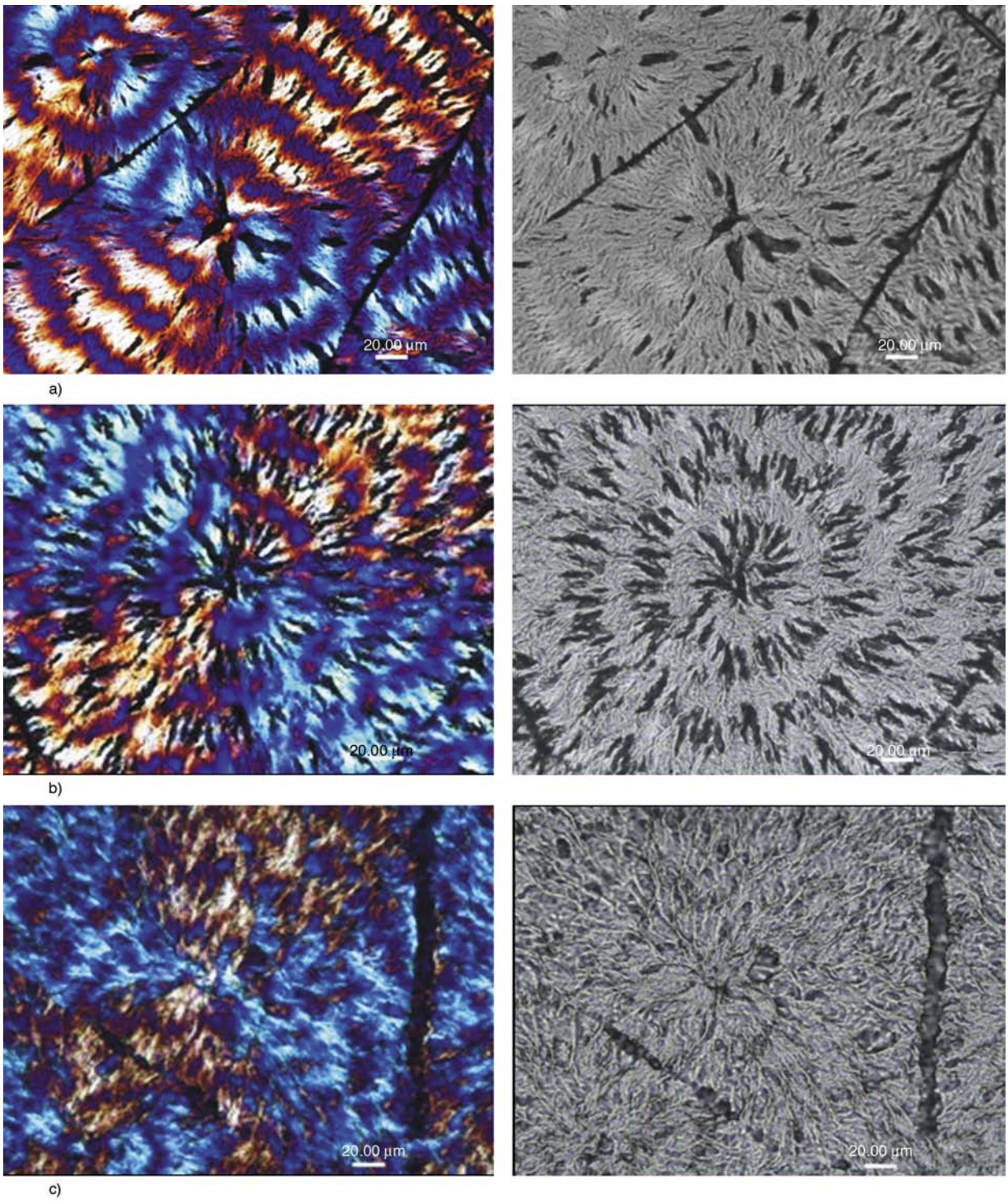

Figure 2. POM (left) and OM (right) graphs of PEO/PLLA blends (water-etched) crystallized at T_c = 110°C then cooled to ambient temperature (25–28°C) of compositions: (a) 60/40, (b) 70/30, and (c) 80/20

OM graphs for same samples are shown at right side of the POM graphs for comparison of contrast between POM and OM imaging interpretation on the etching effect. For Figure 2a and Figure 2b, the water-etching affected not only on the bright bands but also dark band; however, the etching took place more severely and circumferentially on the entire dark bands, which was indicated from our previous study [16]. By comparison, the bright band (ridge band) remained relatively unaffected by water etching but the bright band became coarser after etching. For Figure 2c, the etching of PEO from the PEO/PLLA (80/20) blend revealed that the PLLA lamellae assumed seaweed patterns, with connected

voids (initially filled with the etched-off PEO component) bordering by the networking and irregularly twisting micro-lamellae of PLLA.

Figure 3 shows SEM graphs for the fractured surface of two-stage crystallization PEO/PLLA (50/50) blends of: (a) unetched sample, (b) water-etched sample. As fracture line might cut through the valley or ridge bands, the lamellar patterns underneath the respective valley or ridge could be exposed for analysis. The fractured sample was further water-

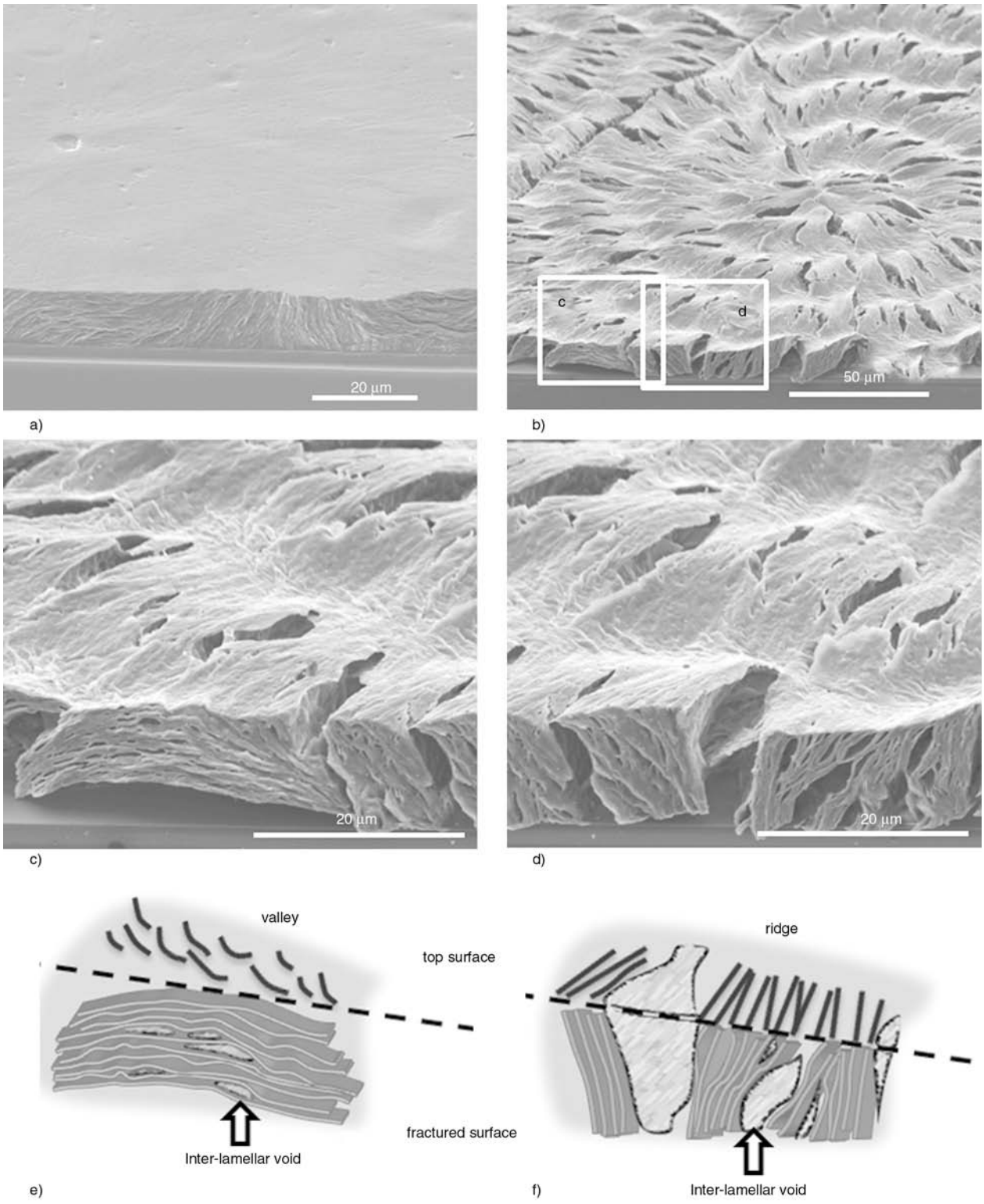

Figure 3. SEM graphs for fractured surface of PEO/PLLA (50/50) blends crystallized at T_c = 110°C then cooled to ambient temperature (25–28°C) of: (a) unetched sample, (b) water etched sample, (c) zoom-in valley 'Region-c', (d) zoom-in ridge 'Region-d'. Schemes of (e) and (f): lamellae assembly and re-orientations of PLLA micro-lamellae at valley and ridge, respectively.

etched to remove the PEO from the blend and as a result, PLLA lamellar plates were more clearly exposed. The fractured-surface morphology in the SEM graphs display clearly that the lamellar assembly and orientation are oppositely different in the valley and ridge regions. These two regions are zoomed-in and magnified as shown in SEM graphs in Figure 3c (fracture across the valley band) and Figure 3d (fracture across the ridge band), respectively. The lamellar assembly underneath the valley band apparently runs in circumferential direction while the lamellae underneath the ridge band run perpendicular to the film surface. The perpendicular lamellae underneath the ridge band would appear as 'edge-on' when viewed from the top; conversely, the circumferential lamellae underneath the valley band would appear as 'flat-on' when viewed from the top. Details of the micro-lamellar orientation and void patters as exposed in the PEO/PLLA (50/50) were shown in two schemes (Figure 3e and 3f). The two direction lamellar assembly mention above is at micro-scale, mainly combining from nano-scale PLLA lamellar crystals and amorphous PLLA chains, called as flat-on micro-lamellae and edge-on micro-lamellae, respectively.

In addition, the fractured and water-etched interiors of PEO/PLLA (50/50) blend also expose interesting correlations between the lamellar plates and crack orientations. Lenticular-shaped voids on the top surface are oriented in the radial direction between the perpendicular edge-on micro-lamellae in the ridge band (bright bands). The schemes, reflecting the actual fractured morphology in SEM graphs shown earlier in Figure 3, show that the voids are not only on the top surface but also on the hidden interior exposed by the fracture surface, as indicated by the arrow marks. On the other hand, with increasing PEO contents in PEO/PLLA blends, the water-etched PEO/PLLA (70/30, 80/20, and 90/10) blends exhibit more irregular twisting PLLA micro-lamellae, resembling seaweeds. The top surface observation results of water-etched PEO/PLLA (70/30, 80/20, and 90/10) blends by using SEM are shown in the Figure 4. As the PEO content increases even higher to 80 or 90 wt%, only the irregularly twisting micro-lamellae were present, and the micro-lamellae are in less dense assembly. In Figure 4b and 4c, some connected voids appear, similar to the OM-revealed result as shown in Figure 2c.

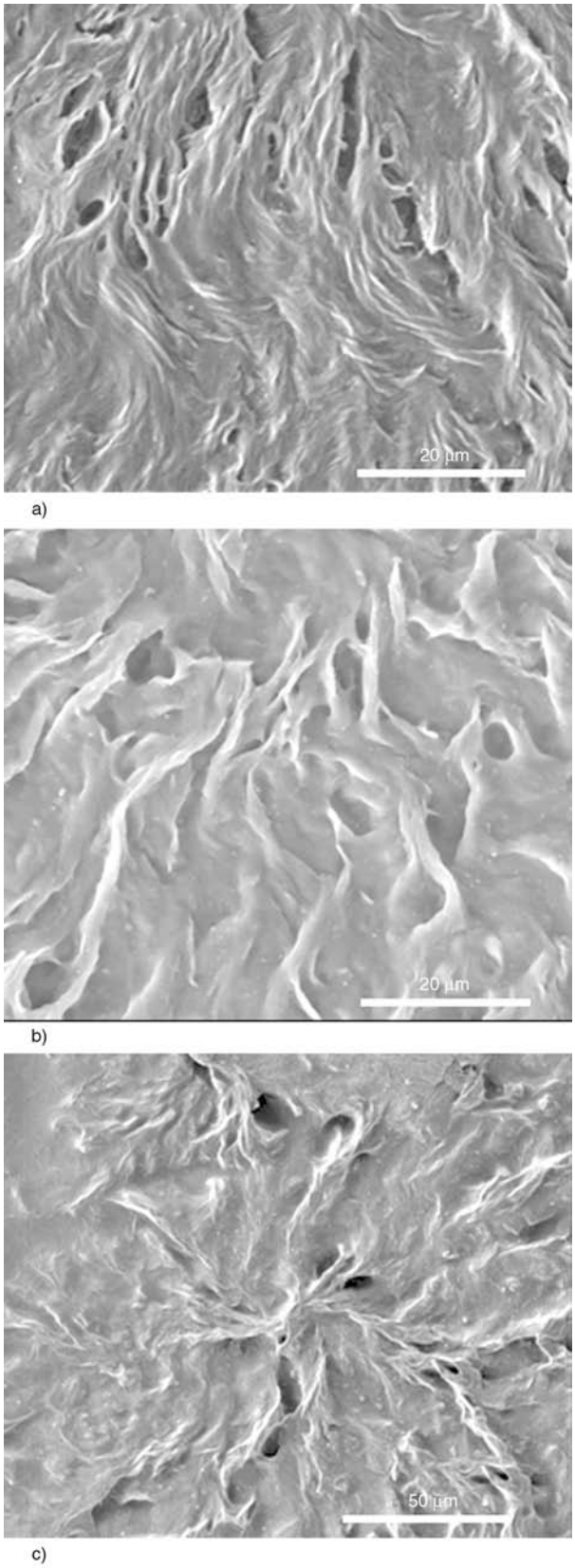

Figure 4. SEM graphs of the water-etched PEO/PLLA blends crystallized at T_c = 110°C then cooled to ambient temperature (25–28°C) of compositions: (a) 70/30, (b) 80/20, and (c) 90/10

Figure 5 shows SEM graph and scheme for the fractured surface of the water-etched PEO/PLLA (70/30) blends crystallized at T_c = 110°C then cooled to ambient temperature (~25°C). The upper portion of the SEM graph and scheme are for the top surface, while the lower portion reveals the fracture surface of the water-etched PEO/PLLA (70/30) blend. Fracture line again is seen to run across the interiors of the ridge and valley bands. Similar to the interiors of the PEO/PLLA (50/50) blend, the lamellar plates underneath the surface ridge bands of the PEO/PLLA (70/30) blend are oriented as perpendicular plates although the lamellar plates are not as regular and orientation is less ordered. The lamellar plates underneath the valley in the PEO/PLLA (70/30) blend are horizontally oriented, but the horizontal orientation is less ordered than that in the 50/50 blend. By comparison, for the PEO/PLLA blend with a higher PEO content at 70 wt%, the lamellar patterns on the top surface are seen to be more irregular and the voids increase in number in comparison to the morphology in the water-etched PEO/PLLA (50/50) blend. The top surface still exhibits lenticular-shaped voids, but as the packing density of the lamellar crystals are smaller and less regularly positioned, the voids diminish in size.

Overall, the PEO/PLLA 50/50 blend exhibits more ordered lamellar plates underneath the ridge and valley bands; as a result, the unetched 50/50 blend sample exhibits the long radial cracks on the ridge bands when viewed from the top. By contrast, in interior of the PEO/PLLA blends of PEO-rich compositions (PEO content above 70 wt%), the lamellar plates are increasingly less ordered, and only irregular cracks of smaller sizes are present. From the 3D interior dissecting analyses into the interior morphology, it then became easy to comprehend the lamellar assembly and cracks seen in ringed spherulites of the top surface of thin-film PEO/PLLA samples. Schemes of micro-lamellar orientation and cracks are summarized in Figure 6, which illustrates how micro-lamellar plates interact with crack/ring formation mechanisms in the PEO-rich PEO/PLLA blends of compositions: (a) 50/50, and (b) 80/20 as examples. Ideally, etching of PEO would be more complete if etching was performed at T_m of PEO. Thus, etching by warm water was performed on crystallized blends of several compositions. However, results were not suitable for analysis owing to several reasons. Rings/PLLA lamellae in warm water etched samples were highly disrupted to extents of hardship in subsequent analysis on PLLA morphology. Films would be disintegrated, floated from glass substrate, and bulk samples would be crumbled into irregular particles.

The diagrams on top the schemes are SEM top-surface morphology for PEO/PLLA (50/50 and 80/20) blends. For the PEO/PLLA (50/50) blend, the ridge bands are PLLA lamellae that are oriented perpendicular to the substrate, though with some occasional twist/bending. When the blend was crystallized at T_c = 110°C, PEO remained molten; but as temperature was cooled to ambient, PEO started to crystallize along the pre-crystallized PLLA crystals.

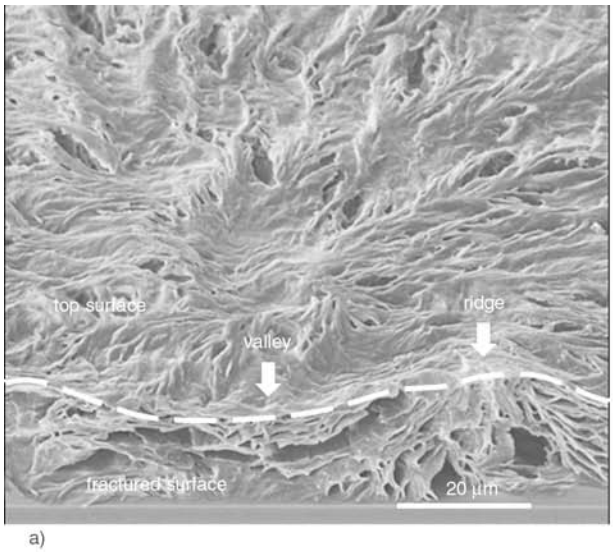

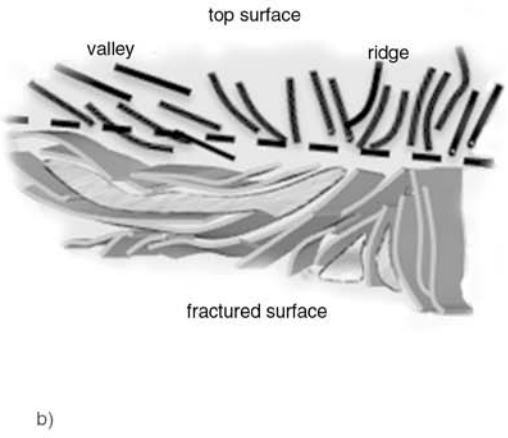

Figure 5. (a) SEM graph and (b) scheme for the fractured surface of the water-etched PEO/PLLA (70/30) blends crystallized at T_c = 110°C then cooled to ambient temperature (25–28°C)

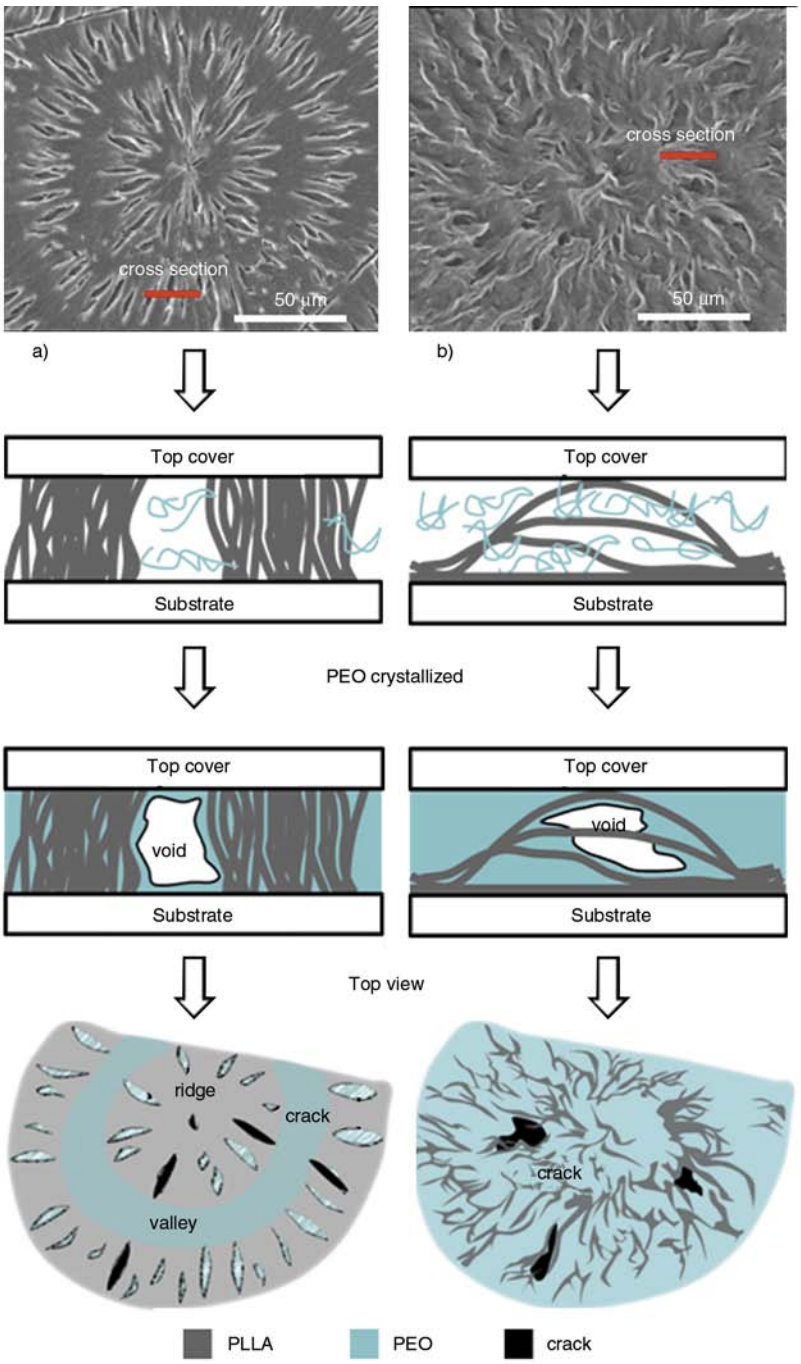

Figure 6. Internal micro-voids/crack formation mechanisms in the PEO/PLLA blends with compositions: (a) 50/50, and (b) 80/20

Thus, PEO molecules were confined in the inter-lamellar regions of PLLA crystals, substrate and top cover. When PEO crystals met and impinged each other in this limited space, the void appeared from the volume reduction of the PEO crystallization. The void was forced to exist by the density difference between molten and semicrystalline PEO state. At the same time, the crack showed up by using POM observation. With the PEO contents in PEO/PLLA blends increase to 70 or 80 wt%, the lamellar assembly and crack formation in the PEO-rich blends have similar mechanisms as that in PEO/PLLA (50/50) blends, but the PLLA lamellar plates decrease in dimensions and orderliness. The PLLA lamellae in the PEO-rich PEO/PLLA blends are increasingly similar to seaweeds with random twists and arrangement, and the lamellae are no longer regularly assembled to perpendicular orientation in ridges and horizontal positions in valleys. Cracks appear to turn as lamellae take turn, and they are no

longer in the regular radial direction, but take irregular turns with the randomly oriented PLLA lamellar crystals.

4. Conclusions

Correlations among internal micro-voids/cracks, ring bands, and interior lamellar assembly in PEO/PLLA blend were analyzed; and bulk-form and thin-film blend samples with different compositions were probed for interior lamellar assembly extending to outer-surface morphology. By extracting the water-soluble PEO component from the crystallized PEO/PLLA blend of PEO-rich compositions, the PLLA lamellar textures further revealed a complex pattern. The periodical interior micro-lamellar textures in PLLA spherulite as exposing by SEM observation might have further help to construct the structure model for banded spherulites in bulk-form samples. By exposing the interior assembly of thick bulk polymer blend samples that formed either cracks or ring bands on top surface, the interior PLLA crystal assembly, after extracting out water-soluble PEO, was more clearly demonstrated. Such views and aims have been rarely dealt with, if any before in the literature, for revealing the inner PLLA spherulitic structure in 3D (i.e., *x*, *y* and *z*-views).

Lamellar-twisting model, though tested and proposed for long time by many researchers, dealt only with semicrystalline polymer samples mainly in thin-film state (~1–5 μm). The results in this work have generated alternative, and perhaps richer, views on interior lamellar assembly in thick bulk state that may be responsible for leading to the top-surface crack/ring bands. In 3D views by cutting across the band ridge and valley, respectively, the lamellar assembly underneath the valley band apparently runs in the circumferential direction while the lamellae underneath the ridge band run perpendicular to the top-surface of samples. Moreover, the internal and exterior voids/cracks in crystallized PLLA always run parallel to the micro-lamellar plates. The radial cracks/voids always coincide well with the ridge band of the alternating ring bands, as underneath the ridge regions, the lamellae plates are oriented perpendicularly to the top surfaces and are easily visible from the top views. Upon cutting across the thickness section of the bulk samples, voids/cracks in the valley regions, on the other hand, are sandwiched between tangential lamellar plates, and thus not visible from the top surface.

Acknowledgements

This work has been financially supported by basic research grants (NSC-99-2221-E-006-014-MY3) in consecutive years from Taiwan's National Science Council (NSC), for which the authors express their gratitude. The authors especially express their gratitude to Dr. B. Lotz, Institut Charles Sadron, Strasbourg, France, for his careful checking and helpful inputs that have enhanced the depth of the work during progress and manuscript preparation.

References

[1] Fortunati E., Armentano I., Zhou Q., Iannoni A., Saino E., Visai L., Berglund L. A., Kenny J. M.: Multifunctional bionanocomposite films of poly(lactic acid), cellulose nanocrystals and silver nanoparticles. Carbohydrate Polymers, **87**, 1596–1605 (2012).
DOI: 10.1016/j.carbpol.2011.09.066

[2] Yu H-Y., Qin Z-Y., Wang L-F., Zhou Z.: Crystallization behavior and hydrophobic properties of biodegradable ethyl cellulose-g-poly(3-hydroxybutyrate-co-3-hydroxyvalerate): The influence of the side-chain length and grafting density. Carbohydrate Polymers, **87**, 2447–2454 (2012).
DOI: 10.1016/j.carbpol.2011.11.022

[3] Maillard D., Prud'homme R. E.: Crystallization of ultrathin films of polylactides: From chain chirality to lamella curvature and twisting. Macromolecules, **41**, 1705–1712 (2008).
DOI: 10.1021/ma071306u

[4] Fraschini C., Plesu R., Sarasua J. R., Prud'homme R. E.: Cracking in polylactide spherulites. Journal of Polymer Science Part B: Polymer Physics, **43**, 3308–3315 (2005).
DOI: 10.1002/polb.20616

[5] He Y., Fan Z., Wei J., Li S.: Morphology and melt crystallization of poly(L-lactide) obtained by ring opening polymerization of L-lactide with zinc catalyst. Polymer Engineering and Science, **46**, 1583–1589 (2006).
DOI: 10.1002/pen.20617

[6] Nurkhamidah S., Woo E. M.: Effects of crystallinity and molecular weight on crack behavior in crystalline poly(L-lactic acid). Journal of Applied Polymer Science, **122**, 1976–1985 (2011).
DOI: 10.1002/app.34021

[7] Nurkhamidah S., Woo E. M.: Correlation of crack patterns and ring bands in spherulites of low molecular weight poly(L-lactic acid). Colloid and Polymer Science, **290**, 275–288 (2012).
DOI: 10.1007/s00396-011-2544-3

[8] Martinez-Salazar J., Sanchez-Cuesta M., Barham P. J., Keller A.: Thermal expansion and spherulite cracking in 3-hydroxybutyrate/3-hydroxyvalerate copolymers. Journal of Materials Science Letters, **8**, 490–492 (1989).
DOI: 10.1007/BF00720717

[9] Hobbs J. K., McMaster T. J., Miles M. J., Barham P. J.: Cracking in spherulites of poly(hydroxybutyrate). Polymer, **37**, 3241–3246 (1996).
DOI: 10.1016/0032-3861(96)88468-0

[10] Kuboyama K., Ougizawa T.: Solvent induced cracking and morphology in banded spherulite of poly(trimethylene terephthalate). Polymer Journal, **40**, 1005–1009 (2008).
DOI: 10.1295/polymj.PJ2007194

[11] Lee J. H., Kim K. O., Ju Y. M.: Polyethylene oxide additive-entrapped polyvinyl chloride as a new blood bag material. Journal of Biomedical Materials Research, **48**, 328–334 (1999).
DOI: 10.1002/(SICI)1097-4636(1999)48:3<328::AID-JBM18>3.0.CO;2-L

[12] Ma G., Fang D., Liu Y., Zhu X., Nie J.: Electrospun sodium alginate/poly(ethylene oxide) core–shell nanofibers scaffolds potential for tissue engineering applications. Carbohydrate Polymers, **87**, 737–743 (2012).
DOI: 10.1016/j.carbpol.2011.08.055

[13] Nakafuku C., Sakoda M.: Melting and crystallization of poly(L-lactic acid) and poly(ethylene oxide) binary mixture. Polymer Journal, **25**, 909–917 (1993).
DOI: 10.1295/polymj.25.909

[14] Nakafuku C.: Effects of molecular weight on the melting and crystallization of poly(L-lactic acid) in a mixture with poly(ethylene oxide). Polymer Journal, **28**, 568–575 (1996).
DOI: 10.1295/polymj.28.568

[15] Nijenhuis A. J., Colstee E., Grijpma D. W., Pennings A. J.: High molecular weight poly(L-lactide) and poly (ethylene oxide) blends: Thermal characterization and physical properties. Polymer, **37**, 5849–5857 (1996).
DOI: 10.1016/S0032-3861(96)00455-7

[16] Hsieh Y-T., Nurkhamidah S., Woo E. M.: Lamellar orientation and interlamellar cracks in co-crystallized poly(ethylene oxide)/poly(L-lactic acid) blend. Polymer Journal, **43**, 762–769 (2011).
DOI: 10.1038/pj.2011.63

[17] Lustiger A., Lotz B., Duff T. S.: The morphology of the spherulitic surface in polyethylene. Journal of Polymer Science Part B: Polymer Physics, **27**, 561–579 (1989).
DOI: 10.1002/polb.1989.090270306

[18] Woo E. M., Wang L-Y., Nurkhamidah S.: Crystal lamellae of mutually perpendicular orientations by dissecting onto interiors of poly(ethylene adipate) spherulites crystallized in bulk form. Macromolecules, **45**, 1375–1383 (2012).
DOI: 10.1021/ma202222e